UNIVERSITY OF CALIFORNIA
RIVERSIDE

Progress Towards Laser Cooling and Trapping of Aluminum Monochloride

A Dissertation submitted in partial satisfaction
of the requirements for the degree of

Doctor of Philosophy

in

Physics

by

Chen Wang

December 2023

Dissertation Committee:

Dr. Boerge Hemmerling, Chairperson
Dr. Harry Tom
Dr. Christopher Bardeen

The Dissertation of Chen Wang is approved:

Committee Chairperson

University of California, Riverside

Acknowledgments

I am grateful to my advisor, without whose help, I would not have been here.

To my parents for all the support.

ABSTRACT OF THE DISSERTATION

Progress Towards Laser Cooling and Trapping of Aluminum Monochloride

by

Chen Wang

Doctor of Philosophy, Graduate Program in Physics
University of California, Riverside, December 2023
Dr. Boerge Hemmerling, Chairperson

Laser cooling and trapping of atoms have revolutionized atomic physics with the realization to cool and trap atoms into the ultra-cold regime. This has led the precision of spectroscopy on atoms to an unprecedented level, which make cold atoms not only platforms to search for new physics and test fundamental laws of nature, but also ultra-precise tools to measure fundamental physical quantities such as time and magnetic fields. Cooling and trapping molecules into the cold and ultra-cold regime foresees similar revolutions. The rich internal energy structure and large permanent electric dipole moments of molecules enable a variety of applications beyond the realm of cold atoms, including searches for the electron electric dipole moment, studies of ultra-cold chemistry, and realizations of strongly interacting quantum many-body systems. However, the complex energy structure of molecules also render them difficult to laser cool and trap, especially at high densities. In this thesis, we present our progress on pursuing laser cooling and trapping of a new species, aluminum monochloride(AlCl). The highly diagonal Franck-Condon factors(FCFs) and high scattering rate with large single photon recoil velocities owning to a cycling transition at DUV wavelength

range make it a favorable candidate. We present our absorption spectroscopy on the $A^1\Pi \leftarrow X^1\Sigma^+$ transition to extrapolate the molecular constants and estimate the Frank-Condon factors, and our effort to study the various targets for laser ablation production of AlCl to optimize its initial production. We also present our in-beam fluorescence spectroscopy to resolve the relevant hyperfine structure in the $A^1\Pi$ state in order to understand and construct optical cycling schemes.

Contents

List of Figures

List of Tables

Chapter 1

Introduction

1.1 Cold Atoms

The invention of the laser [1, 2] has revolutionized atomic physics to an unprecedented precision never seen before. Aided by the laser, the development of laser cooling and trapping of atoms [3, 4, 5, 6, 7] has put cold atoms into a central part of modern atomic physics. It becomes platforms for such a diverse areas in fundamental physics and technology. In the perspective of fundamental physics, the minimized thermal motion of atoms in the cold and ultra-cold regime enables unprecedented precision measurements of fundamental constants in nature [8, 9, 10] and unprecedented sensitive methods to test some fundamental laws in physics [11, 12, 13]. The ability to trap a sample of atoms in a lattice made of lasers can help the understanding of a variety of solid-state physics models with the advantage that the optical lattice [14, 15] is tunable and the atoms can be chosen to be either fermions or bosons [16, 17, 18]. In the perspective of technology, the ability to measure frequencies in the most precise way enables devices such as atomic clocks

[19, 20, 21, 22] to measure time in the most precise way and devices that can measure a variety of physical quantities precisely such as magnetic fields [23]. The quantum nature of cold atoms and precise control of lasers also put them as an ideal platform in the pursue of quantum computing [24].

1.2 Why Cold Molecules?

Molecules, as made of more than one atom, are different from atoms in many perspectives. Molecules have additional internal motions namely rotations and vibrations that lead to more complex internal interactions that can complicate the laser cooling and trapping process but on the other hand, those additional degrees of freedom can be explored as new features to study and manipulate. For example, some of the nearly degenerate energy levels, if ultra-precise measurements can be made, can be used to improve the sensitivity to the measurements of time evolution of fundamental physical constants [25, 26, 27, 28, 29] and the searches for the electron electric dipole moments [30, 31, 32, 33] and parity-violating interactions [34, 35, 36].

Hetero-molecules, which are of interest of most currently pursued laser cooled molecules, owning large permernant electric dipole moment(ususally more than 1 debye) [37] that can be induced by an electric field, can be advantageous to create strongly-correlated systems such as the quantum hall systems [38], and give rise to new phases of matter such as supersolids [39] and certain lattice-spin systems [40, 41]. The large electric dipole moment, in combination with some advantages to the cold atoms systems such as weak coupling to environments, being able to be cooled and trapped individually and having complete

control over the quantum states, put them in a favorable position to pursue a new quantum computing platform [42, 43].

Another important aspect of molecules cooled to low temperatures is that it opens the way to understand collisions and chemical reactions in the quantum regime [44]. The question of what happens when two molecules collide still remain largely unknown [45]. To be able to gain insights in such processes, one would need to cool the molecules down to a single quantum state and then by controlling the inputs and detect the outputs, one can gain understandings of a variety of processes that can happen such as chemical reactions or clustering [46, 47]. Furthermore, the energy levels of molecules can be tuned by external electromagnetic fields and these effects are particularly enhanced at low temperatures which could open pathways to control chemical reactions [48, 49, 50]. Cold collisions are also dominant processes in astrophysical systems and processes such as in interstellar clouds and during star formation, thus gaining understanding on cold collisions could help understand some astrophysical processes.

1.3 Production Methods of Ultracold Molecules

Techniques to cool and trap molecules have been garnered for almost three decades. While there are plenty of proposed methods, only a handful have been effectively put into practice, and each has its own limitations. Generally, methods to produce cold molecules fall into two categories: direct and indirect. Direct methods involve forming the molecules first and subsequently cooling them. In contrast, indirect methods produce ultracold molecules by assembling laser-cooled atoms. This section gives an overview of the key methods show-

cased so far.

1.3.1 Indirect Cooling Methods

Association of Laser Cooled Atoms

So far, the most matured method for producing ultracold molecules is assembling them from ultracold atoms through either photo-association [51, 52, 53] or magneto-association stemming from a Feshbach resonance [54, 55]. Experiments so far have successfully formed ground state polar molecules close to quantum degeneracy [55]. However, this approach is limited to molecules made of atoms that can be laser-cooled. As a result, only diatomic molecules formed from alkali and alkaline earth atoms combinations have been made in this manner, and the production quantity remains relatively low (around 10^4)[55]. Furthermore, this method involves cooling to the ground state after the cold molecules are formed, which is by far still at low efficiencies.

1.3.2 Direct Cooling Methods

Direct laser cooling, compared to the indirect method, follows essentially the same procedure as laser cooling of atoms, despite the complexity associated with molecules, thus can avoid the limitations of the indirect method, in two major aspects. One is that in direct laser cooling, the species are not limited anymore to combinations of alkali and alkali-earth atoms, but rather, to any molecule that can be made and amenable to laser cooling. This is important because different properties and energy structures of different molecules are going to be suitable for different applications, thus a more diverse species of cold molecules is always preferable. Another aspect of direct laser cooling is that just like laser cooling of

atoms, once the molecules are successfully cooled and trapped, they are going to be in the ground state, eliminating further cooling procedures in indirect methods which have low efficiencies.

However, direct laser cooling comes with its own cost. The Doppler cooling method employed in atom cooling relies on momentum exchange with photons. Since photons in generally have much smaller momentum than atoms or molecules, any cooling transition would be required to have a high scattering rate and a relatively closed transition. To put in some quantitative perspective, Doppler cooling of an atom or molecules with mass > 20 amu from room temperature to ultracold temperatures in the visible range, would require scattering $> 10^4$ photons. To scatter such a number of photons before the atom or molecule falls out of its original cycling transition, the transition must be closed, meaning the transition would need to have a high enough probability to spontaneously decay back to its initial ground state. Unfortunately, most molecules do not have such transitions. A first and dominant bottleneck to find such transitions in molecules is the branching to different vibrational states. This is determined by the Franck-Condon factors(FCFs), which describe the overlap of vibrational states between different electronics states. Most molecules have Franck-Condon factors that make them scatter 10^4 photons impossible, thus all the candidate molecules for laser cooling including the molecule of interest of this thesis have a transition that has high enough FCFs to be able to scatter enough photons [56], although the aid of repump lasers is still needed, since in real atoms and molecules, there is no completely closed transitions. Following vibrational branchings, rotational branching is the next mechanism for the molecule to fall out of its cycling transition. Unlike vibrational

states, rotational states have selection rules, which requires $\Delta J = 0, \pm 1$ where J is the rotational quantum number. This means that a spontanous decay from excited state could end up in three possible states per vibrational state, thus careful considerations need to be made to choose the rotational transition employed in optical cycling.

1.4 Thesis Organization

The rest of the thesis is organized as follows: Chapter 2 gives an overview of the energy structure of molecules relevant to laser cooling with a detailed discussion on Aluminum Monocloride(AlCl), including its Hamiltonian and optical cycling scheme. Chapter 3 gives detailed description of our experimental setups such as the cryogenic buffer gas beam source, magneto-optical traps, etc. with a discussion of the molecular beams that have been debugged many times. Chapter 4 documents the ultra-violet (UV) laser systems employed in all of our experiments so far and a Rubidium saturation absorption spectroscopy setup to calibrate our wavemeter. Chapter 5 discusses the in-cell absorption spectroscopy we did to understand the molecular structure of AlCl especially the FCFs. Chapter 6 gives a discussion of a systematic investigation we made on various targets used to produce AlCl with a goal of optimizing its initial production. Chapter 7 presents in-beam fluorescence spectroscopy we did to understand the hyperfine structure of the $A^1\Pi$ state relevant to laser cooling. Chapter 8 summarizes the work in this thesis and discusses outlooks for future directions.

Chapter 2

Molecules and AlCl

A diatomic molecule consists of two atoms, which can either be of the same or different atomic types. While these molecules exhibit electronic energy levels akin to atoms, they also present additional complexities due to vibrations and rotations within the molecule. This makes diatomic molecules inherently more complex than individual atoms. However, according to the Born-Oppenheimer approximation, the electronic, vibrational, and rotational aspects can be largely considered separately as they are mostly decoupled at a first-order approximation. If any higher-order interactions occur, these can typically be addressed using perturbative methods or be analyzed exactly for the relevant state [57].

For molecules to be suitable for laser cooling, they must satisfy specific conditions, like laser cooling in atomic systems. In summary, these requirements are: First, a band system that possesses strong one-photon transitions to guarantee the fast photon-scattering rates essential for laser cooling. Second, a predominantly diagonal Franck-Condon arrangement within the band system, and third, the absence of intermediate electronic states that

could disrupt the cycling transition by allowing decays from the upper state [56].

This chapter delivers an overview of molecular structure relevant to laser cooling along with a detailed discussion on the Hamiltonian of aluminum monocloride (AlCl).

2.1 Energy Structure Overview

Electronic energy levels of diatomic molecules are typically labeled by letters. The ground state is generally indicated by X. Higher energy electronic states can be represented by uppercase letters (A, B, C, ...) or lowercase letters (a, b, c, ...) based on their multiplicity in relation to the ground state. Generally, the sequence of these letters reflects the energy of the states. Any deviation in this order typically arises when a state is identified after others have been established and denoted. The energy differences between electronic states are typically the largest among all molecular energy scales, often falling in the ultraviolet (UV) or visible regions of the electromagnetic spectrum.

Beyond electronic states, the next significant energy scale pertains to the molecule's vibrational states. For every electronic state, there's an associated potential energy curve. This curve results from the interplay of repulsive forces when the two atomic nuclei get too close and attractive forces from the electrons attracting the nuclei. The bottom of this potential curve resembles a harmonic potential well and leads to quantized vibrational levels which is typically the case at low temperatures. The energy gaps between these vibrational levels are generaly smaller than those of electronic transitions but are still significant, usually lying in the infrared (IR) region of the electromagnetic spectrum. Unfortunately, radiation tools within this frequency spectrum are usually not readily accessible.

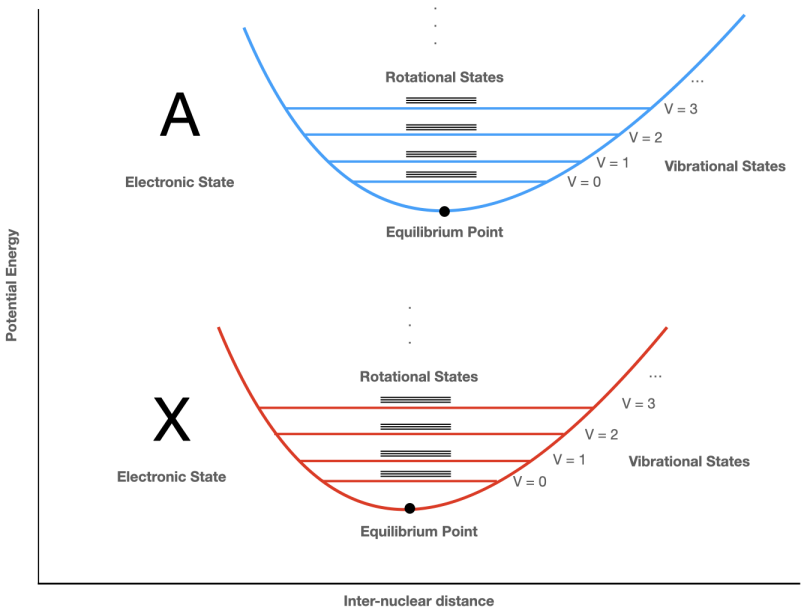

Figure 2.1: Illustration of the electronic, vibrational and rotational energy of a diatomic molecule

As the molecule vibrates, it can also rotate about its center of mass. This rotational motion is quantized into rotational energy levels. The simplest model to describe these levels is the rigid rotor model. While real molecules are not rigid, this model gives a good first-order approximation. The energy differences between rotational levels are the smallest among the three degrees of freedom, lying in the microwave region of the spectrum. Gaps between lower rotational levels usually hover around 10 GHz.

Figure 2.1 gives a simple illustration of the electronic, vibration and rotational energies of a diatomic molecule.

2.2 Born-Oppenheimer Approximation

The Born-Oppenheimer approximation plays a central role in our understanding on molecules. It proposes that due to the significant mass difference between electrons and nuclei, we can distinctively treat the movements of electrons and nuclei. As a result, the total wavefunction of a molecule can be described as a product of its electronic, vibrational, and rotational wavefunctions. This distinction often eases the analysis of molecular energy levels. However, there are situations, especially at elevated energies or with heavier atoms, where this approximation does not hold true.

2.3 Establishing Notations

Quantum Numbers

Table 2.1 gives the notations of the variety of quantum numbers of the diatomic molecules used in this thesis.

State Labeling

In atomic systems, we use a term symbol to label the state of an atom. In molecules, we do so too. The term symbol to label a molecular state is give by:

$$^{2S+1}\Lambda^{+/-}_{\Omega,u/g} \tag{2.1}$$

Where S, Λ and Ω are all expalined in 2.1. The +/- [1]refer to parity associated with

[1]Labeling of +/- is not nessessary in $\Lambda > 0$ states since those states always occur as +/- pairs called Λ doublets

the reflection symmetry of wavefunctions upon reflection with respect to a mirror plane, while u/g (gerade/ungerade) [2] classifications are associated with inversion symmetry (often in linear molecules).

Notation	Description
$\mathbf{V}$	vibration of the nuclei
$\mathbf{R}$	rotation of the nuclei
$\mathbf{L}$	electronic orbital angular momentum
$\mathbf{S}$	electronic spin angular momentum
$\mathbf{I}$	nuclear spin angular momentum
$\mathbf{N} = \mathbf{L} + \mathbf{R}$	total orbital angular momentum
$\mathbf{J} = \mathbf{N} + \mathbf{S}$	total orbital angular momentum + electronic spin
$\mathbf{F} = \mathbf{J} + \mathbf{I}$	total angular momentum of the molecule
Λ	projection of $\mathbf{L}$ along the internuclear axis
Σ	projection of $\mathbf{S}$ along the internuclear axis
Ω	$\Lambda + \Sigma$

Table 2.1: Quantum numbers of diatomic molecules

[2] However, it is usually more convenient to factor out a common phase factor to define e/f parity. Discusion of this can be found in [58]

2.4 Hund's Cases

All the molecular angular momenta listed in table 2.1 can interact and couple together in a variety of ways, depending on the interaction energy and relative coupling strength between them. The coupling schemes were first described by Hund with five ideal cases, while real molecules are never the ideal cases, Hund's cases give a good approximation and thus is a powerful tool to understand the interactions of the variety of angular momenta in molecules. Among all the candidate molecules to laser cool, most fall into Hund's cases a and b, so we will give a discussion on the two cases. Other cases can be found in reference [57] if needed.

2.4.1 Hund's Case a

In Hund's case a 2.2, both L and S interact strongly with the electrical field along the molecular axis so that both precess rapidly about the axis and thus the projections Λ and Σ are constants, along with their sum Ω, are all considered good quantum numbers. Ω then adds to the end-over-end molecular rotation R to form the total angular momentum J, which excludes the nuclear spin. Hence, the angular momenta Ω and R precess about J which is fixed in space and thus a good quantum number in Hund's case a.

2.4.2 Hund's Case b

In Hund's case b 2.3, while the electronic orbital angular momentum L is still coupled strongly to the molecular axis, the electronic spin angular momentum S is coupled stronger to $N = \Lambda + R$ than to the axial field. Thus, L still precesses rapidly about the

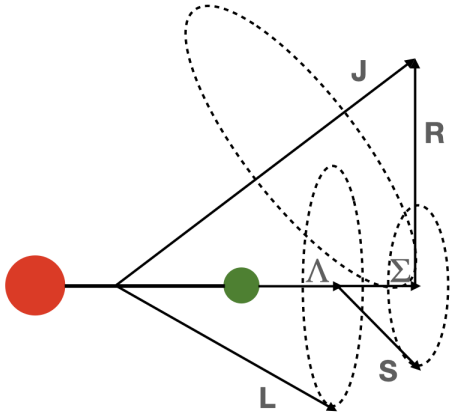

Figure 2.2: Vector diagram of Hund's case a. Dashed circles indicate precessions

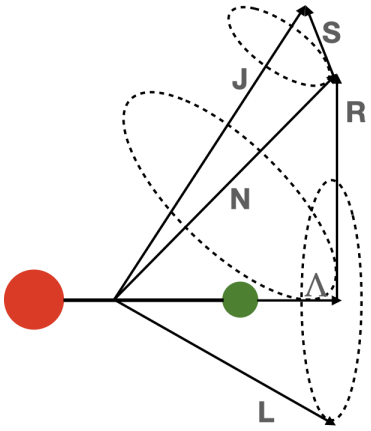

Figure 2.3: Vector diagram of Hund's case b

molecular axis and Λ adds to R to form N and then, S is added to N to form J which is fixed in space and about which N and S precess. Thus J is also a good quantum number in Hund's case b.

2.5 General Properties Concerning Laser Cooling of Molecules

Laser cooling in general relies on rapid scattering of a large number of photons. For molecules, this demands a strong transition with nearly diagonal Frank-Condon factors with only a few vibrational branches that need to be addressed. It is also important to avoid decays into intermediate states. Molecules with simpler ground-state hyperfine structure tend to be preferable, although not necessary since there are ways to generate sideband light that can address multiple hyperfine components. While a strong transition is needed to cool molecules with a high initial temperature, narrow transitions can be used for cooling to much lower temperatures [59], similar to narrow transitions in some atomic laser cooling scheme such as the $^1S_0 \rightarrow {}^3P_1$ transition in ^{87}Sr and ^{88}Sr [60].

Up to date of the writing of this thesis, all diatomic molecules that have been laser cooled so far, namely SrF [61], CaF [62, 63] and YO[64] share the same type of optical cycling transition, $X^2\Sigma^+_{1/2} \leftrightarrow A^2\Pi_{1/2}$, similar to the $^2S_{1/2} \leftrightarrow {}^2P_{1/2}$ transitions in alkali atoms. A primary key feature of such molecules is that they have an unpaired electron whose wavefunction is localized around the alkali-earth or alkali-earth like atom in the molecular configuration, and after an excitation from the ground state to an excited state, this results in a tiny change in the equilibrium distance(molecular bond length) between the two atoms, which leads to highly diagonal Frank-Condon factors. However, this unpaired

electron significantly increase the reactivity of such molecules which can limit the number of molecules during both the initial production and the final magneto-optical trap(MOT). Furthermore, such transitions have to employ the P(1) line as the cycling transition in order for the rotational closure. The larger number of ground states would lead to dark states that need to be addressed by remixing methods. The unpaired electron also leads to a large g-factor in the both states that make the Zeeman levels more complicated to deal with. All of this leads to long slowing distance and low capture velocities $\sim$10m/s of such molecules. As a result, the MOTs of such molecules remain in low densities so far which prevents many of the applications of cold molecules.

Other than the molecules that have a similar cycling transition as in alkali atoms, there is a another group of molecules that are similar to alkali-earth atoms where the valence electrons pair to form a closed shell and thus spin singlet states. Currently, to the knowledge of the writer, three of such molecules are being pursued for laser cooling, AlF [65, 66], TlF [67, 68] and the molecule of interest of this thesis, AlCl [69, 70]. In the rest of the thesis, these two groups of molecules will simply be referred to as singlet and doublet molecules.

Compared to doublet molecules, singlet molecules seem to be able to overcome some of the disadvantages associated with doublet molecules discussed above. The closed shell singlet nature makes them chemically less reactive than doublet molecules which would inherently reduce two-body losses in the MOT and thus increase the MOT density. The lack of any electronic angular momentum in the ground state makes the ground stated hyperfine structure much simpler than doublet molecules. In fact, in the case of AlCl, the ground state hyperfine structure bandwidth is within the natural linewidth of the ro-vibrational state [3].

[3]However, the nuclear spins of Al and Cl are 5/2 and 3/2 respectively which makes the $A^1\Pi$ state

All the three singlet molecules being pursued for laser cooling have a cycling transition in the ultra-violet(UV) regime, along with their smaller number of ground states, this leads to a high spontaneous decay rate. This can be seen from the Einstein A coefficient[71],

$$A_{21} = \frac{g_1}{g_2}\frac{4\alpha}{3c^2}\omega_{21}^3 D_{12}^2 \tag{2.2}$$

that describes the spontaneous decay rate for a excited state, where g_1 and g_2 are the degeneracy of the ground and excited states, α the fine structure constant, c the speed of light, D_{12} the dipole transition matrix element and ω_{21} is the resonate transition frequency. A high spontaneous decay rate, which we define as γ in this thesis, leads to a high scattering rate[72],

$$R_{sc} = \frac{s_0\gamma/2}{1 + s_0 + (2\delta/\gamma)^2} \tag{2.3}$$

where s_0 is the saturation parameter defined as I/I_s, and δ is the detuning of the laser. In the case of resonant light, a high saturation parameter(i.e high intensity light) makes R_{sc} saturate to $\gamma/2$. The high momentum associated with an UV photon also provides a large recoil velocity. As a result, a cycling transition at UV leads to higher scattering rates and large recoil velocities, both of which are favorable in laser cooling.

2.6 Properties of AlCl

AlCl was first observed by accident in 1913 [73] where Jevons and co-workers were investigating the modification of the emission spectra of silicon tetrachloride($SiCl_4$) under

hyperfine structure complicated. The discussion of the hyperfine struture of the $A^1\Pi$ state will be discussed in a later chapter.

nitrogen environment. The observed emission band near 261nm was later identified to be AlCl formed by the liberated Cl atoms from $SiCl_4$ and Al atoms from the aluminum electrodes of the discharge tube [74]. AlCl was first systematically investigated in 1934 by Bhaduri and Fowler[75] and Mahanti[76] where the ro-vibrational structure was first assigned. Later on, the first high resolution experiment in the optical regime was carried out by Ram et al. in 1982[77]. The first high resolution spectroscopy at low temperature to resolve the ground and lower exited ro-vibrational states that are relevant to laser cooling was carried out recently[69].

It was first predicted to be a candidate for laser cooling in 2004 by Di Rosa[56], due to its short life time of the $A^1\Pi$ state, thus a correspondingly high scattering rate, and highly diagonal Frank-Condon factors[78, 79]. More recently, a few groups have performed *ab initio* calculations on the properties of AlCl[80, 81, 82], which are in decent agreement with the previously measured and calculated values. Considering all the calculations and measurement done on the $A^1\Pi$ state life time, we take an approximate value of $\sim$ 5ns to gain ideas of the scattering rate, which would correspondingly be $\sim 2\pi$ x 30MHz. While all the previous calculations and measurements predicted also highly FCFs, our recent low temperature high resolution spectroscopy results further confirmed this and measured a FCFs of the v_{00} branch to be 0.9988[69]. Both properties strongly support that AlCl is amenable for laser cooling. In the original paper by Di Rosa, we note that AlF which has a similar structure as AlCl, is also predicted to be a candidate laser cooling molecule and is currently being pursued experimentally as well[65, 66].

AlCl comes with two isotopes, $^{27}Al^{35}Cl$ and $^{27}Al^{35}Cl$ with natural abundances of

$\approx 76\%$ and $\approx 24\%$ respectively. The two isotopes are similar in properties except that they have slightly different masses and molecular constants which have little effect in terms of laser cooling. Thus, considering the much larger natural abundance of the $^{27}Al^{35}Cl$ isotope, our work is focused on it and in the rest of the thesis, the nuclear number will be omitted in the notation unless they need to be specifically mentioned.

As mentioned earlier, one of the unique properties of molecules that give them certain advantages over atoms for applications such as quantum computing and simulations of quantum many-body systems is the large electric dipole moment(EDM) that can be induced by an electric field. Despite AlCl has one of the smallest EDMs among all the proposed laser coolable molecules which is ≈ 1.6 Debye [37], it certainly still holds such potentials. Besides all other potential applications of cold molecules discussed in the previous chapter, AlCl has its own unique applications. In terms of laser cooling, the chlorine atom that belongs to group 7 of the periodic table, which are part of the halogen family is in general not amenable for laser cooling. The aluminum atom, as a group 3 metal atom, despite the recent success in creating a MOT of indium [83] which is in the same group, the energy structure of Al still makes it too complicated to laser cool and no successful laser cooling of Al has been made. However, if one can successfully laser cool AlCl, both cold Al and Cl atoms can be obtained by dissociating it with a single photon or by two photon ionization process which will be mentioned in later chapters. AlCl also has industrial applications. It can be used to produce solar-grade silicon [84, 85] and can be found in rocket plumes as an optical diagnostic tool for exhaust in rocket launching [86]. Solid densities of AlCl can also be formed by blocking the reaction channel of the formation of the stable compound $AlCl_3$

[87] which itself can be an interesting 2-dimensional material to study and for laser cooling, it can be used as a precursor for producing gas phase AlCl which can conceivably produce much higher densities than the current method of mixing Al powder with Cl compounds [70] and this is critical for producing a high density MOT. AlCl is also important in astrophysics. It was first predicted to exist in carbon-rich and oxygen-rich stars[88] and then detected by several groups later on[89, 90, 91]. It can also be found in the photo-sphere of the Sun[92]. Thereof, experimental and theoretical research to improve the precision of the molecular constants, especially at low temperatures can be important for astrophysical applications.

2.7 AlCl Hamiltonian

To determine whether a molecule is suitable for laser cooling and eventually design an optical cycling scheme, one must first figure out the potential energy curves and molecular constants of the relevant states and then calculate the transition dipole moments to obtain vibrational and rotational branching ratios, for all of which, one needs to construct an effective Hamiltonian of the states and figure out all the dominant terms. A general expression to include all interactions in the absence of external fields is given by equation 7.183 of reference [57],

$$H = H_e + H_{vib} + H_{rot} + H_{cd} + H_{so} + H_{ss} + H_{sr} + H_{\Lambda d} + H_{hfs} + H_Q + H_{fs} \tag{2.4}$$

Where H_e, H_{vib} and H_{rot} are the electronic, vibrational and rotational energies. H_{cd} describes the centrifugal distortion. H_{so} and H_{ss} are spin-orbital and spin-spin in-

teractions. H_{sr} is the spin-rotation interaction. $H_{\Lambda d}$ is the Λ-doubling interaction. H_{hfs} and H_Q are the magnetic hyperfine interaction and electric quadruple hyperfine interaction respectively. The last term H_{fs} indicates any higher-order fine structure interaction.

For AlCl, we first choose basis sets for both $X^1\Sigma^+$ and $A^1\Pi$ states. Since both states do not have electronic spin, Hund's case (a) as depicted in 2.2 would be the most appropriate choice for both states. In such, for the $X^1\Sigma^+$ state, $J = R$ and for the $A^1\Pi$ state, $J = \Lambda + R$. Then the magnetic hyperfine interaction with the nuclei is first to couple J with the nuclear spin I_{al} of the Al nucleus to form an intermidiate quantum number F_1 and then couple F_1 to the nuclear spin I_{cl} of chlorine nucleus to form F, the full angular momentum of the molecule including hyperfine interactions and with projections of m_F to any given quantization axis. We finally obtain basis states for both states as $|\eta, \Lambda, J, F_1, F, m_F\rangle$, where η includes all the electronic and ro-vibrational energies. The Hamiltonian for $X^1\Sigma^+$ and the $A^1\Pi$ state are then given respectively as,

$$H_X = H_e + H_{vib} + H_{rot} + H_{Q_0} \tag{2.5}$$

$$H_A = H_e + H_{vib} + H_{rot} + + H_{Q_2} + H_{LI} + H_{\Lambda d} \tag{2.6}$$

Where H_{Q_0} is the electric quadrupole hyperfine interaction in the $X^1\Sigma^+$ state. Since there is no electronic angular momentum in the X state and the magnetic interaction of the nuclear rotation with the nuclear spins is much weaker, only the electric quadrupole interaction is considered for hyperfine interactions in the X state. In the $A^1\Pi$ state, H_{Q_2} is the electric hyperfine interaction and H_{LI} is the magnetic hyperfine interaction between $J = \Lambda + R$ and

the nuclear spins. $H_{\Lambda d}$, called Λ-doubling, arises due to the two different orientations of the electron orbital motion. The electric quadrupole hyperfine interaction is the interaction between the nuclear quadrupole moment of a nucleus and the electric field gradient produced by the surrounding electron cloud and other nearby nuclei. The subscripts 0 and 2 indicate the interactions along the inter-nuclear axis and perpendicular respectively. We will give a detailed description of all the terms in both states in the following sections.

2.7.1 Vibrational Energy Structure

The vibration of a diatomic molecule can be treated as a harmonic oscillator within the Born-Oppenheimer approximation where the energies follow that of a quantum harmonic oscillator,

$$G(v) = w_e(v + 1/2) \tag{2.7}$$

However, in real molecules, the potential energy is not exactly harmonic and is better described by Morse potential[58], as depicted in 2.4

$$V(r) = D_e(1 - \exp -\beta(r - r_e))^2 \tag{2.8}$$

where D_e is the dissociation energy of the molecule and r_e is the equilibrium inter-nuclear distance. β here is a parameter that describes how wide the potential well is. Vibrational energy levels associated with Morse potential include anharmonic contributions and can be expressed in general as a series expansion[57],

$$G(v) = w_e(v + 1/2) - w_e x_e(v + 1/2)^2 + w_e y_e(v + 1/2)^3 + ... \tag{2.9}$$

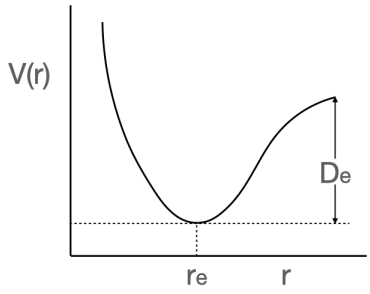

Figure 2.4: Morse Potential

where w_e is the vibrational constant and x_e, y_e are constants that describe different orders of anharmonicities.

Frank-Condon Factors

Frank-Condon Factors(FCFs) are quantities that describe the wavefunction overlaps between vibrational states of different electronic states[4], given by,

$$q_{v',v''} = |\langle \psi_{v'} | \psi_{v''} \rangle|^2 \tag{2.10}$$

One should be careful that Frank-Condon factors alone do not describe the vibrational branching ratios(VBRs) which is in general captured by the square of transition moment

[4]The vibrational wavefunctions within an electronic state are orthogonal to each other, however they are not between different electronic states since different electronic states have different molecular constants.

integral,

$$\int \psi_{e'v'} \mu \psi_{e''v''} \, d^3r \tag{2.11}$$

which also includes other two factors, the strength of the electronic transition and the populations of different vibrational levels. The vibrational branching ratios is given by,

$$VBR_{v'.v''} = \frac{q_{v',v''} \times f_{v',v''}}{\sum_{k=0}^{\infty} q_{v',k} \times f_{v',k}} \tag{2.12}$$

where $f_{v',k}$ are the transtion frequencies and $q_{v',k}$ are FCFs. Despite FCFs alone only gives an upper limit of the branching ratio, it is often close enough to the VBRs such that one can gain a decent idea of the VBRs by only knowing the FCFs which can be calculated by experimental data or theoretical methods. The details of the FCFs of AlCl will be discussed in chapter 5.

2.7.2 Rotational Energy Structure

Besides vibrations, the nucleus of molecules also rotate about the center of mass. The rotational motions of the nucleus contribute to the smallest energies in the electro-rovibrational energy structure. The rotational energy levels within a vibrational energy level are given by[57],

$$F_v = B_v J(J+1) - D_v J^2(J+1)^2 + H_v J^3(J+1)^3 + ... \tag{2.13}$$

Where B_v is the rotational constant as if the molecules were rigid rotators. However, real molecules are not rigid as the atoms experience centrifugal forces and cause distortions in the rotations of the molecule. D_v is the constant that describe such distortions. H_v is the constant that accounts for the anharmonicities of the electronic potential well. B_v, D_v and

H_v can be expressed in terms of other molecules constants that are used more in general, especially in the more compact Dunham model discussed next,

$$B_v = B_e - \alpha_e(v + 1/2) + \gamma_e(v + 1/2)^2 + ... \tag{2.14}$$

$$D_v = D_e + \beta_e(v + 1/2) + ... \tag{2.15}$$

$$H_v = H_e + ... \tag{2.16}$$

2.7.3 Dunham Model

We talked about the Morse potential in the discussion on the vibrational energy structure and how it accounts for the anharmonicities of the electronic potential of a molecule, however, it still does not include effects due to the coupling between the vibrational and rotational motions. Dunham constructed a more general form of the potential called Dunham potential[93],

$$V(\xi) = a_0\xi^2(1 + a_1\xi + a_2\xi^2 + ...) \tag{2.17}$$

where

$$\xi = \frac{r - r_0}{r_0} \tag{2.18}$$

Obtaining exact analytical solutions of the eigenvalues and wavefunctions is impossible with the Dunham potential. However, by using WKB (Wentzel–Kramers–Brillouin) method, Dunham was able to obtain approximate analytical solutions and the energy levels are given by,

$$E_{vJ} = \sum_{jk} Y_{jk}(v + 1/2)^j (J(J+1))^k \tag{2.19}$$

Where Y_{jk} are called Dunham coefficents and can be directly related to spectroscopic constants given by the below table,

$Y_{00} = T_e$		
$Y_{10} = w_e$	$Y_{20} = -w_e x_e$	$Y_{30} = w_e y_e$
$Y_{01} = B_e$	$Y_{11} = -\alpha_e$	$Y_{21} = \gamma_e$
$Y_{02} = -D_e$	$Y_{12} = \beta_e$	
$Y_{03} = H_e$		

Table 2.2: Relationship between Dunham coefficients and spectroscopic constants

Molecules often come with various isotopes. For example as discussed previously, AlCl has natural abundances of ^{27}Al ^{35}Cl and ^{27}Al ^{37}Cl. The different isotopes have different Dunham coefficients due to different reduced masses. In general, the dependence of Dunham coefficients on the reduced mass is given by[58],

$$Y_{jk} \propto \mu^{-(j+2k)/2} \tag{2.20}$$

So we can define a set of mass independent Dunham coefficients as,

$$U_{jk} = \mu^{(j+2k)/2} Y_{jk} \tag{2.21}$$

This allows one to define Dunham energy levels that include all isotopes and can be useful

for interperting spectroscopic data,

$$E_{vJ} = \sum_{jk} \mu^{-(j+2k)/2} U_{jk} (v + 1/2)^j (J(J+1))^k \tag{2.22}$$

Dunham coefficients of AlCl for the $X^1\Sigma^+$ state can be found in [94] and for the $A^1\Pi$ state are presented in chapter 5.

2.7.4 X State Hamiltonian

The $X^1\Sigma^+$ state Hamiltonian is expressed as,

$$H_X = H_e + H_{vib} + H_{rot} + H_{Q_0} \tag{2.23}$$

Where the first three terms are all included in the Dunham model and is disccused in detail in [94] where the result of molecular constants derived from spectroscopic data is also presented. In the $X^1\Sigma^+$ state, the projection of the orbital angular momentum and the spin angular momentum of the electron are both 0, leaving the only magnetic hyperfine interaction coming from the interaction between the rotations of the nuclei and the nuclear spins, which is orders of magnitude smaller than that between electronic angular momentum and nuclear spin. Thus, the only dominant hyperfine term in the X state is the electric quadruple interaction between the quadruple term of the nuclear Coulomb potential due to unsymmetrical charge distribution of the nuclei and the electric field gradient also caused by unsymmetrical and often complex charge distribution of electrons in the molecule, and is given in the tensor notation by[57],

$$H_{Q_0} = \sum_{\alpha} \frac{\sqrt{6}(eQq_0)_\alpha}{4I_\alpha(2I_\alpha - 1)} T_0^2(\mathbf{I}_\alpha, \mathbf{I}_\alpha) \tag{2.24}$$

where the summation is over all nuclei, in this case the nucleus of Al and Cl. The subscript 0 here in the tensor notation indicates the interaction between the electric field gradient and the nuclear quaduple moment is along the molecular axis, as is the case for Hund's case (a). The electric quaduple constants in the ground state AlCl have been previously measured and provided by the below table[95]. The energies associated with electric quadruple hyperfine

Constant	Value (MHz)
$(eQq_0)_{Al}$	-29.8(50)
$(eQq_0)_{Cl}$	-8.6(10)

Table 2.3: Electric quadruple constants eQq_0 for the $X^1\Sigma^+$ state.

interaction is in general much smaller than the magnetic hyperfine interaction involving in electronic angular momentum as is the case for the $A^1\Pi$ state. As a result, for AlCl, the largest hyperfine splitting associated with the $J = 1$ state is $\Delta E \approx 11$MHz [95], which is well within the natural linewidth of the $X^1\Sigma^+ \leftrightarrow A^1\Pi$ transition, $\Gamma/2\Pi \approx 30$MHz. While an unresolved hyperfine structure in the ground state provides the advantage that all the ground states can be addressed with a single laser, the small g-factor (thus insensitive to external magnetic field) in the ground state makes it difficult to do dark states remixing as needed for $^2\Sigma$ molecules. However, there is another approach to address the dark state issue by doing polarization switching of the laser. The issue associated with the ground dark states in AlCl is still unclear and experimental work is currently being performed by measuring photon scattering rate with and without photon polarization switching by the McCarron group.

2.7.5 A State Hamiltonian

The $A^1\Pi$ state Hamiltonian is expressed as,

$$H_A = H_e + H_{vib} + H_{rot} + H_{LI} + H_\Lambda + H_{eQ} + H_Z \tag{2.25}$$

Where $H_e + H_{vib} + H_{rot}$ are again the electronic, and ro-vibrational eneries within the Dunham model and have been measured and presented in [69]. Since the $A^1\Pi$ state has a non-zero electron orbital angular momentum, the most dominant term in the hyperfine structure is from the interaction between the electron orbital angular momentum and the nuclear spins, expressed as,

$$H_{\mathrm{LI}} = \sum_\alpha a_\alpha T^1(\mathbf{L}) \cdot T^1(\mathbf{I}_\alpha) \tag{2.26}$$

Fitting of the data presented in chapter 7 also confirms that this is the most dominant interaction for the hyperfine structure. Similar to the $X^1\Sigma^+$ state, the $A^1\Pi$ state also has electric quadruple interactions despite much smaller than the leading term H_{LI}. The electric quadruple interaction in the $A^1\Pi$ has both the components along and perpendicular to the inter-nuclear axis, expressed as,

$$H_{\mathrm{eQ}} = \sum_\alpha \frac{eQ_\alpha}{4I_\alpha(2I_\alpha - 1)} \left[\sqrt{6} q_{0,\alpha} T^2_0(\mathbf{I}_\alpha, \mathbf{I}_\alpha) + \sum_{k=\pm 1} e^{(-2ik\phi)} q_{2,\alpha} T^2_{2k}(\mathbf{I}_\alpha, \mathbf{I}_\alpha) \right] \tag{2.27}$$

Where q_0 terms are interactions along the inter-nuclear axis and q_2 terms are interactions perpendicular to the inter-nuclear axis.

In the $A^1\Pi$ state, the projection of the electron orbital momentum L(which is not a good quantum number in Hund's case a), along the inter-nuclear axis Λ is a good quantum number and have projection values of $\Lambda = \pm 1$. This can be visualized as the electron

orbiting clock and counter-clock wise with respect to the inter-nuclear axis. The two different projections of the electron orbital angular momentum cause two different interactions with the end-over-end rotation of the molecule R, resulting in a double energies states with opposite parities for each rotation R, denoted as Λ-doublets, with its Hamiltonian expressed as,

$$H_\Lambda = -\sum_{k=\pm 1} e^{-2\imath k\phi} q T^2_{2k}(\mathbf{J}, \mathbf{J}) \tag{2.28}$$

As a similar molecule, it is discussed in [66] that one loss channels for optical cycling of AlF could be due to the mixing of the Λ doublet states caused by external electric fields which results in a parity change in the $A^1\Pi$ state and thus potentially terminate the cycling. This effect largely depend one the Λ-doulet constant q_0 that will be presented in chapter 7.

In summary, the energy structure that is relevant to laser cooling of AlCl is depicted in fig2.5, adopted from the thesis of[96].

2.8 Zeeman Splitting

When an atom or molecule is placed in an external magnetic field, the degenerate m_F states of the each hyperfine state F will be splitted into different energy states known as the Zeeman effect. The Zeeman splitting is utilized in laser slowing, the enhancement of confining forces in magneto-optical traps(MOT) and engineer dark states in certain types of MOTs. Thus, understanding the Zeeman structure of the relevant states of a molecule is crucial for the determination of the optical cycling scheme of it. In the $X^1\Sigma^+$ state, there is no electron orbital angular momentum and no electron spin. Since the magnetic moments associated with the end-over-end rotations of the molecule is several orders of magnitude

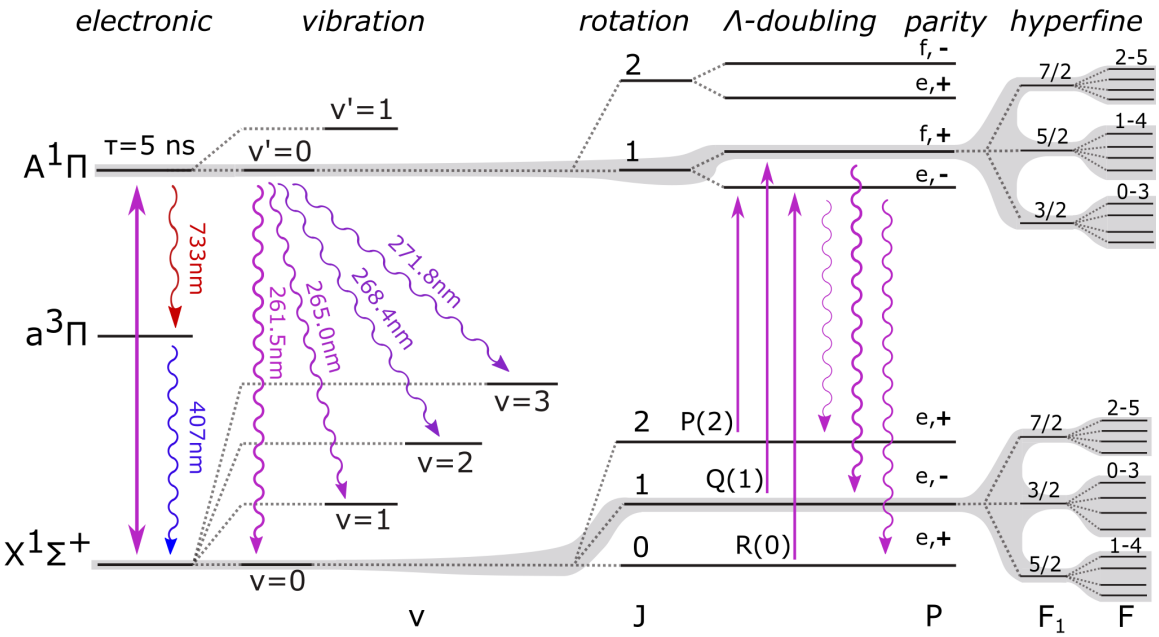

Figure 2.5: Overview of the energy structure that is relevant to laser cooling of AlCl. The grey shaded area indicates optcial cycling transitions. This figure is adopted from the thesis[96].

smaller than even nuclear spin magnetic moments, the most and only dominate interaction that give the Zeenman splitting in the $X^1\Sigma^+$ state is between the nuclear spins and the external magnetic fields, expressed as,

$$H_{Z,X} = -\sum_{\alpha} g_\alpha \mu_\alpha I_\alpha B_z = -\sum_{\alpha} g_\alpha \mu_\alpha T^1_{q=0}(\mathbf{I}_{\alpha,z}) \cdot T^1_{q=0}(\mathbf{B}_z) \tag{2.29}$$

where g_α, μ_α, I_α are the g-factors, nuclear magnetons, spin angular momentum quantum numbers of the Al and Cl nuclei respectively and B_z is the externally applied magnetic field.

For the $\mathrm{A}^1\Pi$ state, there is electron orbital angular momentum and the interaction of it with the external magnetic field is the most dominant Zeeman splitting, since the nuclear magneton is $\sim$ 2000 times smaller than that of the Bohr magneton. It is expressed as,

$$H_{Z,A} = -g_L \mu_B L_z B_z = -g_L \mu_B L_z B_z T^1_{q=0}(\mathbf{L}_z) \cdot T^1_{q=0}(\mathbf{B}_z) \tag{2.30}$$

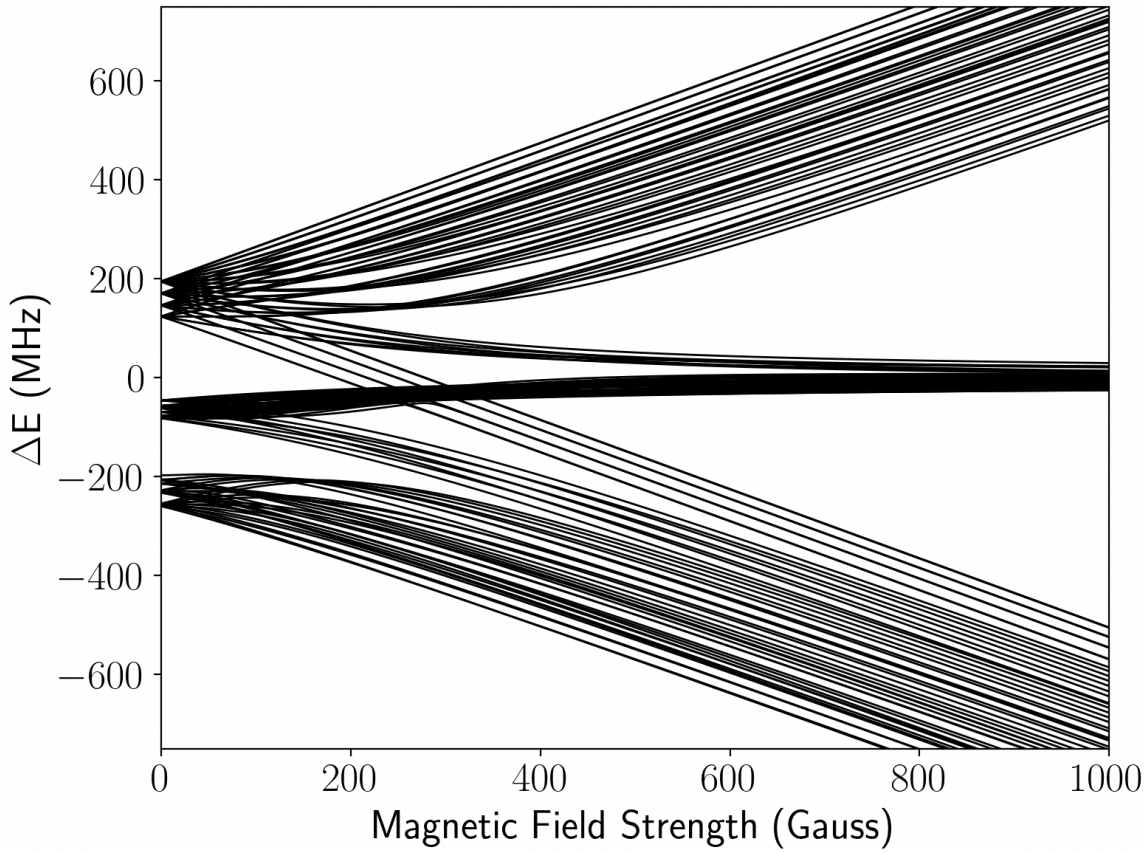

Figure 2.6: Calculated zeeman-splitting of the $A^1\Pi$ state[97]

where g_L, μ_B and L_z are the g-factor of the electron orbital angular momentum, Bohr magneton and projections of the electron orbital angular momentum onto the z axis. While we have not studied the Zeeman structure experimentally, shown in fig2.6 is a calculated $A^1\Pi$ state Zeeman structure.

Chapter 3

Experimental Setup

The key to most of the experiments presented in this thesis and to laser cooling of molecules in general is the buffer gas beam source of atoms and molecules which is different from any previous methods of producing atomic or molecular beams such as thermal effusion beams or supersonic beams. Thus in this chapter, we first present a discussion on molecule beams and our cryogenic buffer gas beam cell that is capable of producing both slow and bright beams of atoms and molecules.

3.1 Molecular Beams

Atomic and molecular beams are central to atomic and molecular physics and have been studied for almost a century so far since the times of Otte Stern. A detailed presentation of molecular beams can be found in a classical book by Norman Ramsey[98]. Here, we give a brief discussion to the essential ideas and methods relevant to laser cooling and trapping experiments with a comparison of the thermal effusive beams, supersonic

beams and cryogenic buffer gas beams, then we give a detailed description of our cryogenic buffer gas beams cell design.

3.1.1 Thermal Effusive Beams

Thermal effusive beam is one of the oldest ways of producing atomic beams. Essentially, it is an oven with a hole where sources are put in and a high enough temperature T is generated with the oven ususally by means of passing though a high electric current that causes resistive heating. The oven temperature is determined by the vapor pressure of different materials. Figure3.1 shows a thermal effusive source used in our lab. Stainless steel wires are used for its high resistivity to produce efficient heating. The use of tantalum foil here is to help create an even distributed heating with the oven due to the good thermal conductivity of tantalum and its low vapor pressure even at high temperatures relative to most metals, which is important for producing better collimated atomic beams. The advantages of such a beam source are that it is continuous, simple to make and as being effusive[1], there are limited number of collisions or none between the particles in the beam. Effusive sources have mean forward velocity characterized by $V_{mean} = \sqrt{2K_BT/M}$ where $T \approx T_{oven}$, which is the lowest compared to supersonic beams and buffer gas beams that we will discuss later. Typical mean forward velocities of such source for lighter metal atoms range from 500m/s to 2000m/s and 100m/s to 500m/s for heavier atoms. Molecules, being heavier in general, should have relatively low mean forward velocity, however thermal effusive beams are also high in temperature T[2]. Thus, although thermal effusive sources

[1]Effusive beams are typically beams with low fluxes and with no background gases such that there are low probabilities of collisions in the beam

[2]The temperature T defined for molecular beams should be in the reference frame of the molecules, thus with respect to the mean velocity

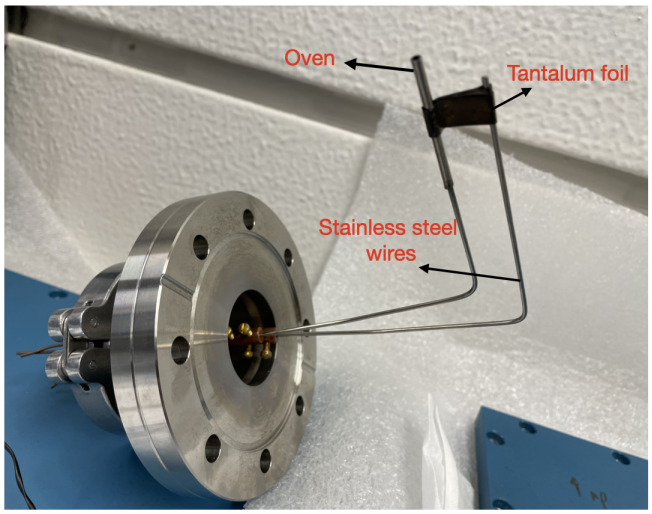

Figure 3.1: Oven source for producing atomic/ion beams

can produce translationally slow molecules, the molecules are internally mostly distributed in high ro-vibrational states, which greatly reduce the flux that are amenable to be laser slowed. Despite that there actually exist methods that can produce slow and low temperature beam sources by using velocity selective beam guides or turbines that can select the slow moving molecules which is only a small fraction[99]. The fluxes of these sources are too low to be used in cooling, trapping or any beam experiments.

3.1.2 Supersonic Beams

Supersonic beams are produced by mixing sources with inert noble gases at high pressures and then through a small(usually $<$ 1mm in diameter) hole, called nozzle into the region of interest, usually vacuum chamber for experiments. In general, as the gas

exits the small nozzle region, it undergoes an adiabatic expansion and cools down rapidly, which results in a low temperature and high flux, but a high forward velocity, typically $\approx 2.4\sqrt{2K_BT/m}$[100], where m is the mass of the background gas. Such sources are great for doing high precision spectroscopic experiments as it is high in flux and cools both the external and internal degrees of freedom of the molecules effectively, but not applicable in general to cooling and trapping experiments due to its high mean forward velocity.

3.1.3 Cryogenic Buffer Gas Beams

The ultimate goal for laser cooling and trapping or any other trapping experiments with molecules such as magnetic trapping is to create a beam that is both slow and cold, and more importantly that works independent of the species, i.e a versatile, general-working beam source. Fortunate to us, there has been tremendous developments in recent years on cryogenic buffer gas cooling which largely relies on a cryogenic buffer gas cell that we will discuss in detail in the next section. The technique has been demonstrated for a variety of species at its early development[101], with temperatures down to hundreds of mK and magnetic-trapping of molecules in-cell has been demonstrated[102]. However, the collisions between molecules and the buffer gas prevent it from precision measurement or manipulation on the molecules. Later on, further developments based on the cell have been made such that the cell only works as a beam source and the cell has an exit hole, behaving like a nuzzle. As the molecules collide with the buffer gas in the cell and thermalize, they also escape from the cell and depending on the density of the buffer gas. There are in general three cases. With low densities of buffer gas, the molecules experience much less collisions and exit as an effusive source, which is slow but not so cold since less collisions

also lead to less thermalization and further more, the flux is also low. At high densities, the molecules experience much more collisions that make the beam cold and result in a high flux, but they also experience a boost in the forward velocity that make them fast, like supersonic beams[103, 104]. The third case is densities of buffer gas in between of low and high, where there is hydrodynamic effect and thus called hydrodynamic regime. In the hydrodynamic regime, a beam that is both slow and cold can possibly be generated and in our experiments, we typically run in the hydrodynamic regime with a flow of helium buffer gas at 3 or 4 standard cubic centimeters(sccm).

3.2 A Two-stage Buffer Gas Beam Cell

The buffer gas beam cell lies in the heart of all the cryogenic buffer gas beam source setups and is the key to all our experiments. An illustration of a two stage cell is shown in 3.2 and figure 3.3 shows an actual picture of the two-stage cell in our lab. Figure 3.4 shows a single(first) stage cell. All parts in the main body of the cell are made out of oxygen free and high thermal conductivity copper(Cu101) with 99.95–99.99% copper and less than or equal to 0.0005% oxygen according to our supplier Sequoia brass&copper. All the parts are stacked together with four #8-32 threaded brass rods and stainless steel nuts with Belleville washers. Previously, we used stainless steel rods and nuts and realized that due to a lower thermal expansion coefficient of stainless steel than that of copper at 4K[105], the rods would shrink less than the copper and that can cause leakage of helium density in cell since the cells parts are potentially not as tightly stacked. Brass, on the other hand, has a high thermal expansion coefficient at 4K and thus becomes the choice of what we use

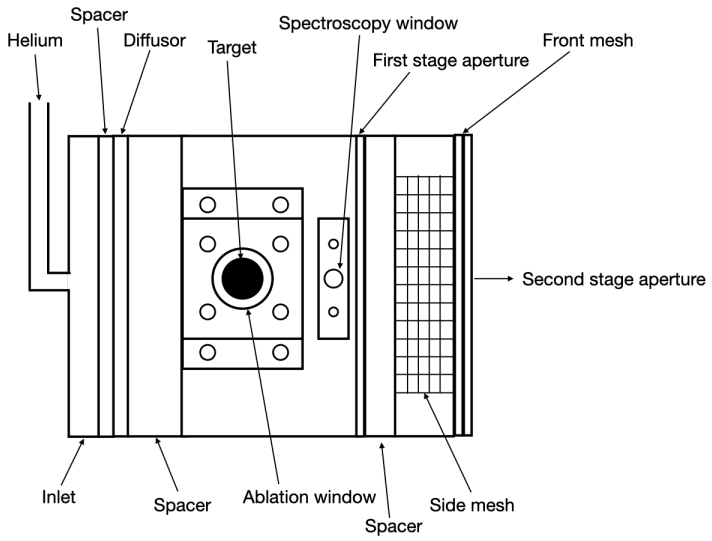

Figure 3.2: An illustrated two-stage cell for generating cryogenic buffer gas beam sources. Note that it is not meant to be on scale

now. Another important thing to note is that the roughness of the surfaces of copper can greatly reducing the thermal conductivity throughout the cell pieces(in face, through any metal to metal contact in the dewar), thus Apiezon vacuum grease which has good thermal conductivity is applied between all the interfaces of copper to copper contact. The following gives a detailed discussion of each part of the cell and how the molecular beam is generated.

The inlet and the buffer gas beam line

The first piece of the cell parts is the inlet of buffer gas that is connected with the the buffer gas beam line. A 1/8" inner-diameter copper tube is connected to the inlet

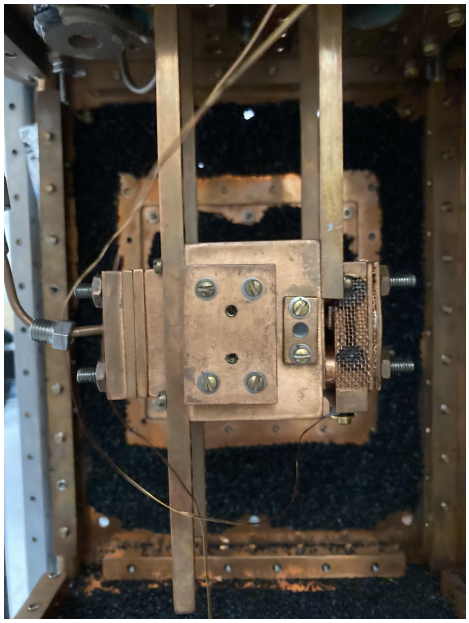

Figure 3.3: A full assembly of the two-stage cell

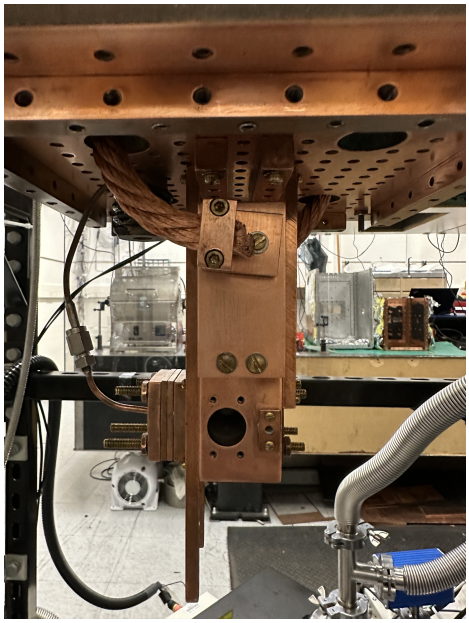

Figure 3.4: A single stage cell

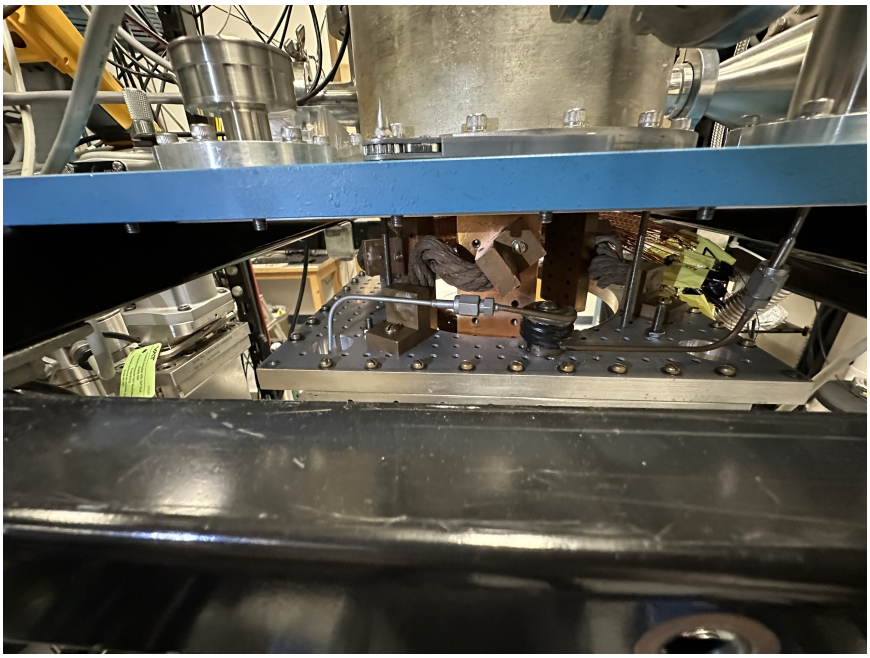

Figure 3.5: Stainless steel tube is used to separate buffer gas beam lines of stages of different temperatures

plate by brazing. The copper tube is then connected to another copper tube through a Swagelok VCR connection as can been seen in fig3.4 and the rest of the buffer gas lines are all connected via VCR connections. The high purity helium comes from a room temperature gas cylinder and it goes through an intermediate stage at 40K and then goes to the 4K lines. In order to separate stages of different temperatures, stainless steel(SS316) tubes are used in between as shown in fig 3.5.

Diffuser and Spacers

As the buffer gas exits the hole of the inlet plate, it will expand rapidly and be jet-like, i.e in the supersonic regime. The purpose of the cell is that it fills with the helium buffer gas that can thermalize with the molecules, thus a jet-like buffer gas beam would

Figure 3.6: diffuser, the outer dimension of the plate is 1.5” x 1/5 ” and the thickness is 1/8”. The diffuser itself is 1” in diameter

not work since it will exit the cell fast and the high forward velocities would also not be ideal. In order to create more uniformly distributed buffer gas in cell, we use a diffuser as depicted in fig3.6. The diffuser plate has an outer dimension of 1.5” x 1.5 ” and a thickness of 1/8”. The diffuser itself is a circle with a diameter of 1”. Before the diffuser, a spacer of thickness 1/8” is inserted to increase the area onto which the buffer gas stick to the copper wall before diffusing instead of just having a area equivalent to the size of the inlet hole and after the diffuser, a spacer of thickness 1/2” is inserted between the diffuser and the cell. This is to ensure that the buffer gas will fill the cell uniformly. Both the spacers have an outer dimension of 1.5” x 1.5” with a circular hole of 1” in diameter.

Main Cell

The main cell is where the buffer gas cooling happens, ideally with a uniformly filled high density buffer gas colliding with the molecules towards equilibrium. It has an outer dimension of 2" x 2" x 1.5" with a bore of diameter 1" along the buffer gas flow direction, perpendicular to it are two bores, one for the target holder and ablation window, the other smaller one for spectroscopy lasers. Attached after the main cell(in the buffer gas flow direction), is a plate for the aperture of the cell. It has an outer dimension of 1.5" x 1.5" and the aperture is a circular hole of diameter 5mm. The thickness of the plate is 1/16" and the shape of the aperture has a cone-shaped bore that is machined with a counter-sink of 45 degrees. This cone-shaped feature can enhance collisions bewteen the buffer gas and the molecules right before the molecules exit.

Washers

The washers used for the stacking of cell pieces are Belleville washers for its spring-like conical shape to support high forces with small deflections. We typically stack three washers in series to make sure the cell as a whole is held with versatility especially at low temperatures.

Target Holder

The target holder is a circular copper plate with thickness depending on where the surface of the target is roughly set to be relative to the center of the cell. We mostly set the target to be about 1/2" inch behind the center of the cell. The target is glued to the target holder by vacuum glue Stycast 2850 that has good thermal conductivity at 4K. The target

holder itself is mounted onto another plate which is mounted to the cell. As mentioned earlier, it is crucial to put Apiezon grease in between all the copper interfaces to enhance thermal conduction. Based on our experience with the yield of molecules after ablation, it matters the distance from the surface of the target to the center of the cell, however, no systematic investigation has been made regarding this. We also notice that other groups found that the orientation of the target relative to the ablation laser matters, but it is not a critical matter to us at the moment.

Ablation Window and the Snorkel

The window for the ablation laser could just be clamped to the main cell as the spectroscopy window. However, coating of the ablation window from ablation dust can greatly reduce the ablation pulse power and result in much less production of molecules. From our experience and other groups, this is usually the first factor to prevent experimental performance such that one needs to open the dewar and either clean or replace the ablation window. Thus, a snorkel of 1.5" is added so that coating of the window can happen in much slower rate. Another advantage for adding a snorkel is that the ablation laser is less focused at an earlier position and thus the window has a much less chanced to be damaged.

Second Stage Cell

The purpose of the second stage cell is that the density of the buffer gas greatly reduce and the molecules experience a second stage collision with a much lower collision rate(generally one collision per molecule) with the hope that a second group of thermalized molecules with much lower mean forward velocity ($\sim$ 60m/s or less) can be generated. The

second stage is first separated with the main cell by four circular nuts and then the beam goes though the main body of the second stage which is a block of copper with an outer dimension of 1.5" x 1.5" x 1/4". The block has a circular bore in the center with a diameter of 1". The two sides of the block both have a slit and a copper mesh is glued to the slits by Stycast. Finally, the aperture of the second stage is a mesh sandwiched by two 1/16" thick copper plates with indium added to enhance thermal conduction. The purpose of the mesh is that some molecules would be bounced back and experience more collisions with the buffer gas.

Previous studies have shown that the production of the beams depend on the cell geometry and a varieties of parameters[106] and yet there are still many unknowns about the cell, thus there are still improvements expected towards the cell design.

3.3 Experimental Apparatus

The experimental apparatus is depicted in fig 3.7. It consists of an overall of three parts, the cryogenic high vacuum chamber that is often referred to as the Dewar. The buffer gas beam cell is located in the heart of the dewar where the target is put and laser ablation on the target creates plumes of hot atoms and dusts and when an aluminum atom and chlorine atom collide and form a bound state, the radical AlCl is formed. Details of this process will be discussed in chapter 6. The hot plumes then thermalize with the helium buffer gas, forming a beam of mixture of helium and AlCl and Al, Cl atoms. Since the dewar is where the molecular beam is generated, everything else in the dewar is built for generating a slow and cold beam. The intermediate chamber is built to pump out more residue gases

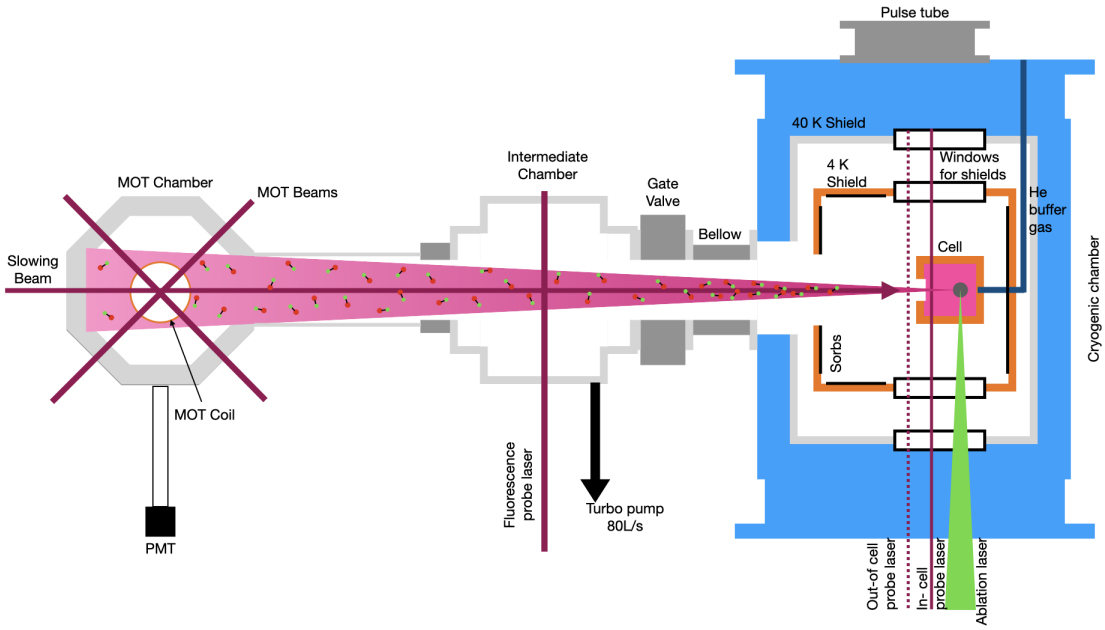

Figure 3.7: Overview of the experimental apparatus.

and help maintain a low enough pressure in the MOT region as well in order to increase the MOT lifetime. It can also be used to do intermediate stage probes. This is actually where we measured the hyperfine structure of the $A^1\Pi$ state. The last region downstream is the MOT chamber where we try to make MOTs of AlCl or any atoms and molecules of interests. This section gives a detailed discussion on all the parts of the experimental apparatus.

3.3.1 The Cryogenic Chamber(Dewar)

The cryogenic chamber is built based on a two stage cryogenic pulse tube, Cryomech PT420, that cycles helium. The pulse tube has two stages, one maintains temperatures at $\sim$ 40K and the second one at $\sim$ 4K. The outer most layer of the whole chamber is

a blue box made out of aluminum that is machined with ports for vacuum pump connections, temperature sensors, vacuum gauges, a mass spectrometer, view ports that contains windows for the transmission of the lasers and for the cryogenic pulse tube. All the ports on the blue box are KF connections with o-ring sealing except the one for an extension adaptor that is a CF connection with copper gasket sealing. The adaptor is there since the height of the pulse tube do not match where it should be in the dewar. An overview of the dewar is depicted in fig3.8

For buffer gas cooling to work, it is critical to reduce any possible black-body radiation from room temperature sources such as the blue box as the thermal radiation power is proportional to T^4. Thus, in order for the cell to maintain at temperatures as low as possible, two stages of radiation shields are built to fight against black-body radiation. The first stage is a rectangular box made of metal aluminum plates and covers all sides except holes for cables such the temperature sensors and openings for window frames. The shield box is attached to the top of the blue box by stainless steel all-thread rods to have thermal separation. The shield box is connected to the 40K stage of the pulse tube via $\sim$ 1 inch diameter copper braids which we call thermal links and the thermal links are brazed to copper blocks and the blocks are on both sides on the thermal links, one side attached to the 40k stage via an intermediate hexagonal extender and the other on the shield box as depicted in fig3.9. Inside of the aluminum 40K stage is the 4K stage shields. The 4K stage shields are made of copper plates and as the same case for the aluminum shields, we try to cover as much as possible areas in all sides except the holes and window frames needed for cables(only temperature sensors at this point in the experimental setup), gas lines and

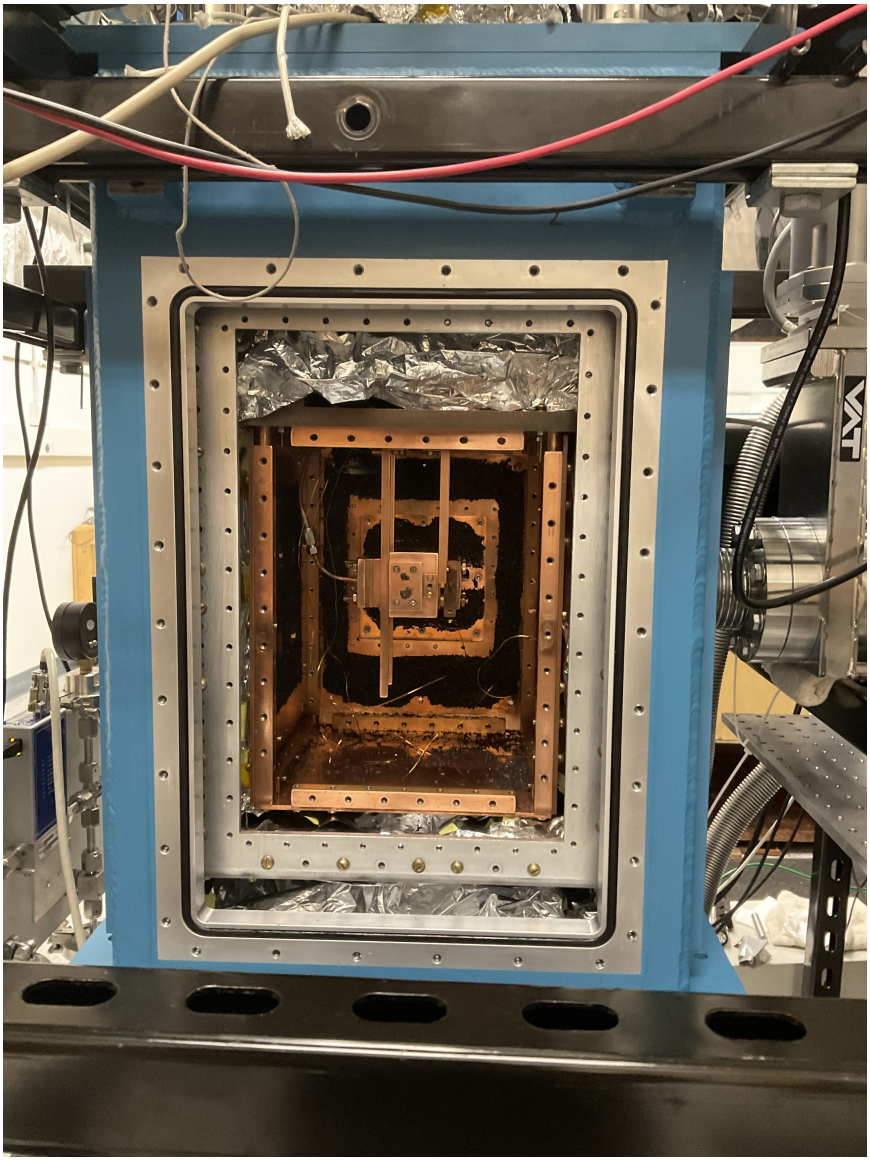

Figure 3.8: Overview of the dewar.

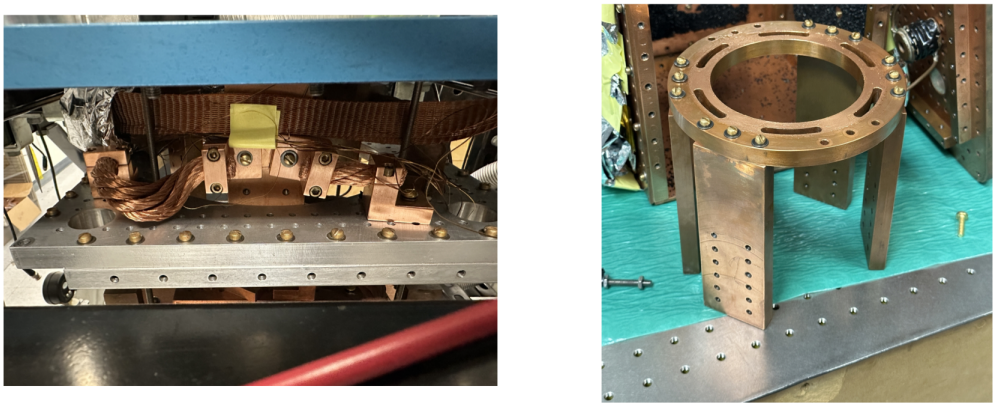

Figure 3.9: 40K copper braid heat links and the hexagonal extender

lasers to pass through. The 4K stage is hanged also by stainless steel all-thread rods to the top plate of the 40k stage in order for thermal separation and are thermally connected to the 4K stage of the pulse tube via thermal links. Another reason why we hang the shields by stainless steel rods to the blue box instead of attaching them directly to the pulse tube is that the pulse tube cannot take much strain and there is considerable chance of damaging it by hanging the shields. The details of the parameters of the pulse tube can be found in the manual of Cryomech PT420. The radiations shields by themselves are in fact not enough to fight against room temperature black-body radiation, so we also wrap layers of thins sheets of aluminum to both stages of shields. We call them super-insulation. In our experience, we found that attaching 5 to 10 layers works noticeably better than only a few

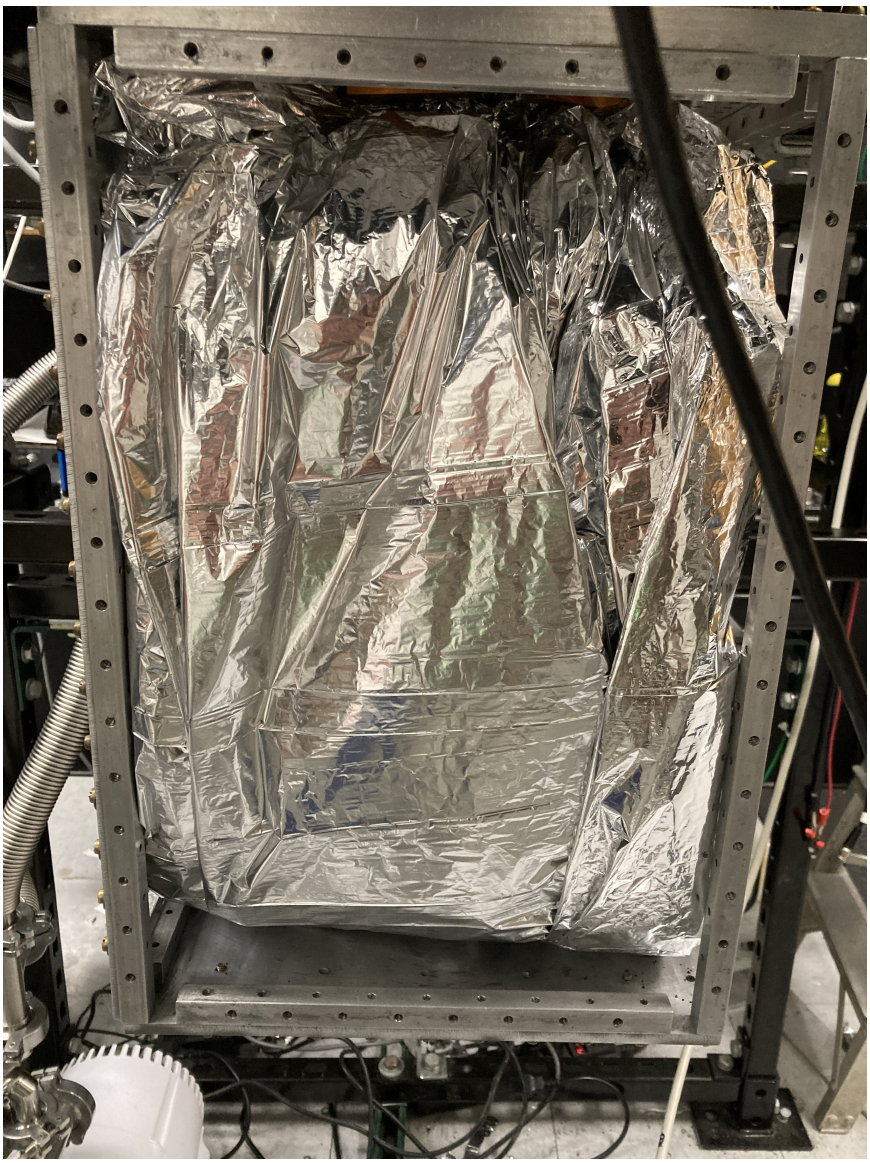

Figure 3.10: Super-insulation made of multiple layers of thin aluminum sheets to further reduce black-body radiation

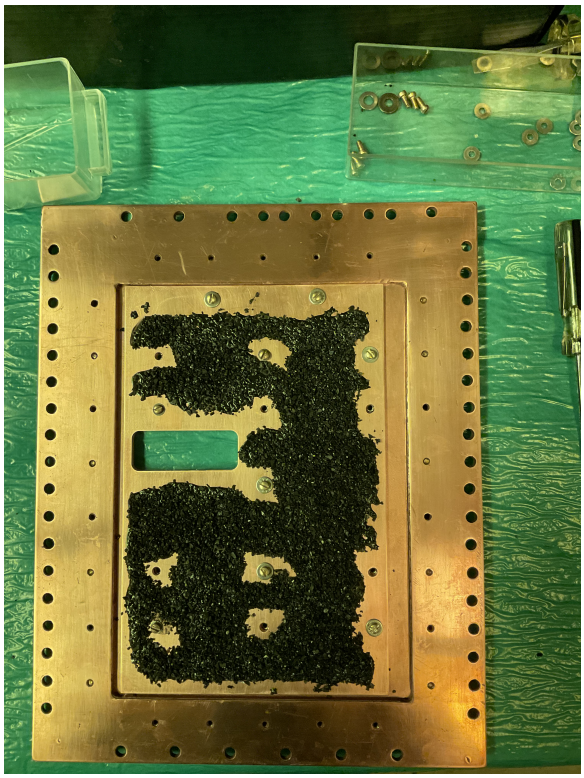

Figure 3.11: A sorb plate covered with coconut charcoal sorbs for cryogenic pumping. The sorbs are glued to the copper plate by Stycast.

layers less 5, depicted in fig3.10 is the super-insulation.

Since in our experiments, we typically need to flow buffer gas continuously, we choose to use cryogenic pumping. The basic principle of cryogenic pumping is that gases can be captured (or "pumped") by condensing, freezing, or adsorbing them onto a cold surface. Coconut charcoal, also referred to as activated carbon derived from coconut shells, which we typically call sorbs is used as our sorbent for its having large surface area, low outgassing rate, chemically stable and they become more effective at cryogenic temperatures due to large increase in the adsorbing coefficient. The sorbs are attached to the inside of the 4K shields by gluing them with Stycast. A sample of sorb plate with sorbs covering is

depicted in fig3.11. In order to replaced the sorbs more easily as we found the replacement is more often needed that previously thought, we modified our previous design to add the sorb plates to the shields.

By far, we have been saying temperatures of the two stages of the pulse tube as $\sim$ 40K and $\sim$ 4K, however, in experiments, temperatures are often important physical quantities such that knowing them in a precise manner is necessary and for our experiments to work, the lower the temperature of the cell, the better and it turned out that this is critical which we will be discussing shortly. Thus, when the dewar was first assembled, a temperature test was taken with no heat load(shields, cell, etc.) and only super-insulation was put to thermally separated the two stages and the outside. The plot 3.12 shows the result of the cooling down test. However, when we run experiments with typical ablation powers and helium flow rates, the temperature of the two stages of the shields are generally at $\approx$ 50K and $\approx$ 4.5K and the cell is generally at $\approx$ 4.2K and can go up to 4.5K. All are none ideal. The problem with the shield can be solved by attaching more layers of super-insulation. For the cell, we decided to connect the cell thermally directly to the 4K stage of the pulse tube with thermal links as depicted in fig3.13. This change has made the cell having a temperature dropped to 4K or below, which resulted in noticeably higher production of molecules than we ever had before. Besides the change on the thermal connection to the cell, we also added more heat links to both two stages of the shields. After all the changes made to successfully improve the temperature performance of the dewar, we did a buffer gas cooling test with Potassium(K) by extracting temperature through Doppler broadening fittings at different times after the ablation and the result shows successful buffer

gas cooling as depicted in plot3.14. A comparison with the previous demonstration of buffer gas cooling with Ytterbium(Yb) can be checked in the thesis[107].

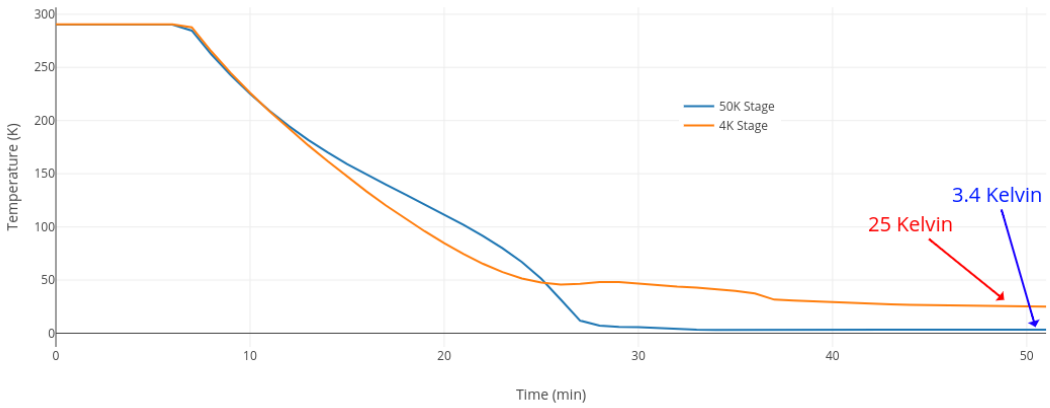

Figure 3.12: First cooling down test of the cryogenic chamber without any heat load. Super-insulation is used to separate the two pulse tube stages and the outside.

3.3.2 The Intermediate Stem Chamber

As depicted in fig3.7, in between the cryogenic chamber and the MOT chamber, there is an intermediate region, where a hexagon vacuum chamber with all ports of CF connections is placed. The main purpose of this region is to help maintain lower pressure in the MOT region which is critical the MOT lifetime and that is also why we call it the stem reion sometimes. It is attached with a turbo pump TwisTorr 84 FS from Agilent that has an average pumping speed of 80L/s and 63L/s for helium. The region can also be used as a probe region and we did the the $A^1\Pi$ hyperfine structure measurements in this region(details on this can be found in chapter 7). This region is also flexible, meaning it is

Figure 3.13: Direct thermal connection of the cell and the 4K pulse tube stage to increase cooling power for the cell

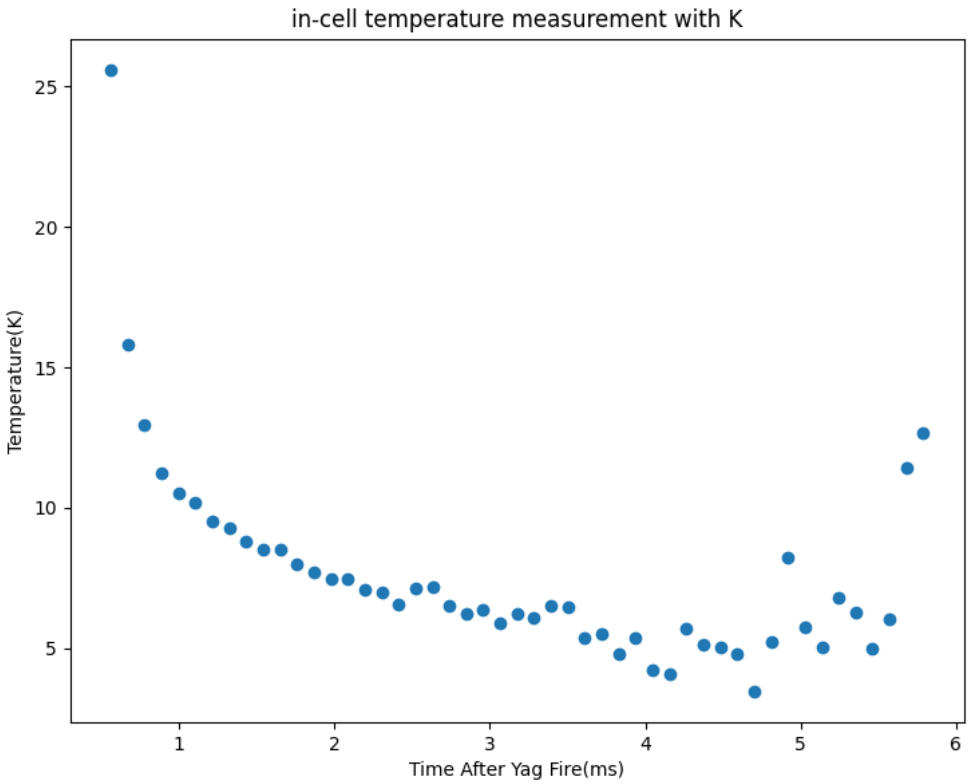

Figure 3.14: Demonstration of successful buffer gas cooling with Potassium(K) after improving thermal connections in the dewar, especially with adding a heatlink directly from the cell to the pulse tube 4K stage. The temperatures are extracted by Doppler broadening fittings at different times after ablation. The coldest point is ≈4.7 K and the temperature rises again at ≈4.8 ms after ablation.

relatively easy to be removed and attached. Removing it would cause a higher pressure in the MOT and decrease the MOT lifetime, however, it will significantly shorten the distance between the beam source and the MOT, thus increasing the beam brightness at the MOT.

3.3.3 The MOT Chamber

Downstream along the molecular beam direction, after the intermediate stem region is the MOT region which is an vacuum chamber of octagon on the side and both top and bottom have ports as well with all ports CF connections. With extension adaptors, six ports are for the MOT laser beams, two of the ports along the molecular beam directions is one for the molecular beam and the other for the slowing laser beam. Attached to the chamber is also a turbo pump TwisTorr 305 FS from Agilent that has an average pumping speed of 300L/s and 255L/s for helium. One port is used to insert the MOT coils. Details of the MOT coils can be referenced to thesis[107]. The typical pressure (with a helium flow rate 4sccm or less) when running the experiment in the MOT region is $\sim$ 3 x 10^{-7} torr.

3.3.4 Rough Pressure Vacuum Pumps

We have had a long struggle with the issues of having high pressures when running experiments. A high pressure would destroy the slow, cold molecular beam sources. From our experience, a working pressure for producing a slow, cold molecular beam is to have a pressure $\sim$ 5 x 10^{-6} torr in the cryogenic chamber and a pressure $\sim$ 3 x 10^{-7} torr in the MOT chamber when running experiemnts with typical flow rate of helium at 4sccm and ablation energy at 7mJ. However, what have happend long is that these pressures are generally seen right after a through cleaning in most parts in the dewat such as cleaning of

the cell, radiation shields and often with a replacment of new fresh sorbs, but after running experiments for a few days, the pressures ususally get one order of magnitude higher and this ususally destroys the slow, cold beams source. A major issue that we found that causes this is that the IDP Scroll pumps that we have been using is not good at handling water and water condenses and accumulates on the sorbs. Overtime, the scroll pump accumulates water as can be seen in fig3.15 and the pump efficiency decreases a lot. To solve this problem, we replaced the IDP scroll pumps with EBARA dry pump EV-A06-1 recommended by Prof. David Patterson at UCSB and the pressure maintains much better than before and we can now have a more consistent slow, cold beam source for a longer running time.

Figure 3.15: The IDP scroll pumps tends to accumulate water overtime and pumping efficiency decreases that causes the pressure to be one order of magnitude higher than working pressures.

Chapter 4

Laser Systems

4.1 Introduction to DUV Lasers

One of the biggest challenges on laser cooling of AlCl is that the main cycling transition is at wavelength ≈ 261.5nm in the deep ultra-violet(DUV) region of the electromagnetic spectrum and the most relevant re-pump transitions are also only a few nm away. Due to their short wavelengths, DUV lasers have a plethora of applications in industry, medicine[108, 109] and scientific research, especially if they can be controlled precisely. One of the most significant applications of DUV lasers is in photo-lithography for semiconductor chip manufacturing. The shorter wavelength allows for the creation of smaller features on silicon wafers, contributing to the ongoing miniaturization of integrated circuits. They can also ablate materials with high precision, making them ideal for micro-machining, structuring of thin films, and patterning of delicate surfaces without significant heat damage. In terms of medical applications, DUV lasers can be used in refractive eye surgeries because they can precisely remove corneal tissue without causing significant thermal damage. For

scientific research, many molecules have electronic transitions in the UV region of the electromagnetic spectrum, including AlCl, thus high resolution spectroscopy can be done to study properties of such molecules. However, DUV light sources, both lasers, and LEDs, have challenges associated with the materials used. The aggressive nature of DUV radiation can degrade optics and other components over time, necessitating specialized materials and coatings.

4.2 Challenges for Laser Cooling at DUV wavelengths

Not only technologies are not as developed for DUV lasers as for wavelengths towards infrared, The nature associated with laser cooling at DUV range also provides another challenge. If we take the picture of a two level system, the saturation intensity is given by

$$I_{sat} = \frac{\pi hc\Gamma}{3\lambda^3} \tag{4.1}$$

Thus $I_{sat} \propto 1/\lambda^3$. For AlCl, the natural linewidth of the cycling transition $\Gamma/2\pi \approx 30$MHz and the transition wavelength $\lambda \approx 261.5$nm. Putting in the numbers then we find that the saturation intensity for this transition is $I_{sat} \approx 219\text{mW}/cm^2$. As comparisons, the saturation intensities for transitions at wavelengths towards infrared for example for CaF is $I_{sat} \sim 15$mW and for ^{87}Rb, even smaller at $I_{sat} \sim 2.5$mW. The saturation intensity for the main cycling transition is one or two orders of magnitude higher than typical atomic and molecular species for laser cooling. However, producing high powers of DUV light is not a mature technology, but recently, the McCarron group at University of Connecticut with their colleagues have figured out a way to produce Watt-level DUV laser light by frequency

quadruple a 1046nm IR light source[110]. For us, the pathway towards a high power, aimed at hundreds of mW of DUV laser light is first chosen to be frequency doubling a stable high power (up to 2W) commercial ECDL laser from Vexlum VALO SHG SF at 523 nm. At the same time, we are also building a similar system to the frequency quadrupled IR light source at 1046nm as the system in the McCarron group. Nevertheless, for the purpose of laser cooling and trapping of AlCl, there are still many unknowns such as the $A^1\Pi$ state hyperfine structure and the resolution with previous spectroscopy results especially at lower states that are relevant to laser cooling is not precise enough, thus further investigation of low temperature high resolution spectroscopy is needed in the first hand and it does not require much power to do spectroscopy, so our first system to produce UV light is a Titanium:Sapphire (Ti:Sapph) laser frequency tripped and we choose Ti:Sapphs for their wide-tunnability such that they not only can be frequency tripped to get 261.5nm for AlCl main cycling transition, but also can be tuned to nearby re-pump transitions for example 265nm for the first dominant re-pump line. Furthermore, the frequency doubled Ti:Saph can cover a wide range of atomic species such as Ytterbium, Molybdenum, Manganese and so on so that we can try direct loading of MOT of such species if our two-stage cell works appropriately.

4.3 The Titanium:Sapphire Laser Systems

The Ti:Sapph laser is a widely used class of tunable solid-state lasers that produces output in the near-infrared region, typically between 700 nm and 1100 nm. It combines the broad tunability and pulsed operation capabilities that make it a workhorse for a variety of

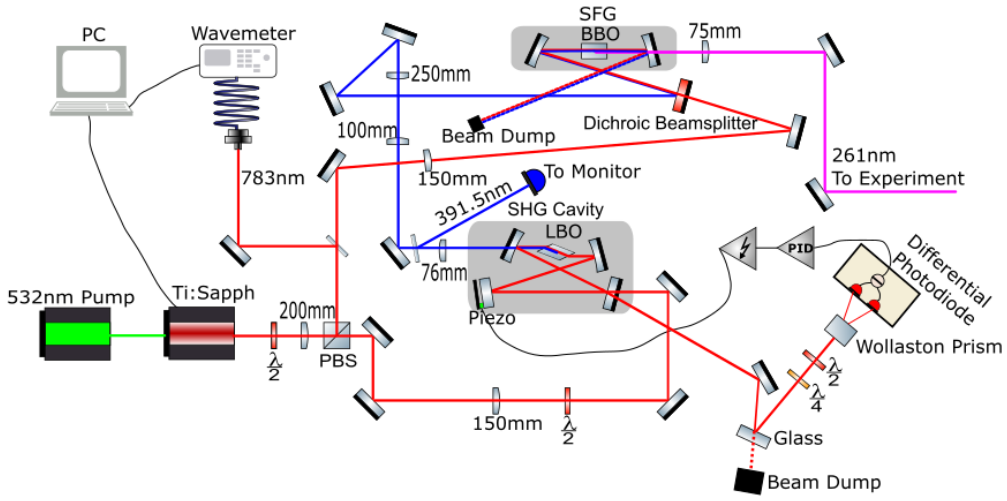

Figure 4.1: Schematic of the Ti:Sapph laser system that generates UV light from third harmonic of the Ti:Sapph fundamental frequency[69].

scientific applications. The gain medium is a sapphire (Al_2O_3) crystal doped with titanium ions (Ti^{3+}). This medium is responsible for the wide tunability of the laser. We have two Ti:Sapphs in use and both of them are pumped by the Sprout-H lasers from Lighthouse Photonics with one pump goes up to 18W and the other up to 12W. A schematic of the optics setup to produce the third harmonic of the Ti:Sapph fundamental frequency is depicted in fig4.1. The Ti:Sapph is a Coherent 899-21 model and it is pumped by a diode-pumped solid-state laser (DPSSL) that operates in continuous-wave (CW) mode to produce a high power, collimated, green beam from Lighthouse Photonics called Sprout. The Sprount pump lasers can operate up to 18W although we find that the output of the Ti:Sapph saturates at 14W pump and the maximum output of the Ti:Sapph is $\approx$ 2W when everything is optimized.

The fundamental IR laser beam that comes out of the Ti:Sapph first goes through a half-wave plate(HWP) and polarized beam splitter(PBS) pair to be polarization split. A larger portion of the light is sent to the second harmonic generation(SHG) cavity and the rest is further split to send as least amount as possible to the wavemeter for the frequency to be read out for frequency locking and the other portion goes into the sum frequency generation crystal to combine with the output from the SHG cavity to get the third harmonic of the fundamental. The larger portion of the light then goes through two lenses with focal length 200mm and 150mm respectively to get the desired beam waist inside the SHG cavity. The HWP after the second lens is for the purpose of making the light mostly P-polarized to couple into the cavity to match the Brewster-angle in-couple property of the non-linear lithium triborate LiB_3O_5(LBO) optical crystal for the SHG process, however, the light is never fully P-polarized, which is in fact critical for the method of frequency locking of the second harmonic cavity, Hansch-Couillaud locking method[111]. The Hansch-Couillaud method relies on detecting the slope of the cavity's resonance as light frequency scans across it. This slope provides an error signal that is inherently linear near the cavity's resonance. A small amount of polarization rotation is introduced to the beam before it enters the differential detector, typically using a quarter-wave plate. When the laser is off-resonance with the cavity, the introduced ellipticity in the polarization results in different reflection coefficients for the two orthogonal polarization components. By detecting the difference between the two orthogonal polarization states of reflected light using a differential photodetector, an error signal can be derived. The error signal looks like a dispersive signal of the cavity resonance. When the laser is on one side of the resonance, the error signal is

positive, and when it is on the other side, it is negative. When the laser is on resonance with the cavity, the error signal is zero. The error signal can be fed back into the cavity's frequency control system. In our system, we control the length of the SHG cavity by a PID control micro-controller Red Pitaya to lock the error signal to near zero voltage. The feedback loop acts to minimize the error signal, thus locking the in couple laser frequency to the resonance of the cavity. The reason why we want to lock the in couple laser frequency to the resonance of the cavity is to produce as intense as possible fundamental frequency light in cavity to maximize the SHG process that happens in the non-linear optical LBO crystal. Here, we give a brief introduction to the SHG process and explain why intensity is critical for it to work. For a thorough treatment of SHG, readers can refer to the book[112]. SHG is a nonlinear optical process where two photons with the same frequency ω_1 interact within a nonlinear material, combine, and generate a new photon with twice the energy and, consequently, twice the frequency $\omega_2 = 2\omega_1$ and half the wavelength of the original photons. It's one of the simplest and most widely utilized processes in nonlinear optics. Unlike linear optical processes which obey superposition and are independent of light intensity, SHG depends on the intensity of the light, because SHG arises from the nonlinear susceptibility of the medium as the polarizibility of a material depends on applied electric field in the following way[112],

$$P(t) = \epsilon_0 \chi^{(1)} E(t) + \epsilon_0 \chi^{(2)} E^2(t) + \epsilon_0 \chi^{(3)} E^3(t) + ... \tag{4.2}$$

where ϵ_0 is the permittivity of free space. $\chi^{(1)}$, $\chi^{(2)}$, $\chi^{(3)}$... are the first, second, third and higher order susceptibility of materials. $\chi^{(1)}$ is ≈ 1 and higher order $\chi^{(n)}$ is $\propto 1/E^{n-1}$. The characteristic atomic electric field strength is $E = e/4\pi\epsilon_0 {a_0}^2 \approx 5.14$ x 10^{11} V/m, thus $\chi^{(n)}$

decreases dramatically with increasing order. During an non-linear optical process, a laser beam has electric field associated with it in general as,

$$E(t) = Ee^{-i\omega t} + c.c. \tag{4.3}$$

Where *c.c.* stands for complex conjugate. As the laser light interacts with the optical crystal, the second order induced polarization $\mathrm{P}^{(2)}(\mathrm{t}) = \epsilon_0 \chi^{(2)} E^2(t)$, plugging in equation 4.3 for $E(t)$, we have,

$$P^{(2)}(t) = 2\epsilon_0 \chi^{(2)} EE^* + (\epsilon_0 \chi^{(2)} E^2 e^{-i2\omega t} + c.c) \tag{4.4}$$

Since radiation is general proportional to the second derivative of $P(t)$, we see that the second term of equation 4.4 generates radiation in the second harmonic with frequency 2ω and it is proportional to E^2, and since the intensity of radiation $I \propto E^2$, the second harmonic generation is proportional to the intensity of the applied laser light. The intensity is in fact critical since the second order susceptibility $\chi^{(2)}$ is orders of magnitude smaller that $\chi^{(1)}$. Thus, in our setup, it is critical to have the desired beam waist in the cavity which can be shaped by the 200m and 150mm lenses. We also use two curved mirrors, one right before the laser beam couples into the crystal and one as the output coupler to ensure that the intensity is as high as possible coupling into the optical crystal. Besides the intensity of in-couple laser light, for efficient SHG, the generated second harmonic wave should be in phase with the driving waves to constructively build up the second harmonic signal. Due to dispersion in materials, the phase velocities of the fundamental and the second harmonic light may differ. This leads to a phase mismatch, which can hinder the SHG process. To overcome this, we have a home-built crystal stage that can be angle tuned in three axises, temperature are also important to ensure the two waves propagate with the same phase

velocity and to keep water accumulation into the crystal, however, we have not built in a temperature control system for the crystal yet. Once we have the successfully generated second harmonic of light in blue, the TEM00 output mode always displays an elliptical shape that has the longer axis parallel to the optical table, thus we use a 76mm cylindrical lens that only has curvature in one axis to shape the beam closer to a circular beam. The beam is picked up a tiny amount to a photo-detector to be monitored as an indicator for the second harmonic generation process. The majority of the blue beam is then directed through two lenses of focal length 100mm and 250mm to be beam shaped and couples into the sum frequency generation optical crystal which is a Beta Barium Borate (BBO) crystal[1] to be combined with the fundamental IR beam to generate the third harmonic DUV light for the experiments. Sum Frequency Generation (SFG) is a second order nonlinear optical process in which two photons with frequencies ω_1 and ω_2 interact in a non-centrosymmetric medium to generate a photon with a frequency $\omega_3 = \omega_1 + \omega_2$. It is similar to the SHG process described, but with the electric field of the two photons different. Since the second harmonic blue and the fundamental IR beams couple in from different directions, a dichroic beamsplitter is used to reflect the blue beam and another mirror is used to reflect the IR beam and pass through the dichroic beamsplitter. As for now, only to curved mirrors are used for the SFG setup, meaning it is a single pass and not an cavity to enhance the in-coupling beam intensities. This is due to additional challenges on having two different frequencies resonant in the same cavity simultanously, which will be discussed in chapter 8. Nevertheless, the power we get from the single pass SFG is enough for spectroscopy

[1]BBO is transparent in wide range from the ultraviolet (about 190 nm) to the near-infrared (around 3500 nm). It has a high damage threshold, however, it is hygroscopic, meaning that it can absorb moisture from the air.

experiments. The final third harmonic DUV light is shaped by one 75mm lens and then directed to experiments.

4.4 The Vexlum VECSEL laser system

The Ti:Sapph systems are beneficial for their wide wavelength tunability, however, it lacks power when it comes to the generation of UV at the third harmonic, since in general, the conversion efficiency of non-linear optical process decreases as the order goes up. In addition, the SFG is not yet a closed cavity, we typically get $\sim$ 100uW UV light, that is sufficient for doing spectroscopy, but far from sufficient power for laser cooling and trapping AlCl. The estimation of laser cooling at UV is discussed in a previous section and a detailed estimation for the power needed for laser cooling AlCl will be discussed in chapter 7. Our first and current approach to get high (aimed at hundred of mW) power UV light at the cycling transition is to frequency double a vertical external cavity surface emitting laser(VECSEL) that can produce stable high power green light at 523nm that can go up to 2W, which is commercially bought from VEXLUM. Although it has a limited wavelength tuning range of $\pm$ 0.25nm, it provides highly stable laser light in terms of both frequency and power, and the fundamental IR light inside of Vexlum has an output that can be used to lock and tune the frequencies, which we currently use to lock to a frequency comb(Toptica DFC Core 80). Fig 4.2 depicts a schematic of the optics setup of the Vexlum laser system. The setup is in essence similar to the second harmonic part of the Ti:Sapph laser systems. The fundamental 523nm green light first goes through a pair of lenses with focal length 150mm and 75.6mm to ensure the desired beam waist inside the SHG cavity. The half-wavelength

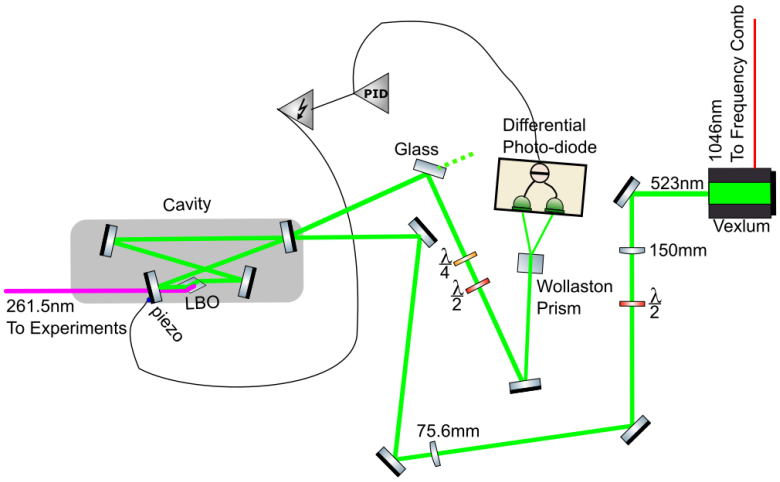

Figure 4.2: Schematic of the optics setup of the Vexlum laser system that generates second harmonic light from the 523nm fundamental green light.

plate in between the lenses are used to make the in-couple green light as P-polarized as possible to match the Brewster angle in-couple property of the LBO crystal. The locking method we employ is also Hansch-Couillaud. However, we have had a long struggle with getting stable lock of this cavity, and when it was locked, it used to be only able to lock for no more than one hour time scale. Our suspicion was largely two causes, one being that the optical crystal absorbs moisture too much that it changes the optical properties of the crystal and the other being that the intense in-couple green light heats up the crystal in some random manner such that the optical properties of the crystal changes as temperature fluctuates so much. Furthermore, the dusts in the lab also disturbs the in-couple light since they can scatter light and the dust can also be adhere to the crystal surface. To solve the problem with the moisture and dust, we built a plastic-box enclosure with ports open for the laser beams and cables, and connected to the box is also a 1/4" diameter plastic tube to flow dry-air into the box with opening for air displacement to have circulated air flow inside to

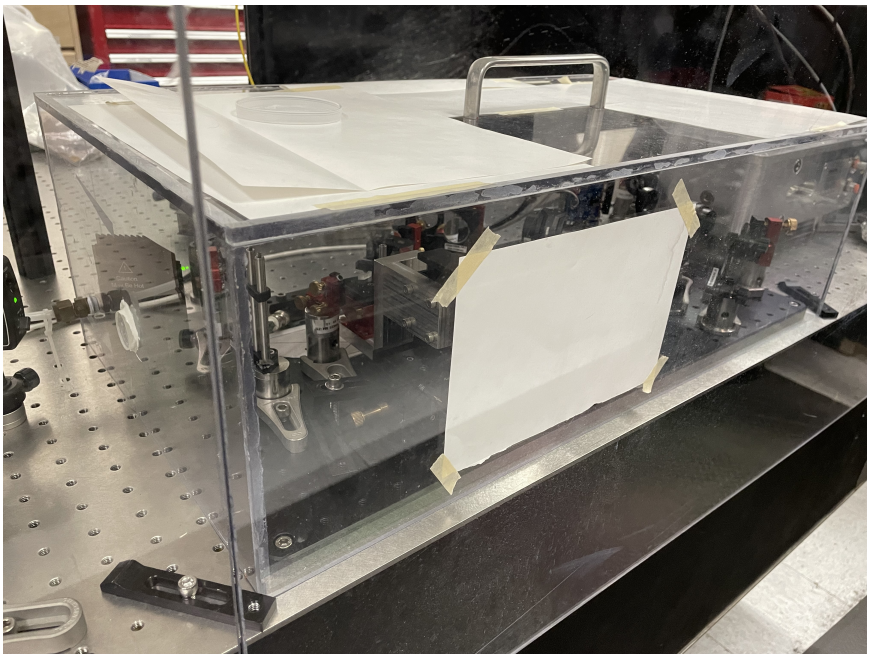

Figure 4.3: The plastic box with dry air circulation filling the box is built to prevent dust and moisture

avoid pressure built-up and have constant dry air environment inside, as depicted in fig4.3. The box protection with dry air environment clearly help maintain a clean dry environment inside as can be seen a clear green light beam with no dust being visible shown in fig4.4. At the same time, we also changed our strategy for locking from a continuous locking to pulsed locking for only the duration of an experiment after ablation. The combination of the box with pulsed locking are able to produce relatively stable locking for the cavity for hours running experiments as for now. However, we have not implemented a temperature control system yet as the same case for the Ti:Sapph laser system.

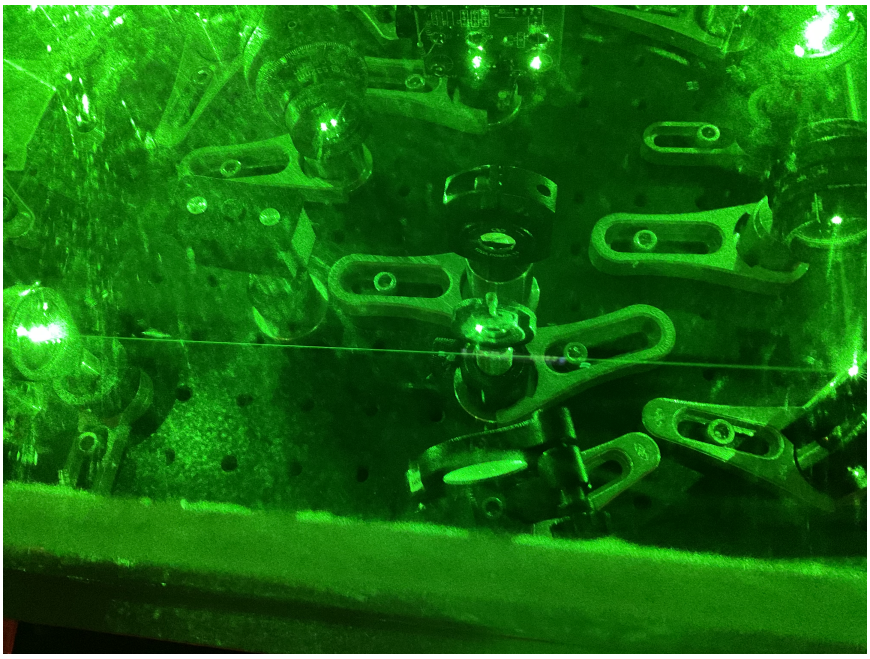

Figure 4.4: After installing a plastic box protection with dry air environment inside, clear beam of green light can be seen with no visible dust around

4.5 Laser Lock

Atomic and molecular physics experiments generally use lasers to study or manipulate atoms and molecules. Creating a frequency reference, and locking the lasers which means to stabilize the frequency of the lasers to the frequency reference is critical. This section describes our solution to this problem.

For all the experiments performed so far in our lab, we rely on a wavemeter, HighFinesse WS7 to read out the frequency of our lasers. The optical components in the wavemeter can change due to fluctuations of temperature, humidity, air pressure and so on, resulting a drifted frequency readings overtime, thus frequent calibration of the wavemeter with a stable frequency reference is critical. We use a Helium-Neon(He-Ne) laser to calibrate the wavemeter since it is stable from a day to day base, and has a well measured frequency.

The initial calibration of the wavemeter by the company was using a stabilized He-Ne laser with accurate 632.990890 nm wavelength. However, the He-Ne laser is free running and it also fluctuates with temperature, pressure and so on, thus we need a more stable reference to calibrate the He-Ne laser as well. Our choice is to do saturation absorption spectroscopy on the hyperfine transitions of the Rubidium(Rb) D2 lines since they are narrow and they have been measured accurately[113, 114]. We typically use a few of them to make sure of the accuracy, especially that we do not know whether the frequency offset of the wavemeter is linear. An example of the saturation absorption spectroscopy of Rb for the calibration is shown in 4.5. Since we do not know how linearly the offset of the wavemeter is with respect to a specific calibration frequency of the He-Ne. In the first place, we did a systematic calibration scans with a range of calibration frequencies and got a relation as such,

$$f_{offset}[MHz] = 0.797 * \Delta f_{HeNe,set}[MHz] - 16.826[MHz] \tag{4.5}$$

Where $\Delta f_{HeNe,set}[MHz]$ is the difference between the actual He-Ne frequency and the calibration frequency the user told the wavemeter. Thus every time we do calibration, we extract the f_{offset} from the Rb saturation absorption spectroscopy scan and then plug into the above relation to get the current He-Ne frequency.

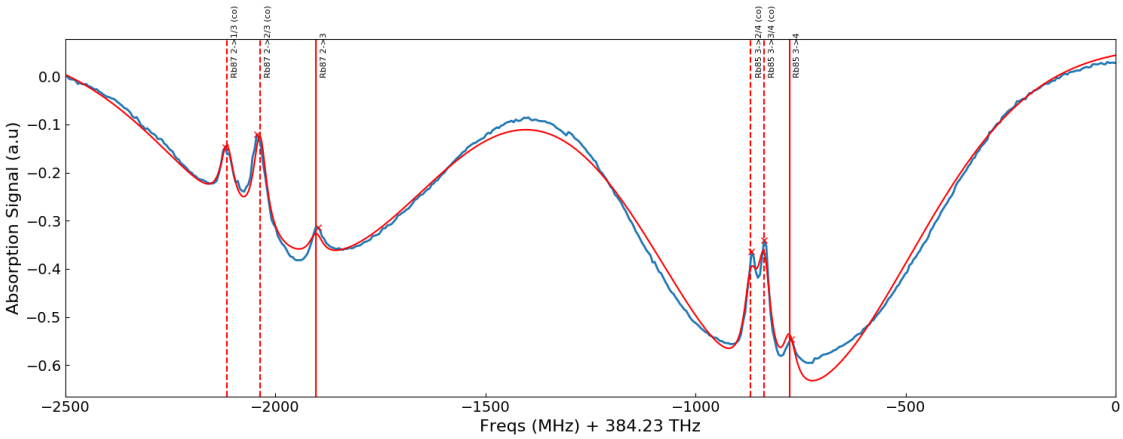

Figure 4.5: An example of the Rb saturation absorption spectroscopy for calibrating the He-Ne and subsequently the wavemeter

Chapter 5

AlCl Characterization with In-cell Absorption Spectroscopy

AlCl is predicted to have highly diagonal Frank-Condon factors[80, 81, 56] which is critical for laser cooling of molecules to work, however, the FCFs of the most relevant transitions, namely the main cycling transition $A^1\Pi(v'=0) \leftrightarrow X^1\Sigma^+(v=0)$ and the dominant re-pump transition $A^1\Pi(v'=0) \leftarrow X^1\Sigma^+(v=1)$ have not been experimentally estimated because the previous spectroscopy studies[77] were not carried at few Kelvin temperatures where the ground and low-lying states can be resolved with high enough precision to extrapolate the relevant molecular constants. With our cryogenic helium buffer gas beam setup that was discussed in chapter 3, we were able to carry out in-cell absorption spectroscopy measurements on the $A^1\Pi \leftarrow X^1\Sigma^+$ with high resolution that enables us to quantitatively characterize AlCl to an unprecedented level with a rigorous estimation of its $A^1\Pi$ state molecular constants and Frank-Condon factors. We also compared our experimental results

with a high-level *ab initio* calculation of the electro-rovibrational enegies of AlCl by our collaborators. The good agreements between our experimental results and the *ab initio* calculation results with an estimated FCFs of 99.88% of the $A^1\Pi(v' = 0) \leftrightarrow X^1\Sigma^+(v = 0)$ transition renders AlCl indeed an excellent candidate molecule for laser cooling. In this section, we detail our in-cell spectroscopy experiments, discuss our data analysis procedures and present the results of the molecular constants and estimated Frank-Condon factors.

5.1 In-cell Absorption Spectroscopy Experimental Procedure

The in-cell spectroscopy measurements are all performed in the cryogenic buffer gas chamber as depicted in fig 3.7. To do spectroscopy measurements, gas-phase AlCl needs to be created. We generate gas-phase AlCl by laser ablation of a solid target. The solid pellet target(details of the procedure of making the targets and a systematic study on the different chemical composition of the target regarding the yield of AlCl is discussed in the next chapter.) is ablated by a pulsed 532nm Nd:YAG (Continuum) laser with a pulse duration of 5±2 ns and typical pulse energy ≈ 10mJ. The width of the laser pulse is ≈ 80um at the target. The hot ablation plume has Al, Cl atoms, ions and AlCl molecules through collisional combinations of Al and Cl. Meanwhile, there are dusts due to ineffective ablation. Both the dusts and aluminum atoms can coat the ablation window. Thus we add a snorkel to keep the ablation window away from main cell to avoid coating. However, coating of the ablation windows still remains a major factor that forces us to open the Dewar after running some experiments. Throughout the experiment, helium buffer gas is flowing into the cell and collide with the hot ablation plume to resulting in a cold gas-phase

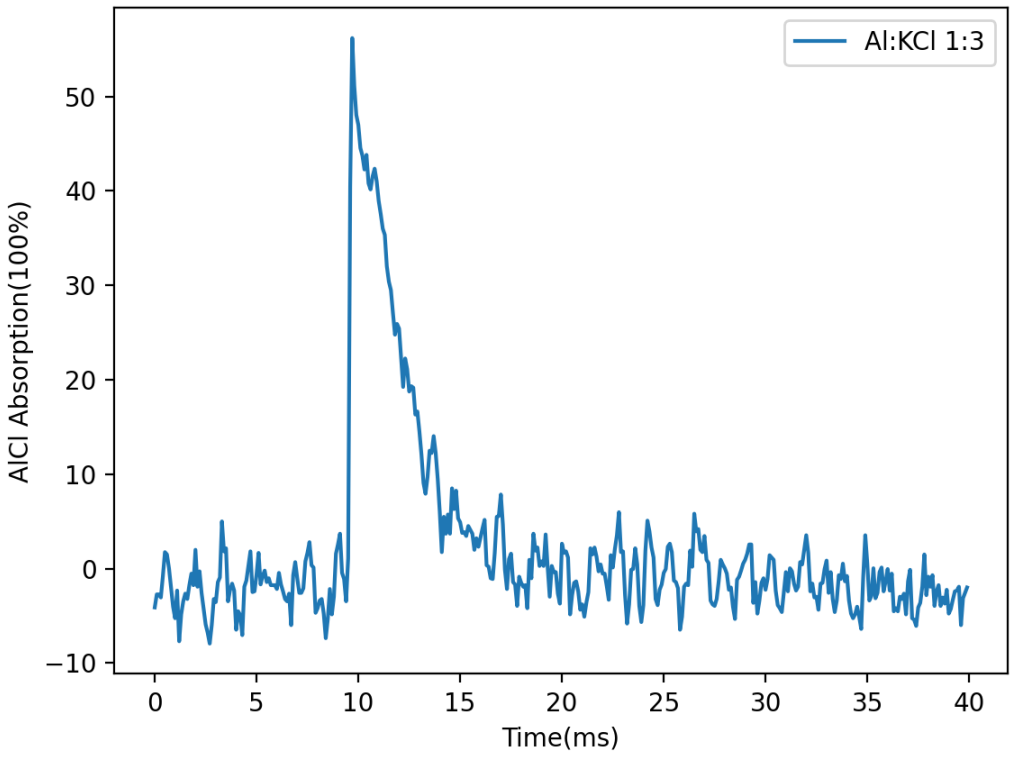

Figure 5.1: Sample absorption time trace of a Q transition of $Al^{35}Cl$. The laser ablation happens at 10ms. The target is a Al+KCl mixture of molar ratio 1:3.

AlCl along with background gas. A collimated tunable UV spectroscopy beam is directed through the cell passing a 3 mm thickness glass window with UV transmission coating and detected after the cell by an amplified photodiode (Thorlabs PDA25K2). The interatction of the spectroscopy laser beam with the molecular beam is $\approx$ 1.9cm downstream from the ablation point. A sample of an absorption time trace is shown in fig5.1. In order to have a better signal-to-noise ratio and avoid any artifacts in single shots, we typically do averages of 10 or more. Each shot(one complete experimental sequence) is repeated at $\approx$ 1Hz with a single experiment lasts $\approx$ 43ms for the cell to cool down again after each ablation. We also

raster the last mirror of the ablation laser setup continuously with an actuator (Conex CC, New Focus) on both the mirror axes to avoid drilling a hole in the target and have more consistent ablation yield. Prime numbers of steps on both axes shall be chosen to maximize the raster area on the target surface.

5.2 In-cell Absorption Spectroscopy Experimental Results

5.2.1 Data Fitting Procedure

The ultimate goal for our spectroscopy measurements is to get the molecular constants and Frank-Condon factors that are relevant to the laser cooling states. Thus, proper fitting to the spectroscopy data is crucial. The first step before fitting any data is to calibrate the wavemeter offset with saturation absorption spectroscopy of the Rb hyperfine lines and the He-Ne laser. The procedure for this is discussed in chapter 4.

After making sure that the wavemeter offset is taken into account. We can then fit each transition line individually by considerations of various line broadening mechanisms. The most dominant line broadening mechanism in our spectroscopy measurement is the Gaussian broadening associated with the Doppler shift frequencies due to the velocity distribution of the molecules in cell at still yet a finite temperature(estimation of the rotational temperature will be discussed). The next largest line broadening mechanism is pressure and collisional broadening that is due to a high pressure built up by the helium buffer gas and the ablation plume. The pressure due to the helium buffer gas per sccm is estimated to be 0.181mTorr per sccm[107]. Pressure broadening is generally described by Lorentzian broadening. Thus, Voigt broadening, which convolves both the Gaussian and Lorentzing

broadening is used to fit the line centers.

Once we obtain all the measured and fitted line centers, a least-square fitting method can be used to fit the Dunham coefficients with the Dunham model,

$$E_{vJ} = \sum_{kl} Y_{kl}(v+1/2)^k[(J(J+1)) - \Lambda^2]^l \tag{5.1}$$

Where Y_{kl} are the Dunham coefficients and Λ is 0 for the $X^1\Sigma^+$ state and 1 for the $A^1\Pi$ state. To fit for the $A^1\Pi$ state Dunham coefficient from measuring the $A^1\Pi \leftarrow X^1\Sigma^+$ transition, one also needs to know the relevant $X^1\Sigma$ state Dunham coefficients, for which we adopt the values from a high-resolution infrared spectroscopy studies on AlCl[94].

5.2.2 Rotational Temperature

To gain insights of the thermalization of the internal degrees of freedom of AlCl, we extract the rotational temperature in cell from the P-transitions of $Al^{35}Cl$ in the $v = 0$ vibrational branch since the data was taken within the same day, same target and minimized fluctuations of the experimental conditions are expected. The absorption of the P-transitions as a function of the $X^1\Sigma^+$ state quantum number J is shown in fig5.2. The $X^1\Sigma^+$ rotational state population is determined by the Boltzmann distribution as,

$$N_J \propto (2J+1)e^{-E_J/(k_B T)} \tag{5.2}$$

where $E_J = B_v J(J+1)$ is the rotational energies and $B_v \approx Y_{01} + Y_{11}(v+1/2)$ is the vibration dependent rotational constant. Besides the rotational population distribution, the transition line strengths also depend on the rotational transition dipole matrix element, which is described by the Honl-London factor, given by[115],

$$S_J = \frac{(J-\Lambda-1)(J-\Lambda)}{2J} \tag{5.3}$$

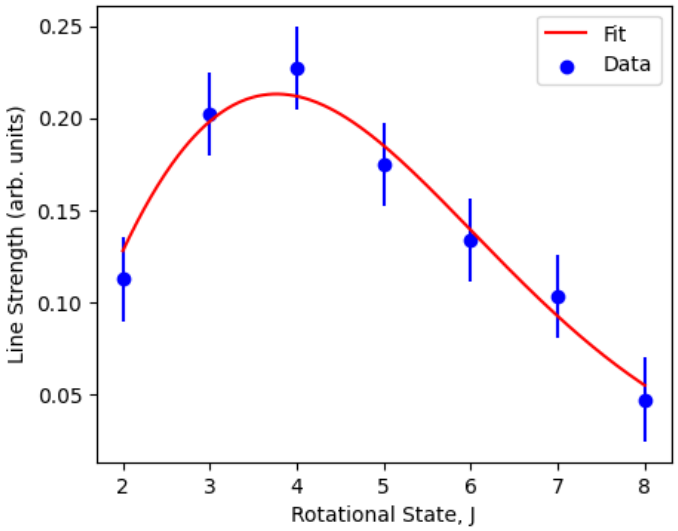

Figure 5.2: The P-transition line strengths of $Al^{35}Cl$ in the $v = 0$ vibrational branch as a function of the $X^1\Sigma^+$ state quantum number J. The absorption signal is integrated between 0.7ms - 3.1ms after the ablation. A rotational temperature of 8.3(4)K is extracted from a least-square fitting by considering both Boltzmann distribution and the rotational transition strengths[69].

Where $\Lambda = 0$ for the $X^1\Sigma^+$ state, thus S_J is reduced to $S_J = (J-1)/2$. Finally, a least-square fitting method is used to fit the line strengths with the intensities of the lines,

$$I_J \propto \frac{2J+1}{(J-1)/2} e^{-E_J/(k_B T)} \tag{5.4}$$

to yield an estimated rotational temperature of 8.3(4)K. This is a few K higher than the cell base temperature, which besides the heat load, is also attributed to the fact that the temperature is extracted from absorption signals integrated from 0.7ms to 3.1ms after the ablation and thermalization has not been achived. To further check the rotational temperature of the AlCl beam after a longer thermalization time to reach thermal equilibrium which is expected out of the cell , the same absorption measurements can be made out of the cell, a suggested measurement for future work.

5.2.3 Molecular Constants

With the signal-to-noise ratio we could reach in our experimental setup, we were able to obtain spectra for the $A^1\Pi(v'=0) \leftarrow X^1\Sigma^+(v=0)$ and $A^1\Pi(v'=1) \leftarrow X^1\Sigma^+(v=1)$ bands of transitions. While this gives us a decent amount of data to fit the Dunham coefficients up to Y_{11} for $Al^{35}Cl$, it limited us to fit the Y_{11} coefficient for $Al^{37}Cl$. The Dunham fit is then compared with the line centers from Voigt fitting of the experimental data. The spectra and Dunham fitting are shown in fig5.3

Two approaches were taken for the fitting of the Dunham coefficients, one being that fitting the two different isotopes separately, and the other is fitting the two isotopes simultaneously with the mass-reduced Dunham coefficient discussed in Chapter 2. For all the fittings, the $A^1\Pi$ state Dunham coefficients are varies and the $X^1\Sigma^+$ state Dunham coefficients are obtained from previous measurements[94]. The number of coefficients are restricted to a minimum to avoid shifts from systematic offsets of the data and subsequently the fitted line centers. The fitted Dunham coefficients for fitting the two isotopes separately are shown in table5.1, with the average difference between the fitted values and the measured values. On the other hand, as discussed in chapter 2, the Dunham coefficients are proportional to the reduced mass μ of the molecule given by,

$$Y_{jk} \propto \mu^{-(j+2k)/2} \tag{5.5}$$

Thus we can define a new set of mass independent Dunham coefficients as,

$$U_{jk} = \mu^{(j+2k)/2} Y_{jk} \tag{5.6}$$

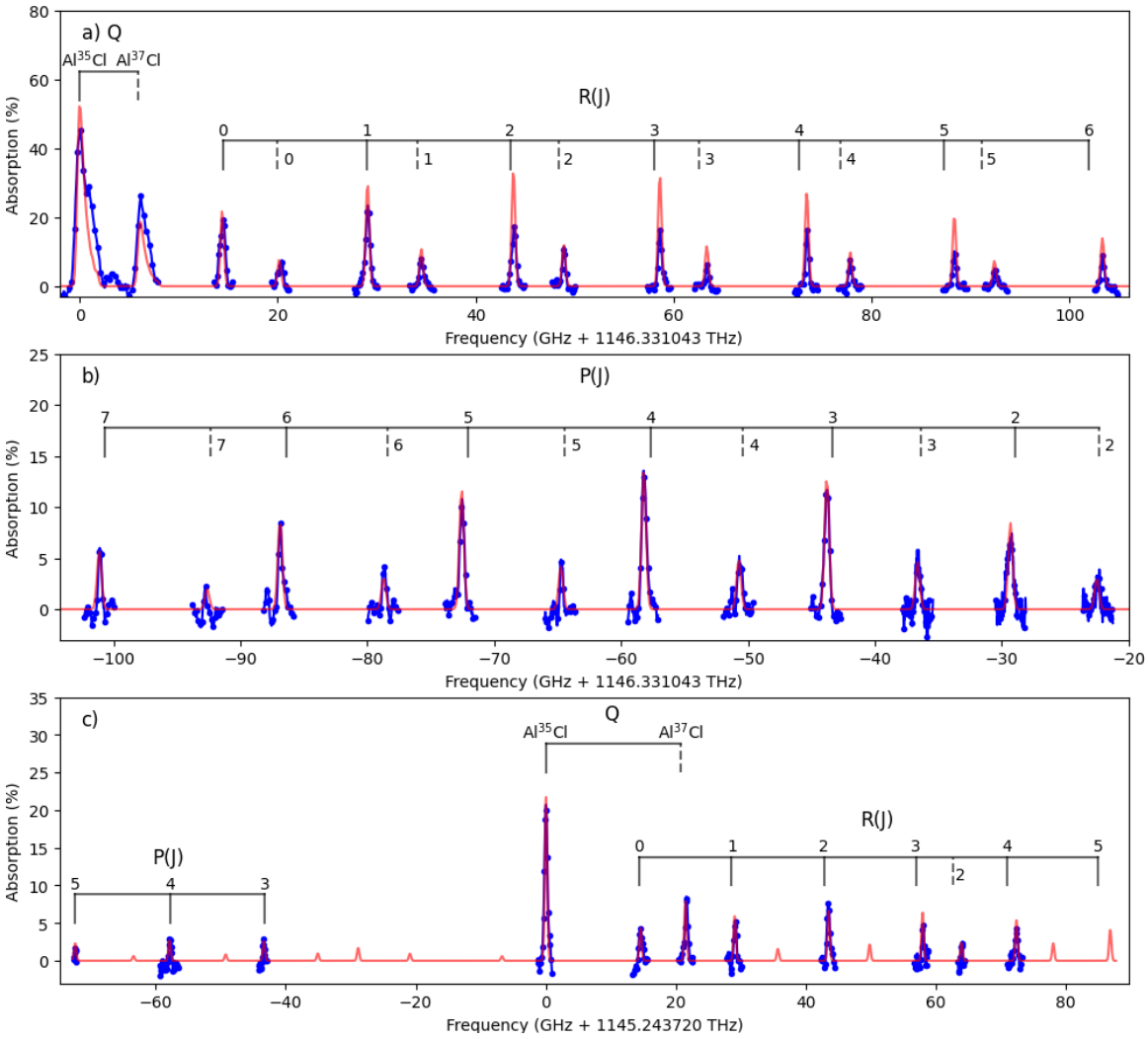

Figure 5.3: (a) Q , R , (b) P absorption spectrum of the $A^1\Pi(v' = 0) \leftarrow X^1\Sigma^+(v = 0)$ transition and (c) Q, R, and P branch of the $A^1\Pi(v' = 1) \leftarrow X^1\Sigma^+(v = 1)$ transition. Experimental data are depicted with blue dots and the fit to mass-reduced Dunham model are the red lines. Black lines are predicted frequencies from the *ab-initio* theory for $Al^{35}Cl$ (solid) and $Al^{37}Cl$ (dashed) with the rotational quantum number J of the $X^1\Sigma^+$ state[69].

Which allows one to define Dunham energy levels that include all isotopes. The fitting approach with such model has the advantage of reducing restrictions on the isotope dependence of the rotational and vibrational constants. The results are shown in the second column of table5.2. The fitting resulted in a higher mean line error. This is attributed to

	$Al^{35}Cl$	$Al^{37}Cl$
Y_{00}	38257.4210(4)	38257.3401(7)
Y_{10}	441.3320(6)	436.2127(6)
Y_{01}	0.24534(2)	0.23833(2)
Y_{11}	-0.00265(3)	
Mean Line Error	26 MHz	41 MHz

Table 5.1: Dunham coefficients in units of cm^{-1} for the $X^1\Pi$ state from a least-square fitting of the measured line centers[69].

not considering the isotope dependent Born-Oppenheimer breakdown factors[116, 117],

$$Y_{kl} = \mu^{-(k+2l)/2}\left(1 + \frac{m_e}{m_{\mathrm{Cl}}}\Delta_{kl}^{\mathrm{Cl}}\right)U_{kl} \tag{5.7}$$

By introducing one breakdown coefficient $\Delta_{00}^{\mathrm{Cl}}$, we find better agreement of the fitting with the data and the mean line error is reduced by a factor of two, shown in the third column of table5.2 with the U_{kl} coefficients. We used only one breakdown coefficient since there are no other Born-Oppenheimer breakdown coefficients we can find in literature for the $X^1\Sigma$ state [94] and none is found for the $A^1\Pi$ state.

5.2.4 Frank-Condon Factors

Once we obtained the molecular constants of the $A^1\Pi$ state, we can estimate the Franck-Condon factors of the $A^1\Pi \leftarrow X^1\Sigma^+$ transition by approximating the potential energy surfaces as a harmonic oscillator, which is a good approximation at the temperatures of our measurements at a few K. The Franck-Condon factors, as discussed in chapter 2, is

U_{00}	38253.33(2)	38253.31(2)
U_{10}	1764.9(2)	1766.1(2)
U_{20}	-83.0(4)	-85.4(4)
U_{01}	3.7377(3)	3.7367(3)
U_{11}	-0.165(2)	-0.157(2)
$\Delta_{00}^{\mathrm{Cl}}$		-0.158(7)
Mean Line Error	72 MHz	31 MHz

Table 5.2: Mass-reduced Dunham coefficients in units of cm^{-1} for the $A^1\Pi$ state obtained from the measured line centers. The third column are the Dunham coefficients with adding one Born-Oppenheimer breakdown coefficient ($\Delta_{00}^{\mathrm{Cl}}$)[69].

given by

$$q_{v',v} = |\langle \psi_{v'} | \psi_v \rangle|^2 \tag{5.8}$$

Where $\psi_{v'}$ and ψ_v are the harmonic wavefunctions of the vibrational eigenstates of the upper and lower levels. The harmonic wave functions depend on the equilibrium molecular bond length R_e and the vibrational constant ω_v. The equilibrium bond length can be estimated with the rotational constant B_v by approximating the rotational energies as a solution of the rigid rotor potential.

$$B_v = \frac{\hbar}{4\pi\mu R_e^2} \tag{5.9}$$

Where B_v is given by

$$B_v \approx Y_{01} + Y_{11}(v + 1/2) \tag{5.10}$$

and

$$\omega_v \approx Y_{10} + Y_{20}(v + 1/2) \tag{5.11}$$

With the molecular constants we measured, the equilibrium bond length for both isotopes in the $A^1\Pi$ state is estimated to be $R_e \approx 2.1220$ $\mathring{A}$. Plugging the numbers for R_e and ω_v, we estimated Franck-Condon factors presented in table5.3 with a comparison of the values obtained from *ab initio* calculations and found good agreement. With an estimated Franck-Condon factor of the $A^1\Pi(v' = 0) \leftarrow X^1\Sigma^+(v = 0)$ transition to be 99.88% from both the experimental and theoretical results, it renders that AlCl is indeed an excellent candidate for laser cooling.

	$Al^{35}Cl$		$Al^{37}Cl$
$\nu' \rightarrow \nu$	Expt.	Theo.	Expt.
$0 \rightarrow 0$	0.9988	0.9988	0.9989
$0 \rightarrow 1$	0.0012	0.0003	0.0011
$1 \rightarrow 0$	0.0019	0.0003	0.0019
$1 \rightarrow 1$	0.9961	0.9965	0.9961

Table 5.3: Estimation of Franck-Condon factors for the $A^1\Pi \leftarrow X^1\Sigma^+$ transition by using harmonic oscillator wavefunctions with the experimentally determind B_v and ω_v compared with the values obtained from *ab initio* theory.

5.3 Helium-YAG Dependence of the AlCl Yield and the Missing P_{11} Line

As a final remark, mention should be made that in our measured spectrum, we could not observe the P(2) transition in the $A^1\Pi(v' = 1) \leftarrow X^1\Sigma^+(v = 1)$ band. Meanwhile,

the intensities of the R transitions are in general about twice of that of the P transitions. We do not have good explanations to this but speculate that it could be due to the preparation of AlCl with ablation. The ablation process could excite some portions of the molecules to the $A^1\Pi$ state, either directly or being decays from higher excited states. In such situations, the competing absorption and emission processes would dramatically decrease the signal. In order to test our speculation, we did a systematic measurements on the YAG-power dependence of the absorption strength at different helium flow rates as shown in fig5.4, but did not observe significant difference between different ablation powers. To further measure the P_{11} branch transitions, in beam fluorescence measurements can be made to minimize Dopper broadening effects, given that we have a working AlCl beam now.

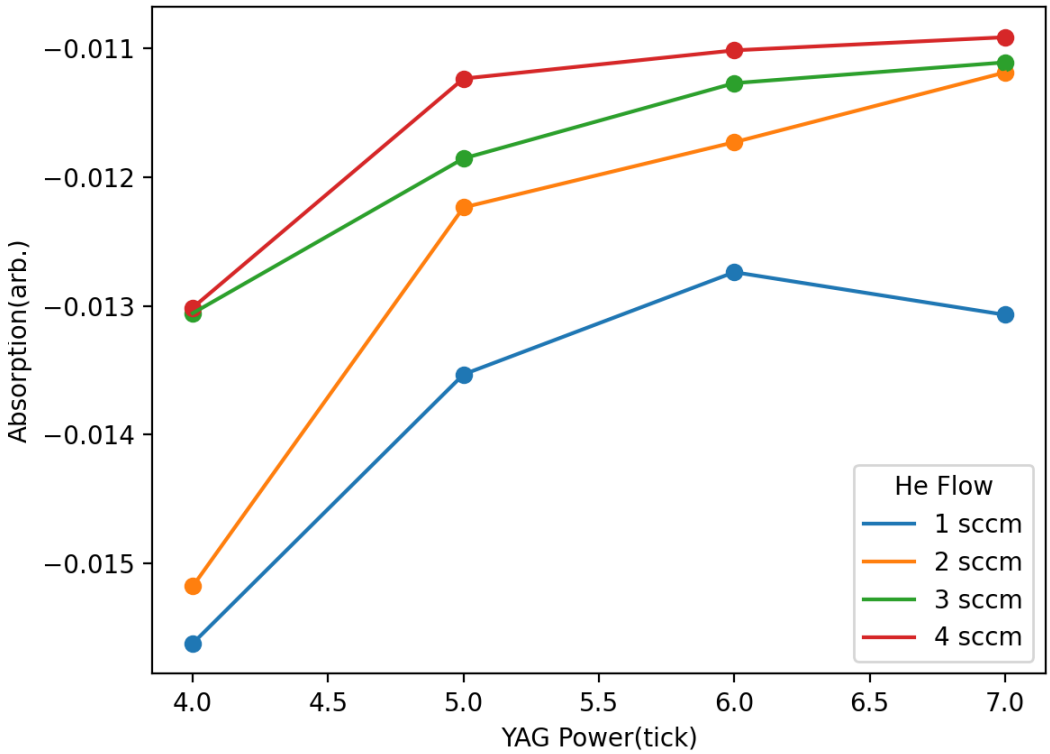

Figure 5.4: YAG ablation power dependence of the absorption strength. The measurements were carried out to test our speculation that ablation could populate the $A^1\Pi$ state that resulted in weak P_{11} transitions, especially the missing P(2) transition

Chapter 6

Optimization of Pulsed Laser Ablation Production of AlCl

The first step towards laser coolig of AlCl is to generate it in the gas phase and make a slow, cold and bright beam of it with a density as high as possible, which is especilly critical for applications such as creating molecular Bose-Einstein condensates(BECs) or quanum simulation of condensed matter systems. However, no previous studies on AlCl were based on our method of laser ablation along with cryogenic buffer gas cooling. In this chapter, we present our pathways on finding a robust way of creating AlCl in the gas phase and our studies on optimizing the initial production of it for laser cooling experiments.

6.1 Motivation and Background

As discussed in the section on molecular beams in chapter 3, to carry out laser cooling experiments on AlCl, we need to produce a cryogenic buffer gas beam source with the

molecules being generated by laser ablation, however, previous studies on the spectroscopy of AlCl were all based on either heating $AlCl_3$ or putting it in a discharge[75, 78, 77, 118, 119, 120, 121]. Experiments have also been carried out to react aluminum vapor with gases such as Cl_2 and HCl, as well as vaporized solids such as $MgCl_2$, $AlCl_3$ and AgCl[122, 123, 124, 125, 126]. These thermal effusive sources are hot both translationally and internally, making it not suitable for laser cooling. Similar approach could be introduced to the cryogenic chamber with laser ablation of Al and reaction with Cl gases to form AlCl. Laser ablation of Al should be efficient as Al absorbs visible light well. Such gases are also chemically stable. So such approach could give rise to high production of gas phase AlCl. However, these gas Cl sources are corrosive and potentially toxic, so the introduction of these gases into the cryogenic chamber and the ultra-high vacuum chambers could add experimental problems and even cause harms to the experimenters. Further investigations have to be made before implementing such approaches. Thus, as a first step to generate AlCl in the gas phase, our only choice is left with laser ablate solid targets that contains Al and Cl atoms. The straightforward choice for such a target would be $AlCl_3$ and it is indeed what we used to find our first AlCl signal and carried out earlier spectroscopy experiments. Ablating $AlCl_3$ in fact gives us the highest production of AlCl as will be shown later, however, it comes with the problem of being highly hydroscopic, causing it not only decomposes to HCl gas which is toxic, but also gives highly variable signals from shot to shot. This led us to think of other choices. Most salts are compounds of alkaline or alkaline-earth metal atoms and Cl atom, and are not toxic, thus become the next choice for us. We first tested a target made of Al and potassium chloride(KCl) and found successful production of AlCl. We also

found the target to be stable, not highly hydroscopic and thus become our choice. In order to generate robust, high density of cold beams of AlCl. We carried out a systematic study on the composition of the target, with varying molar ratios of Al to Cl and varying element of the salts, denoted as XCl_n. In the following sections, we first present the procedure of how the solid targets are made and then present the experiments results of the target study and gives a discussion that can potentially give guidance to further investigations on laser ablation of solid targets for laser cooling.

6.2 Target Making Procedure

All of our targets are made by first mixing aluminum powder with the various chloride sources by mortar and pestle and then put inside a 12mm diameter pellet die and pressed between two anvils with a hydraulic press as shown in fig6.1 at 6000psi for 1 minute[1]. The chloride sources need to be first grind to finer size as fine as possible and it is critical to take enough time to mix the aluminum powder with the clorides as even as possible. The aluminum powder is 99.95% purity with grain size $< 75\mu$m from Sigma Aldrich. For the studies of varing Al to Cl ratio, we chose potassium chloride(KCl) that is 99% purity BioXtra KCl from Sigma Aldrich. For the studies on other chloride sources, all were carried out with a Al:Cl molar ratio of 1:4 and the sources are crystalline sodium chloride (NaCl, Fisher Scientific), 98% anhydrous magnesium chloride ($MgCl_2$, Sigma Aldrich), and anhydrous calcium chloride ($CaCl_2$, Fisher Scientific). For comparision with $AlCl_3$, pure 98% sublimed, anhydrous aluminum trichloride (Sigma Aldrich) was used. For the Al and XCl_n mixtures,

[1]However, later we found that pressing for 10 minutes increase the soild density of the pellets and improve the yield, thus become the standard now.

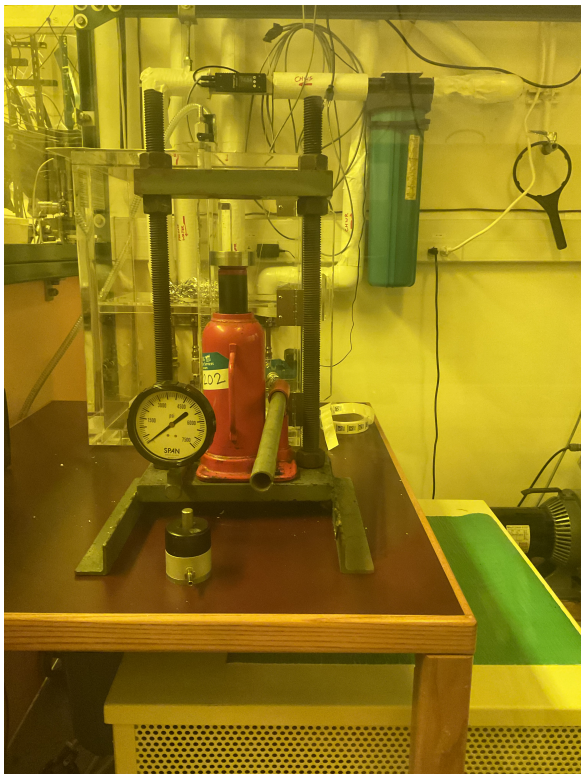

Figure 6.1: Hydraulic press and pellet dies used to make solid pellets of target. Typical pressure used is 6000psi and pressing time used to be 1 minute. However, we found pressing for 10 minutes increase the solid density of pellets and increase ablation yield.

the sample is cured for 24 hours in air after pressing, while the $AlCl_3$ samples are wrapped in parafilm and cured for 4-5 hours. The solid pellets are glued to a copper101 target holder by a thin layer of Stycast 2850FT. After full curing of the epoxy. The target holder is attached to the main cell in the cryogenic chamber.

6.3 Experimental Results

The apparatus for the experiment is similar to the spectroscopy experiments described in chapter 5, other than that the fundamental IR and the second harmonic blue light are used to measure the absorption of K and Al respective at $\approx$ 766nm and $\approx$ 395nm.

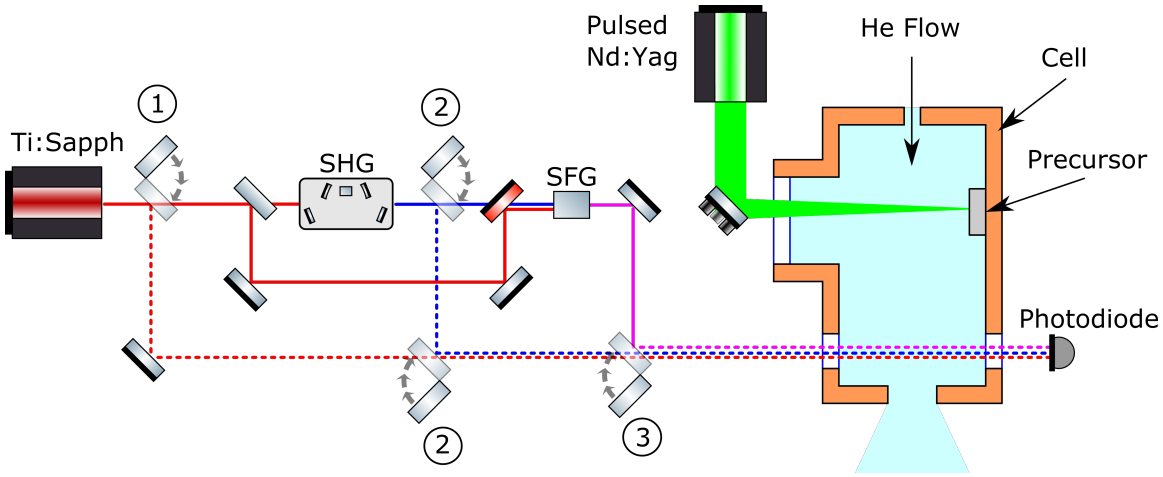

Figure 6.2: Schematic of the experimental apparatus for the target studies. The flip mirrors (1,2 and 3) allow for frequency selection. (1) uses the fundamental Ti:Sapph IR at 766nm for measuring K. (2) uses the SHG blue light at 395nm to measure Al and (3) uses the THG UV output at 261.5nm to measure AlCl[70].

For that, we added flip mirrors as depicted in fig6.2. A typical time trace of absorption is shown in fig5.1 of chapter 5. The yield of AlCl, Al and K are all observed by absorption spectroscopy. In order to account for the inhomogeneity of the target, we typically raster over the target and take minimally 50 spots on the target with at least 10 averages on each spot. The yields can be conveniently visualized with target mappings as shown in fig6.3 with the associated targets. Shown in fig6.4 is a comparison of the targets before and after the ablation. As can be seen clearly in the picture, besides the corrugated surface that due to losses of the target, shiny coverings of Al are also present, which we attribute to the recondensation of Al atoms back to the target surface due to cold buffer gas beam environment and this turns out to be a critical factor to understand the yield of AlCl with our models.

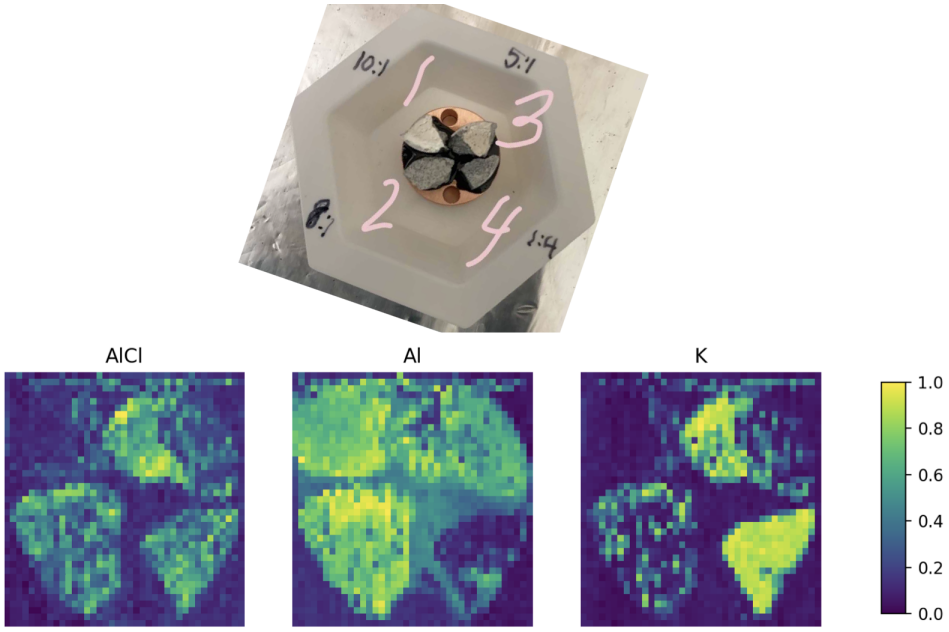

Figure 6.3: Sample mapping of the yield of AlCl, Al and K, with the corresponding Al:Cl molar ratios indicated in the picture of targets. The scale on the mapping is absorption strength.

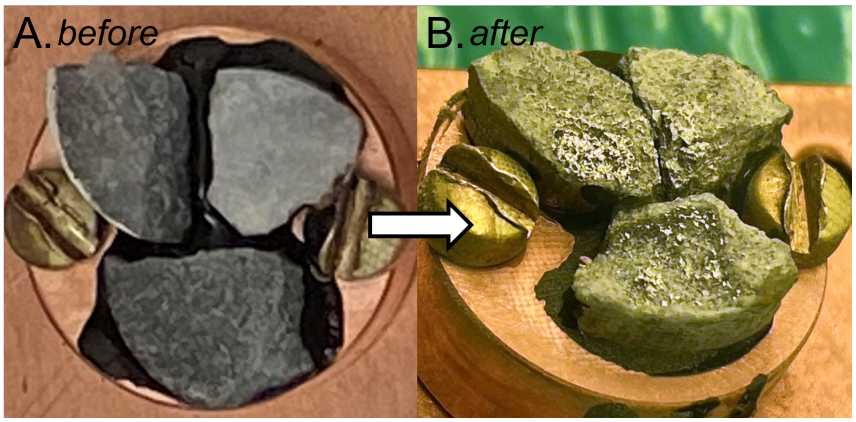

Figure 6.4: A) Sample targets of Al:KCl mixtures before ablation. Targets vary in shade of grey due to the amount of aluminum, shown above are pure KCl (top right), 1:3 (top left), and 1:10 (bottom). B) Typical target appearances after ablation showing shiny aluminum coating on the surface after ablation. The Al:KCl ratios are 3:1 (top right), 1:1 (top left), and 1:3 (bottom).

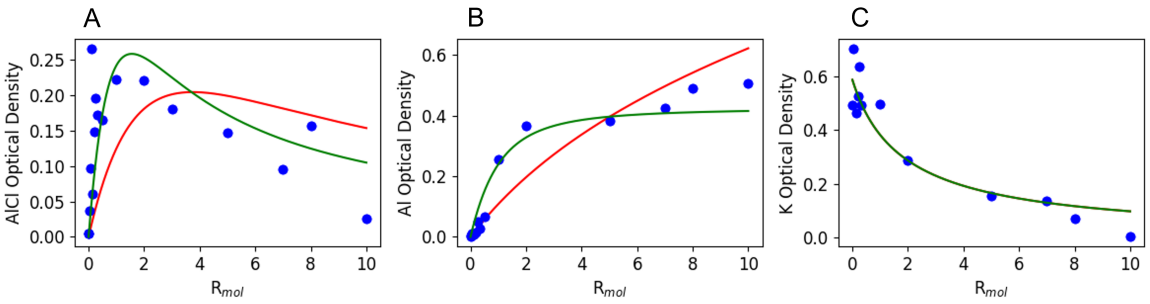

Figure 6.5: Model A (red line) and Model A' (green line) are overlaid with experimental data of optical densities of (A) AlCl (B) Al, and (C) K showing a better fit from Model A'. Model A and A' predict the same fit for K Optical Density. The details of Model A and A' are discussed in appendix B.

The experimental results of the Al:Cl molar ratio study is shown in fig6.5 along with fittings from two chemical models that is discussed in appendix B. In essence, both models describe AlCl formation based on first encounter collisions with a limitation of the ablation volume v_0, but model A' takes into account the recondensation of Al back to the target surface such that there is a saturation limit of gas phase Al that limit the production of AlCl. The saturation of Al in the gas phase is indeed what we observe with the data as can be seen in plot(2) of fig6.5. The important result in regards of laser cooling of AlCl is that with the better fit of model A', a molar ratio Al : Cl of 1 : 1.55 gives the optimal production of AlCl regardless of the chloride sources.

To further understand laser ablation production of AlCl with mixtures of aluminum powders with chloride compounds, we also investigated production of AlCl with different kinds of chloride sources. A comparison of the yield is shown in fig6.6. The results show that the production of AlCl with different kinds of chloride is within a factor of 2, indicating that the production of AlCl with such mixtures is not determined by the properties of XCl_n such as the X-Cl bonding energy. Instead, from the understanding with the chemical models, we

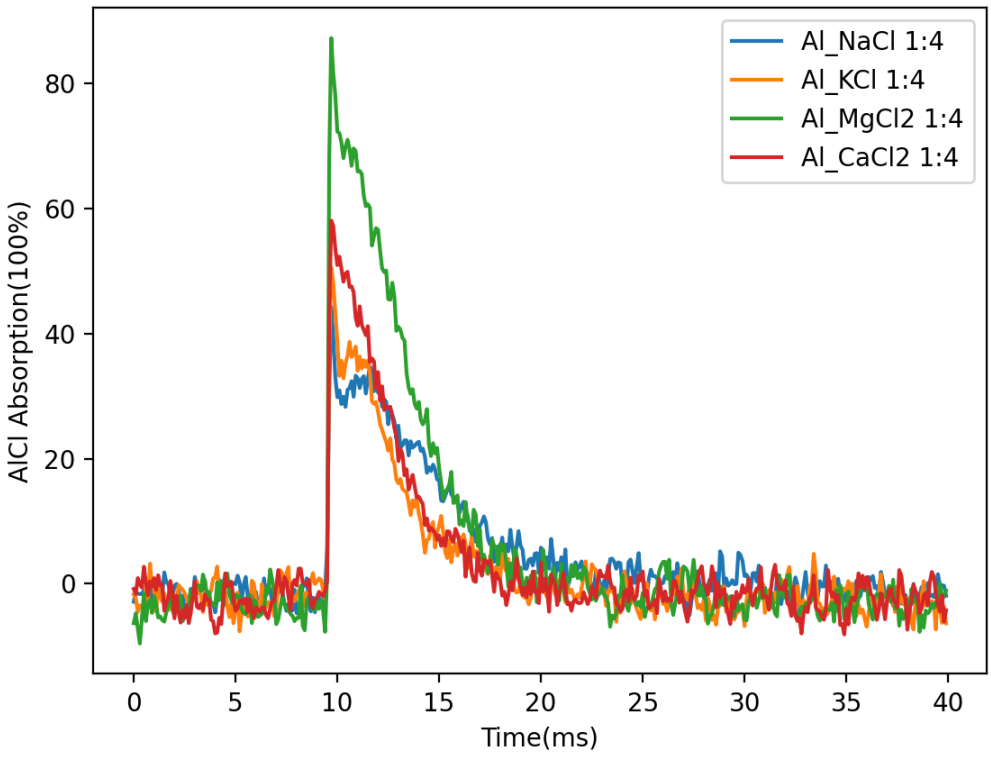

Figure 6.6: Absorption strength of AlCl from different chloride compounds with Al:Cl ratio of 1:4 for all the compounds showing yield of AlCl within a factor of 2.

find that the Cl solid density is what determines the yield. Given that the yield of AlCl is independent of the chemical properties of the chloride compounds, our conclusion can also be potentially applied to other metal-halide productions such as AlF.

Alongside the target studies, we also estimated the yield number density of AlCl molecules in cell based on Beer's law,

$$I(\omega, z) = I(\omega, 0)e^{-n\sigma(\omega)z} \tag{6.1}$$

where I(ω, 0) and I(ω, z) are the intensities before entering and after exitting the cell. σ is

the absorption cross section that is $\approx \lambda^2/2$. z is the interaction length which is the width of our cell. n is the number density of AlCl that is the parameter we can calculate from our absorption measurements. The estimated number densities of AlCl is shown in table6.1.

Al:Cl Molar Ratio	AlCl Density(10^8 per cm^3)
0.02	1.977
0.05	5.108
0.10	14.079
0.125	3.169
0.20	7.854
0.25	10.350
0.33	9.140
0.50	8.736
1.00	11.793
2.00	11.664
3.00	9.534
5.00	7.764
7.00	5.019
8.00	8.264
10.00	1.334

Table 6.1: Estimation of number density of AlCl in cell based on Beer's law with different Al:Cl molar ratios. With optimal production, we get density at the order of 10^9 molecules per cm^3.

Chapter 7

Hyperfine Structure of the $A^1\Pi$ State Relevant to Laser Cooling

Understanding the hyperfine structure of both the $A^1\Pi$ state and the $X^1\Sigma^+$ state and measuring the hyperfine constants are crucial to understand and determine the optical cycling scheme. The $X^1\Sigma^+$ hyperfine structure has been previously studied[95] and a hyperfine span of ≈11MHz was reported, which is well within the natural transition linewidth of $A^1\Pi \leftrightarrow X^1\Sigma^+$ of ≈ 30MHz. Thus, measuring the hyperfine structure of the $A^1\Pi$ is critical to determine how much fraction of the hyperfine transitions a single laser frequency can address which would determine the ability to optical cycle AlCl and create damping force on it. In addition to the hyperfine structure, Zeeman interaction are often used in laser slowing and magneto-optical traps to enhance damping forces or being engineered to address dark states. In order to understand the hyperfine structure and Zeeman splittings relevant to laser cooling, we spectroscopically measured the hyperfine structure of the lowest

three rotational lines of the $A^1\Pi$ state. In this chapter, we present our in beam fluorescence spectroscopy measurements and the results, discuss its implications to laser cooling and estimate capture velocities of an AlCl MOT.

7.1 Experimental Setup

The experimental setup is described in detail in Chapter 3. In a nutshell, the AlCl molecules are produced in a cryogenic buffer gas beam cell with a base temperature of 3.4K by laser ablation of a solid target made of mixtures of Al and KCl powders with the laser being an Nd:YAG pulsed laser with a pulse duration $\approx$ 5ns and pulse energy of $\approx$ 10mJ. The AlCl molecules then thermalize with the cold helium buffer gas beam and diffuse out of the cell with a beam in the hydrodynamic regime. The fluorescence measurements were taken in the intermediate stem chamber (see fig3.7) at $\approx$ 40 cm downstream from the ablation region where the molecular beam and the probe laser beam are aligned orthogonal to each other and the induced fluorescence photons were collected with a photo-multiplier tube (H10722-04, Hamamatsu). The probe UV laser light at 261.5 nm with power of a few mW was produced by frequency-doubling the output of a 522 nm green VECSEL laser(Vexlum VALO Vecsel) with a custom-built second-harmonic generation cavity as discussed in chapter 4. The laser frequency was tuned and frequency stabilized by using the frequency readout of a wavelength meter (WS-7, High-Finesse), which was calibrated by using saturated absorption spectroscopy of the Rubidium hyperfine transitions detailed in chapter 4.

7.2 Hyperfine Spectra

The hyperfine structure of the $X^1\Sigma^+$ state spans only about 11MHz by previous measurements[95], thus we attribute to any measured spectra to the hyperfine structure of the $A^1\Pi$ state. The R branch, depite not being the main cycling transition of Q(1), the change in quantum number J is suitable for fitting hyperfine constants. It also has advantages of scattering less photons relative to the Q branch to have enhanced signal to noise ratio and by rotational branching ratio, higher than P-branch. Beyond R branch, Q branch which is the interest of the main cycling transition is also measured up to Q(5). In collaboration with the McCarron group at University of Connecticut(UConn), we also compare our data with the UConn data and find good agreements.

7.2.1 R-Branch Spectra

The R branch spectra is shown in fig7.1. The red circles are data taken by us at UCR, and the blue diamonds are data taken at UConn. The black solid(non vertical) lines are fittings from our effective Hamiltonian model using fitted and *ab initio* calculated molecular constants. The vertical lines are hyperfine transitions predicted by our model with the heights indicating the transition strength.

Unlike a span of only 11MHz of the hyperfine structure in the $X^1\Sigma^+$ state. The span of the $A^1\Pi$ state hyperfine structure ranges from $\approx$ 500 MHz for $J' = 1$ to $\approx$ 200MHz for $J' = 4$. As can be seen from the fig7.1, as J′s increases, the span of the hyperfine structure decreases. The R(0) transition is partially resolved and the $J' = 1$ state should be similar to the f level, although we probed the e level of the $J' = 1$ state, thus this would

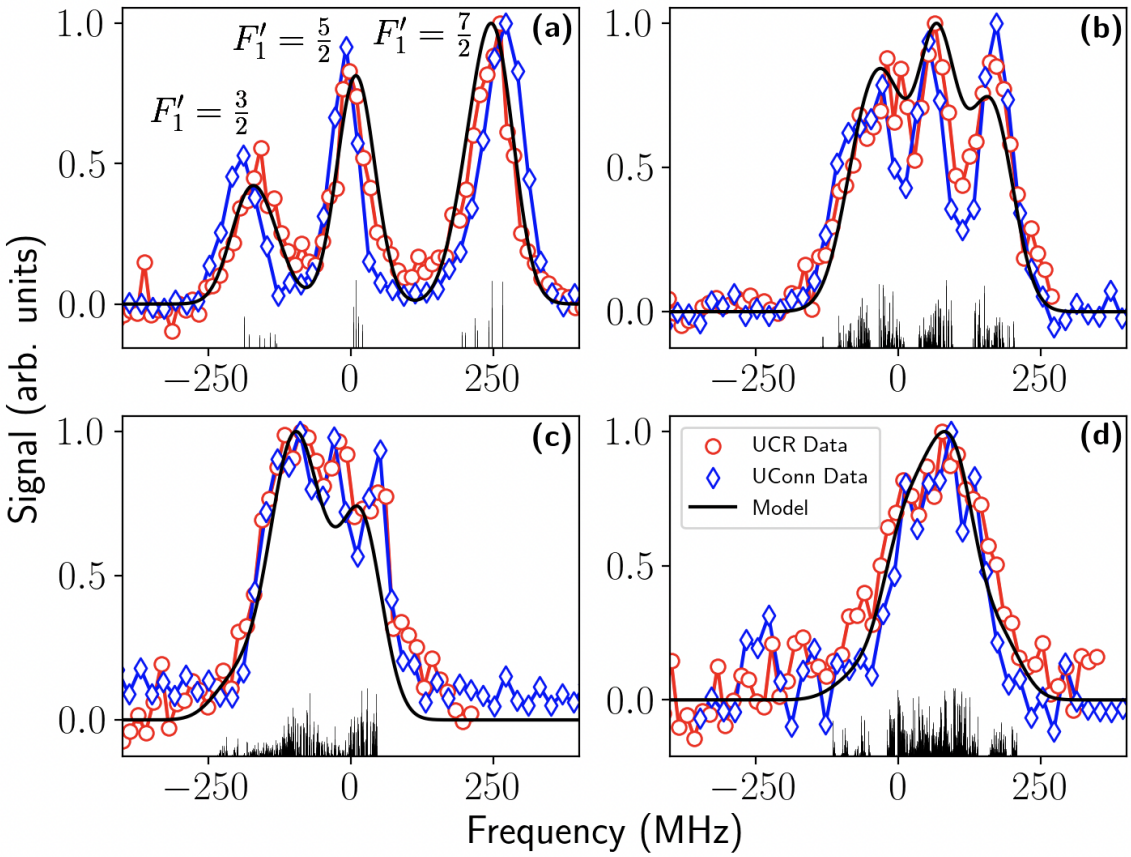

Figure 7.1: Normalized fluorescence data (red circles: UCR, blue diamonds: UConn) and model (black solid line) of the R(J) transitions, $X^1\Sigma^+, |v = 0, J\rangle \leftarrow A^1\Pi, |v' = 0, J + 1\rangle$, **(a)** R(0), **(b)** R(1), **(c)** R(2), and **(d)** R(3). The vertical black lines represent the different transitions predicted by our Hamiltonian model with their heights corresponding to their relative line strengths[97].

still give us a good picture of f level of the $J' = 1$ state which is the interest of the cycling transition. The partially resolved $J' = 1$ state indicates that addressing all the hyperfine levels would be suppressed with a single laser, however, the measurements were taken with a low power laser light much below the saturation intensity. With intensities going above the saturation intensity, we expect power broadening greatly enhance the hyperfine levels that can be addressed with a single laser.

From the measured spectra, we extrapolate the hyperfine structure constants by first determining the electron orbital-nuclear spin constants a_{al} and a_{cl} since they are the most dominant interaction. The constants and the associated uncertainties are shown in table7.1. In the mean time, we also used the R(2) and R(3) transitions to determine the Λ-doubling constant q, however, given the broad widths of the two transitions, we could only get an estimated bound values between -8MHz and -3MHz. This value gives us estimates of external electric field that can cause the mixing of the two Λ-doubling states so that the parity change associated with the mixing can make it to be a loss mechanism.

Constant	Value (MHz)
a_{Al}	$131.9\ \binom{+3.6}{-3.3}$
a_{Cl}	$42.0\ \binom{+8.1}{-7.0}$
q	$(-8, -3)$

Table 7.1: Hyerfine constants for the $A^1\Pi$ state including the electron orbital-nuclear spin interaction constants a_{al}, a_{cl} and the lower and upper bounds of the Λ-doubling constant[97].

We also estimated the electric quadrupole constants with the aid of *ab initio* calculations on the electric field gradients at each nucleus and the quadrupole moments of

147.7 mb for ^{27}Al nucleus[127] and 85 mb for the ^{35}Cl nucleus[128] found in literature. The quadrupole constants and electric field gradients are shown in table7.2 for the component along the inter-nuclear axis, which is the case for both the $X^1\Sigma^+$ state and the $A^1\Pi$ state and in table7.3 for the component perpendicular to the inter-nuclear axis, which is only the case for the $A^1\Pi$ state.

Nucleus	State	V_{zz} (a.u.)	eQq_0 (MHz)
Al	$X^1\Sigma^+$	-0.809	-28.1
	$A^1\Pi$	-0.220	-7.6
Cl	$X^1\Sigma^+$	-0.675	-13.5
	$A^1\Pi$	-2.554	-51.0

Table 7.2: *Ab initio* calculations of the electric field gradients and the quadrupole constants eQq_0 along the inter-nuclear axis[97].

Nucleus	$2\sqrt{6}(V_{xx} - V_{yy})$ (a.u.)	eQq_2 (MHz)
Al	0.605	102.9
Cl	0.332	32.5

Table 7.3: *Ab initio* calculations of the electric field gradients and the quadrupole constants eQq_2 perpendicular to the inter-nuclear axis for the $A^1\Pi$ state[97].

Where eQ are the nuclear quadrupole moments with electric field gradient at each nucleus, q_0 being equal to the V_{zz} component along the inter-nuclear axis and q_2 being equal to $2\sqrt{6}(V_{xx} - V_{yy})$ perpendicular to the inter-nuclear axis [57] and eQq_0, eQq_2 are the quadruple constants.

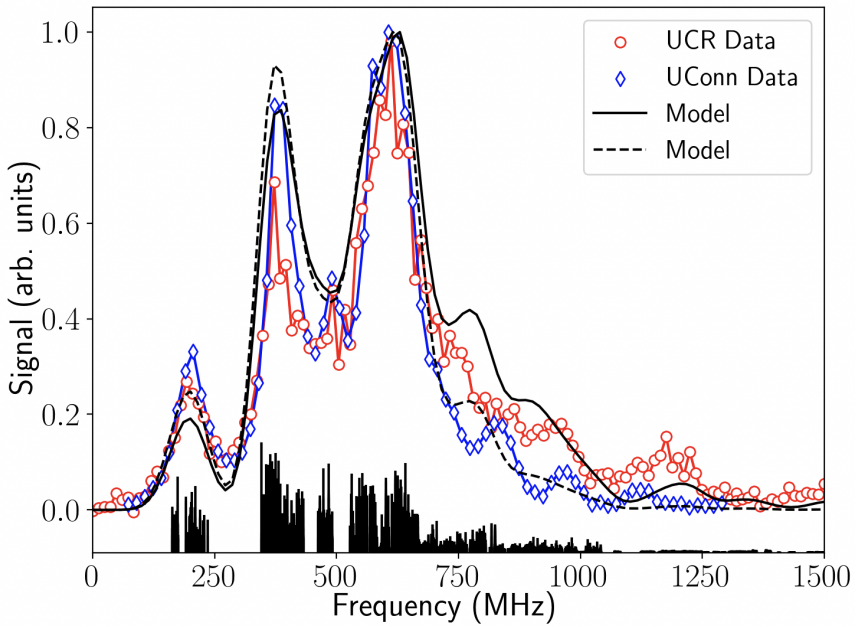

Figure 7.2: Normalized fluorescence data (red circles: UCR data, blue diamonds: UConn data) and model (black solid line) of the Q(1)-Q(5) transitions of AlCl.The models use the fitting parameters from fitting the R transitions and are only optimized to reproduce the measured signal amplitude, the rotational temperature ($T_{\mathrm{rot}} = 2.5\,\mathrm{K}$ solid line, $T_{\mathrm{rot}} = 1.6\,\mathrm{K}$ dashed line) and the absolute frequency offset. The vertical black lines represent the different transitions predicted by our Hamiltonian model with their heights corresponding to their relative line strengths[97].

7.2.2 Q-Branch Spectra

As our interest for the cycling transition lies in the Q transitions, specifically the Q(1) transition, after extrapolated and theoretically calculated the $A^1\Pi$ state hyperfine constants, we also did measurements on the Q transitions from Q(1) to Q(5) as shown in fig7.2. The model with fitted constants from the R transitions and theoretically calculated constants match the Q transition data well.

Chapter 8

Conclusions and Future Outlooks

8.1 Conclusions

In this thesis, I presented the essential works that need to be addressed before direct laser cooling and trapping of AlCl can be implemented. Before I joined the lab, the foundational setups of the experiment including the cryogenic buffer gas beam chamber and the Ti:Sapph laser systems with home-built SHG cavities and SFG single pass generation were already built-up. The first absorption signal of AlCl has also been observed. I participated in the absorption spectroscopy experiments we carried with the low temperature buffer gas beam cell soon after I joined the lab. I helped taking the spectroscopy data while started to learn about molecules and atomic physics. While I did not fit the full spectrum to extrapolate molecular constants, I started to learn least-square fitting techniques and fitted the rotational temperature from our in-cell spectroscopy data and tried to calculate the Franck-Condon factors based our data. At the time I also picked up the Ti:Sapph laser systems and constructed the laser diagram we used to describe our spectroscopy experiment.

Since no previous experimental research associated with AlCl was concerned with laser cooling and the cryogenic buffer gas cooling along with laser ablation production of molecules was only developed recently, we did not have knowledge about not only ways to generate high numbers of AlCl molecules but not even a robust way to generate it. The earlier targets of $AlCl_3$ gave us good signals, but its hydroscopic nature makes it difficult to deal with and gave us varying signals from day to day, even shot to shot. We also tried an organic compound aluminum phthalocyanine chloride, but unfortunately, it messed up our cell. All of this experience motivated us to have an investigation into all possible precursors to produce AlCl with the goal of finding a robust way of producing it at as high densities as possible. We were fortunate to have professor Barbeen in the chemistry department to collaborate with us and give us guidance on such matter as we do not have much knowledge in chemistry. We first tried out mixing Al powder with KCl and found signals of AlCl and found that mixtures of Al with KCl as a target is much more durable and easy to deal with. We then performed systematic investigation on such targets and studied the yield of AlCl molecules with varying Al:KCl molar ratios and Prof.Bardeen constructed simple chemistry models to help understand the nature behind the optimal molar ratio for Al:Cl, found to be 1:1.55. Further more, we wanted to see if this method applies with other alkaline or alkaline-earth metal and chloride compounds. We tried out NaCl, $CaCl_2$, $MgCl_2$ and found that, to our surprise, the yields differed only within a factor of 2, but this indicates that such methods are robust for producing AlCl, and might apply to other halides as well.

After extrapolating the molecular constants and confirmed the FCFs in comparison with theories as well, with the confidence of a Franck-Condon factor of 99.88% on the cycling

transition of $A^1\Pi \leftrightarrow X^1\Sigma^+$, and with a robust way of producing AlCl, We moved on to focus on the AlCl beams. However, for a while, we either could not observe a beam downstream or observe beams at $\approx$ 400m/s as if if were a room temperature beam. I machined new shield plates and an outer plate of the dewar in order to investigate absorption signal after the cell to see if we loose the molecules by a lot in cell which would tell us if if is a problem with the cell, but the spectroscopy results give us reasonable molecular densities our of the cell. Then it came a while when we were debugging for the problems with the beam. After adding sorb plates and more sorbs and improving pressure in the dewar, with the suggestions of adding Kapton foil between copper pieces in the cell, we for the first time, observed slow beams of AlCl. Later, we found that temperature is also key to producing high densities of molecules as well as slow beams. After adding more thermal links, especially a link directly from the 4K stage of the pulse tube to the cell, we finally now have robust AlCl beams that are relatively slow and bright.

With a working AlCl beam, we could carry out in beam fluorescence experiments that minimize Doppler shifts to resolve finer detailed states and energies. In order to understand and construct proper optical cycling schemes, one has to resolve the relevant hyperfine structure of the cycling states. By measuring the R transitions in beam, we could extrapolate some hyperfine constants and for the quadrupole constants, our collaborator helped us figure out by *ab initio* calculations. We compared our data with the McCarron group at UCoon and found good agreements and also theotically estimated the capture velocites.

8.2 Future Outlooks

At this point, given that we have confirmed the Franck-Condon factor of the $A^1\Pi \leftrightarrow X^1\Sigma^+$ cycling transition to be 99.88% and have a robust way of producing AlCl moleucles and have a slow and bright AlCl beam, with also a knowledge on the relevant hyperfine structures of both $A^1\Pi$ and $X^1\Sigma^+$ states, we are ready towards laser cooling and trapping of AlCl, but of course, we need to have more things done and improved. First of all, we need enough laser power. With the estimated capture velocities, we estimate to need 0.5W per beam of the MOT. For such high power UV, we are currently constructing a similar system as the UConn group with frequency quadrupling an IR laser coming out of a fiber amplifier. We anticipate to get $\approx$ 2W of UV eventually. Once we get the UV power, we are ready to try optical cycling and towards laser cooling and MOT trapping.

On the other hand, there are still things we can implement to improve in a variety of areas in our experiments. First of all, we by far, always have had much less laser power coming out of our second harmonic cavities. As my knowledge goes now, SHG process is indeed sensitive to temperature as it can influence phase matching angle, thus adding temperature controllers to the non-linear crystal can help stabilize its optical properties, especially when the temperature operates at relatively high values, it would also help keep out of water which is another mechanism that can change the optical properties of the crystal or even damage it.

We gradually realized how important the base temperature of the cell is to the production of the molecules and to make a slow, bright beam. We already added more thermal links between the pulse tube stages and a direct connection between the cell and

the 4K stage. On the other hand, in order to minimize black-body radiation, we also later modified the shield to have minimized opening areas, that however, will interrupts gas flows between layers and causing a high pressure between shields and even in-cell to destroy, especially a two-stage beam. For that, Chevron baffle assembly can be added to maximize gas conductance between shields. This is discussed in the thesis[129] and future work can refer to the thesis.

While we studied a variety of solid targets for producing AlCl, another foreable way to produce even higher densities of AlCl is by laser ablating Al while flowing into the cell a type of chloride gas. However, for Cl, such as gas is not trivial to find as most of the common one such has HCl or Cl_2 are either corrosive or toxic, but we can still keep looking into this and see if we or some other scientists can help us find such a Cl gas.

Finally, over the last year, especially while our Vexlum laser is broken and under repair, we tried to look for other molecules that have transitions within the reach of our lasers, among the list are MgCl, MgF, HoF and I_2, but found no success, while the transitions have all been previously observed. We could further debug into this issue and if in future, we can see signals of such molecules, we not only know our whole system must have more improvements, but also can try laser cooling and trapping of new species.

My PhD was certainly during a unique period of time with a global pandemic never seen before. I joined the lab at the beginning of this pandemic and spent most of the time through it. I am so grateful for all the support I gained from my PI and how much I learned from him. I always remember that first copper shield I machined went wrong and how my PI had me learned how to do experimental research properly though in a hard

way. I started AMO research with an interest in simulating condensed matter systems, but the hardship with molecules never got me an optical lattice, however, it made me realize the beauty of AMO experiment, precision. I gradually developed a strong appreciation on how much it is behind just to measure something more precisely and how that can lead to discoveries. I will carry on what I learned during my PhD from the project and everyone I worked with and continue learning along life.

Appendix A

Updated Drawings in the Dewar

In order to have more sorbs in the dewar and have the sorb plates modular, I modified the designs of the shields and designed the sorb plates to be machined. Since our AlCl beam did not work, we needed to do absorption spectroscopy in front of cell, which also lead to some modifications of designs in the dewar. Attached are all the drawings for reference.

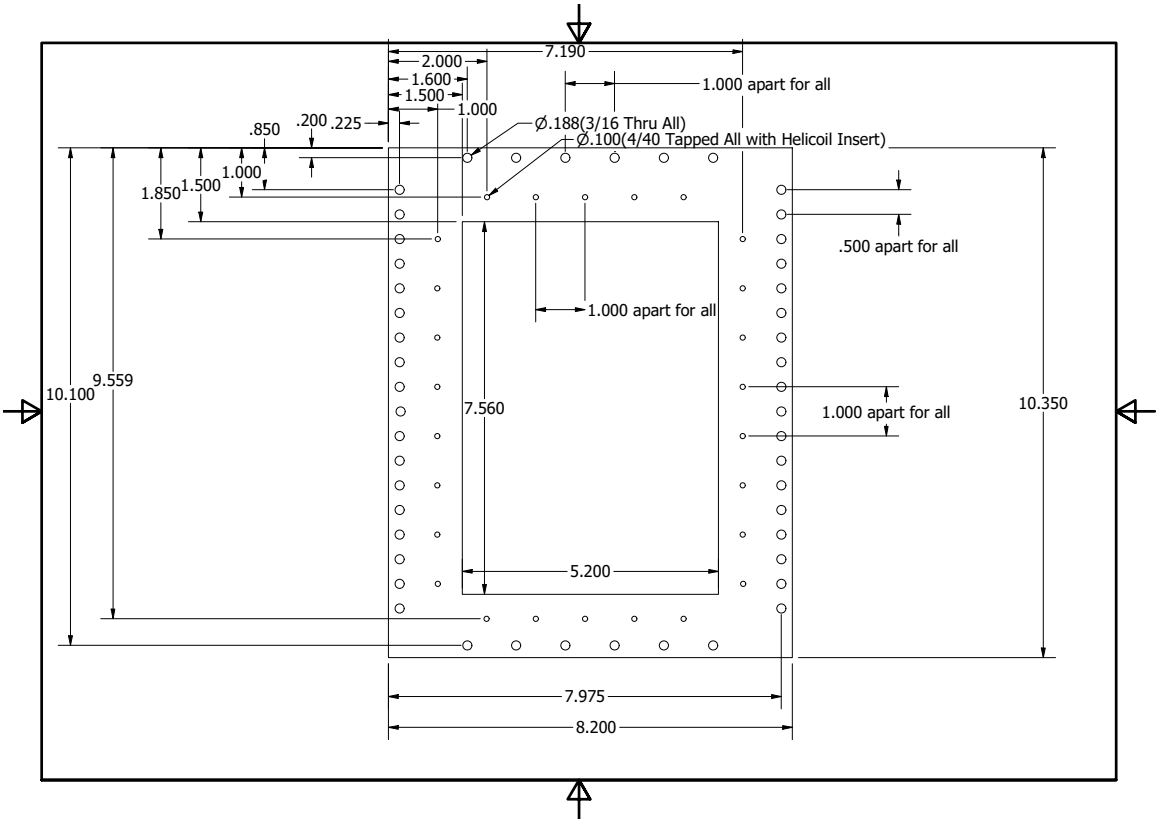

Figure A.1: 4K Frame Spec Side

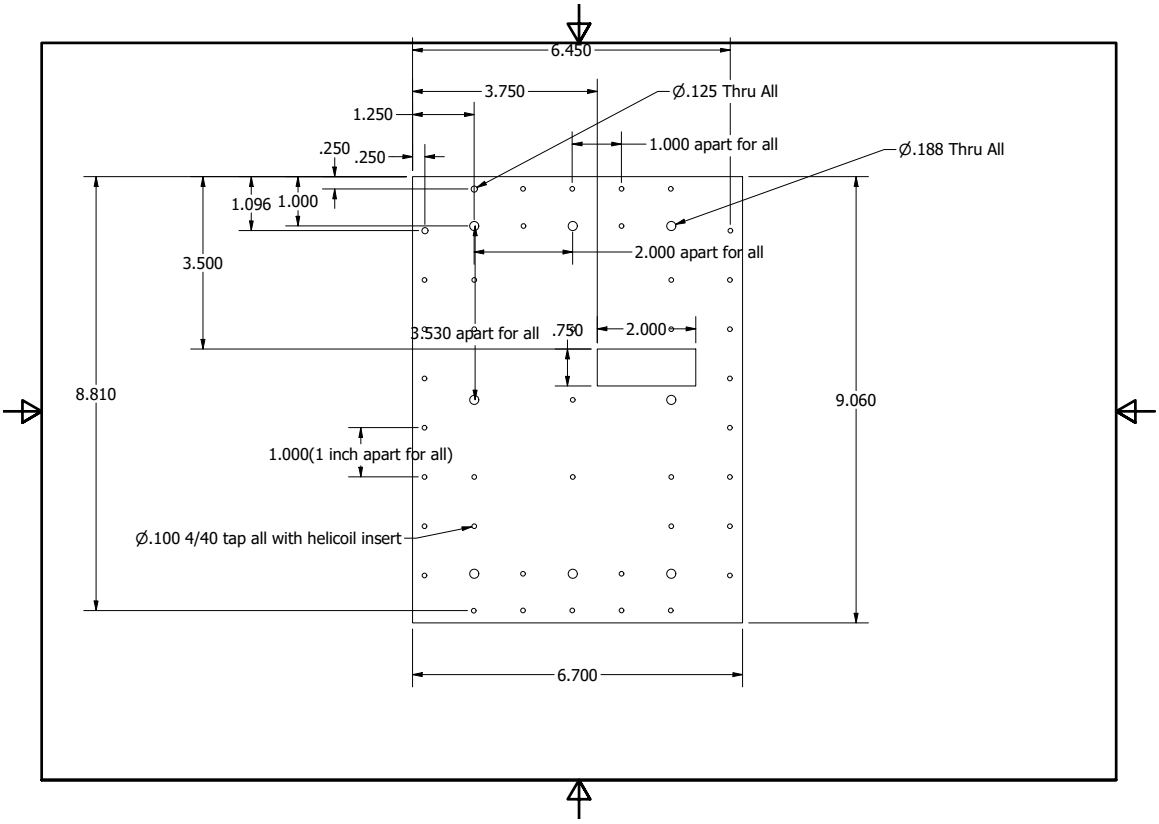

Figure A.2: 4K Inset Spec Side

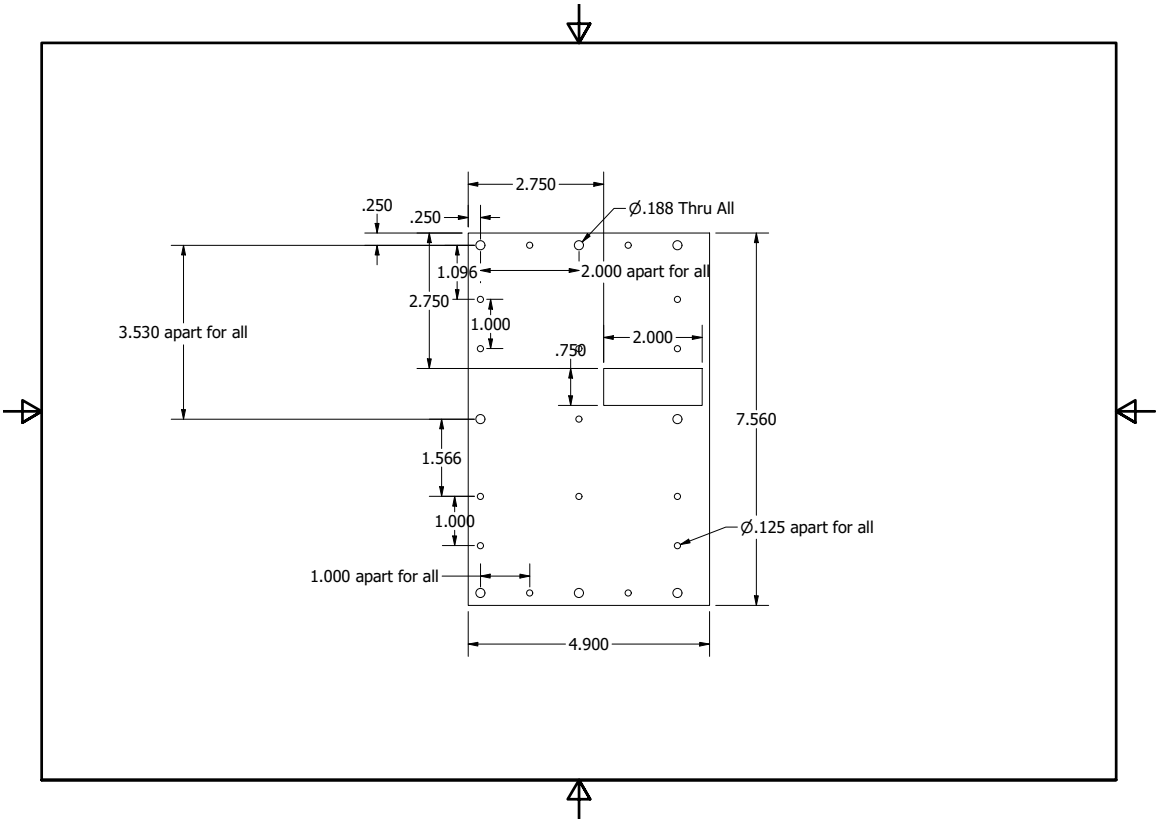

Figure A.3: 4K Sorb Plate Spec Side

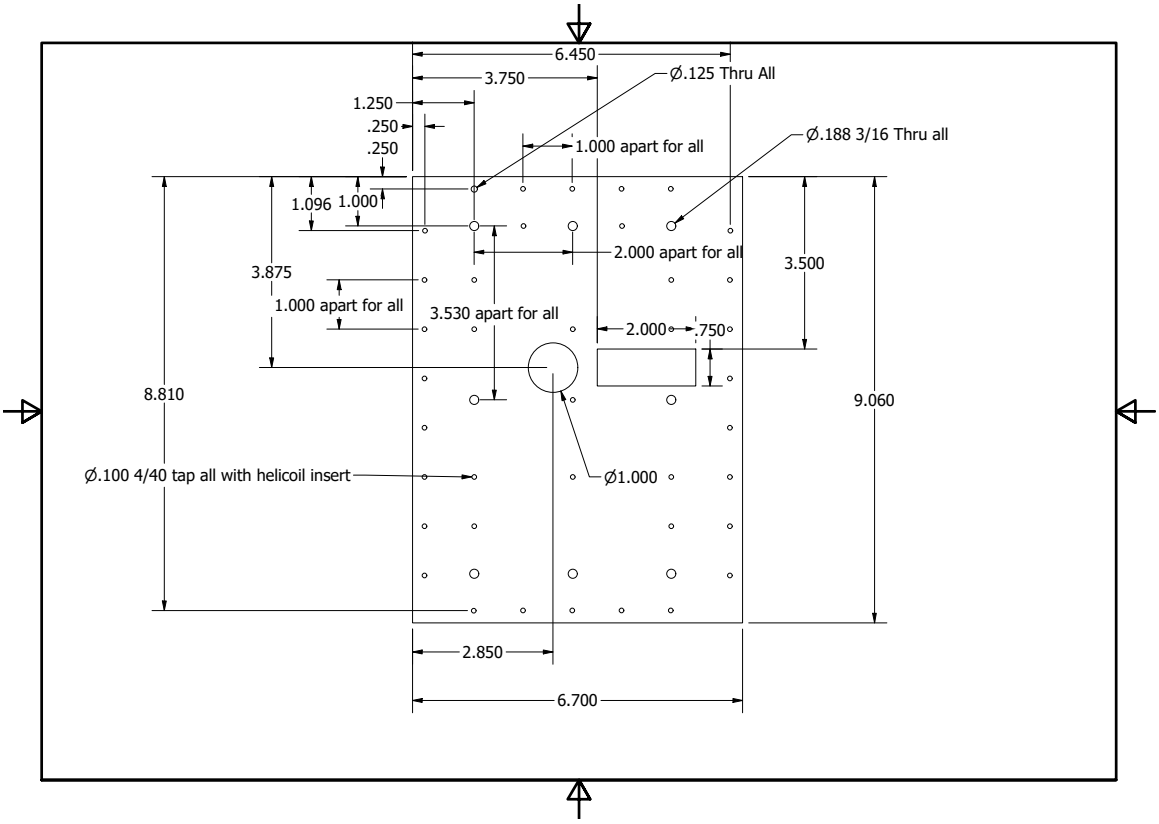

Figure A.4: 4K Inset Ablation Side

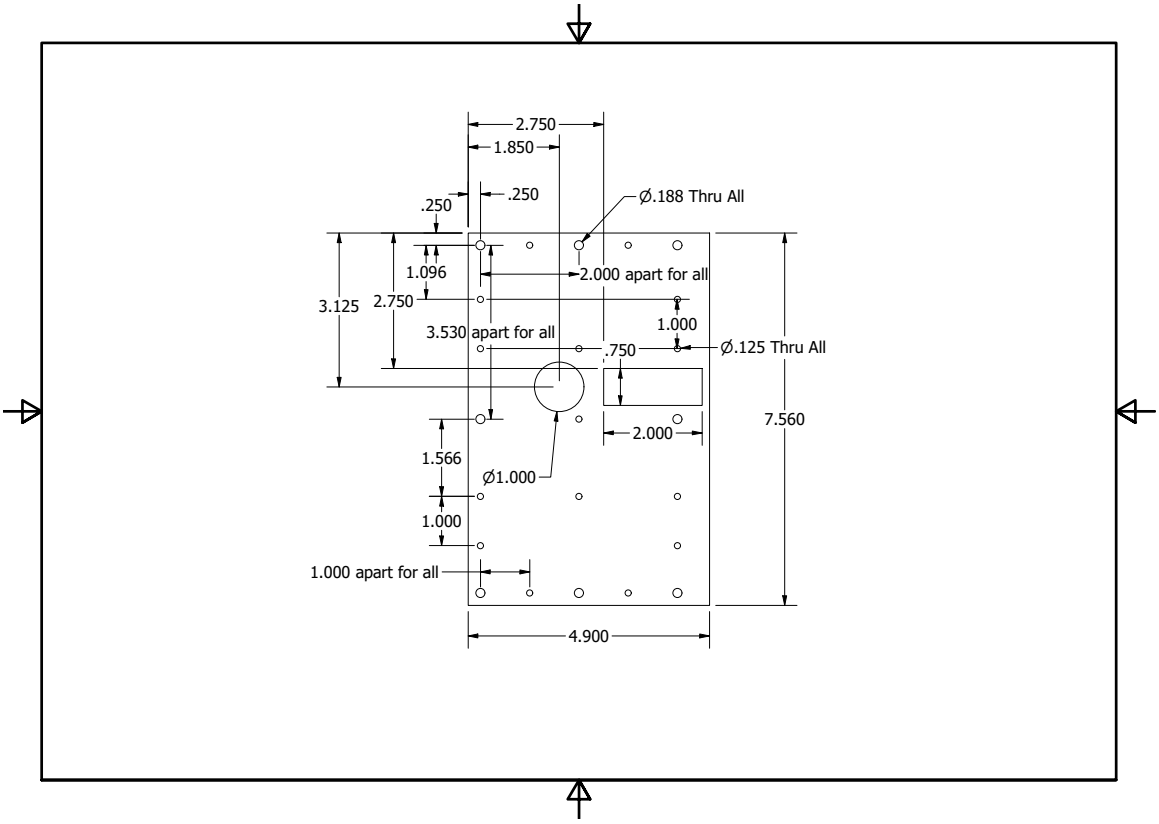

Figure A.5: 4K Sorb Plate Ablation Side

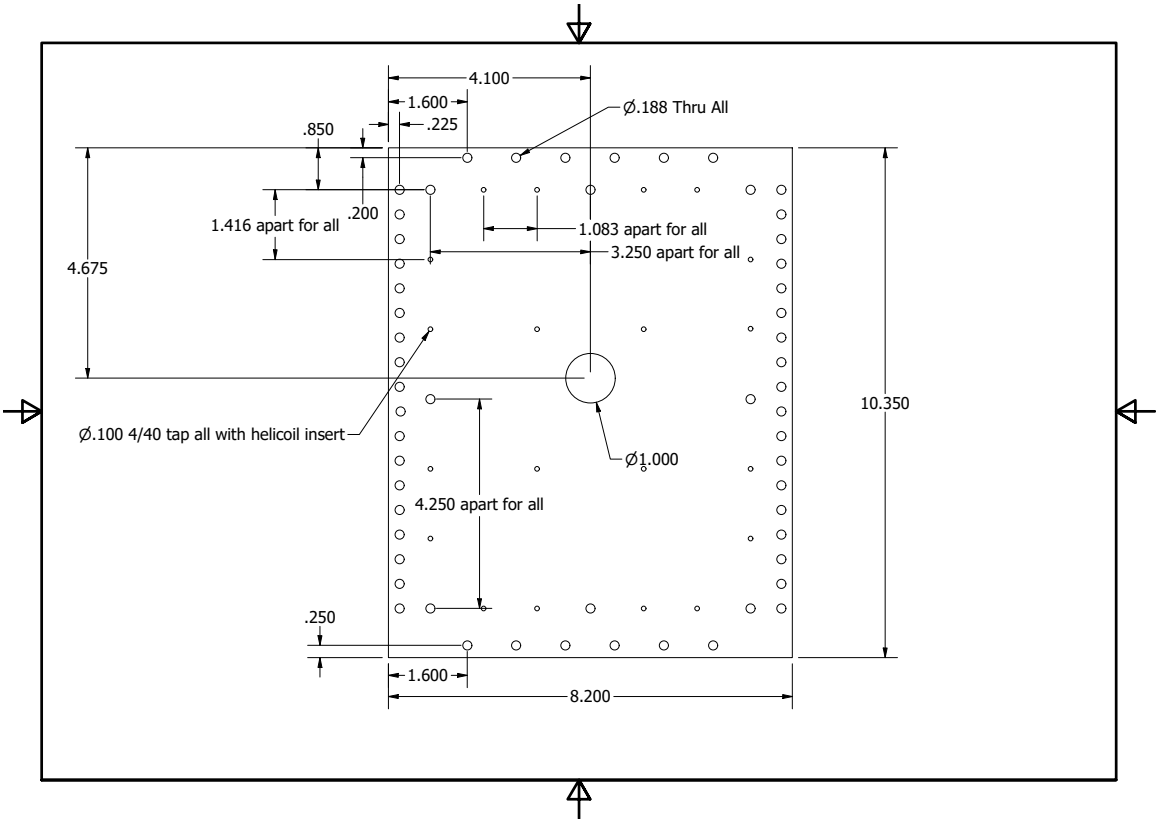

Figure A.6: 4K Molecule Exit Side

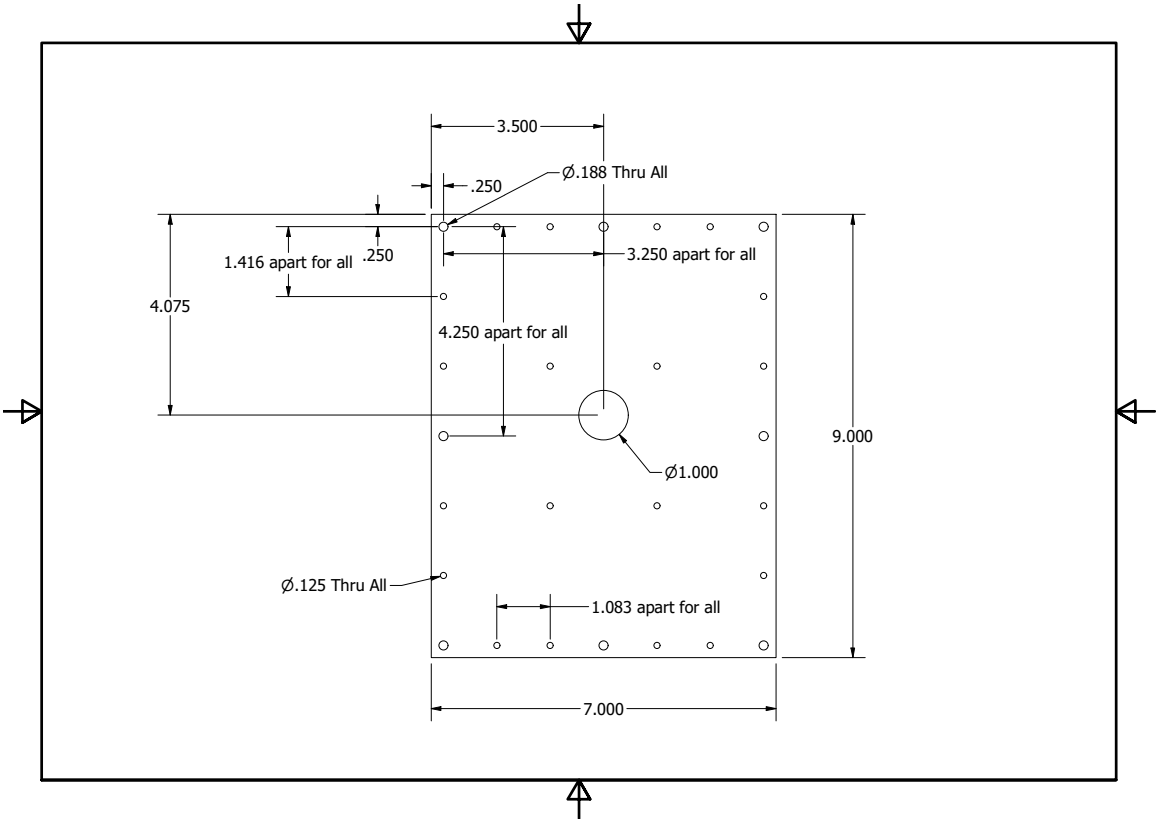

Figure A.7: 4K Sorb Plate Molecule Exit Side

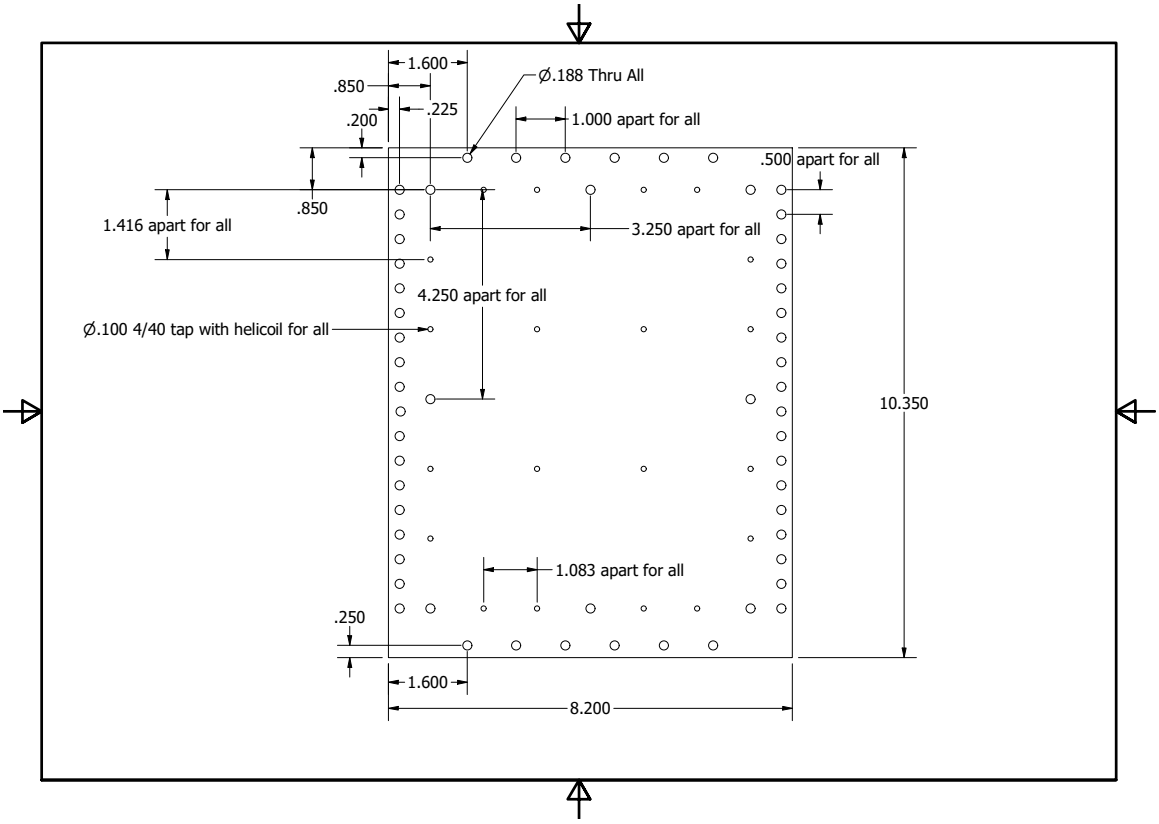

Figure A.8: 4K Blank

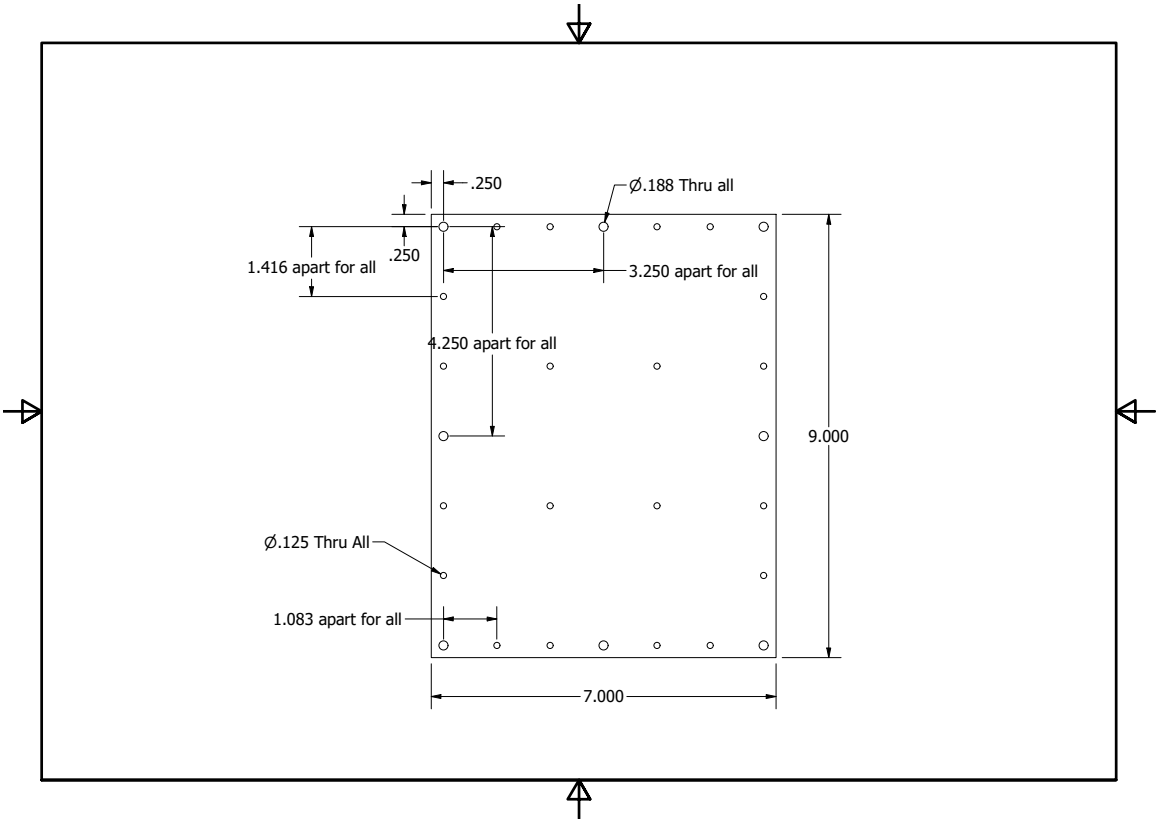

Figure A.9: 4K Sorb Plate Blank Side

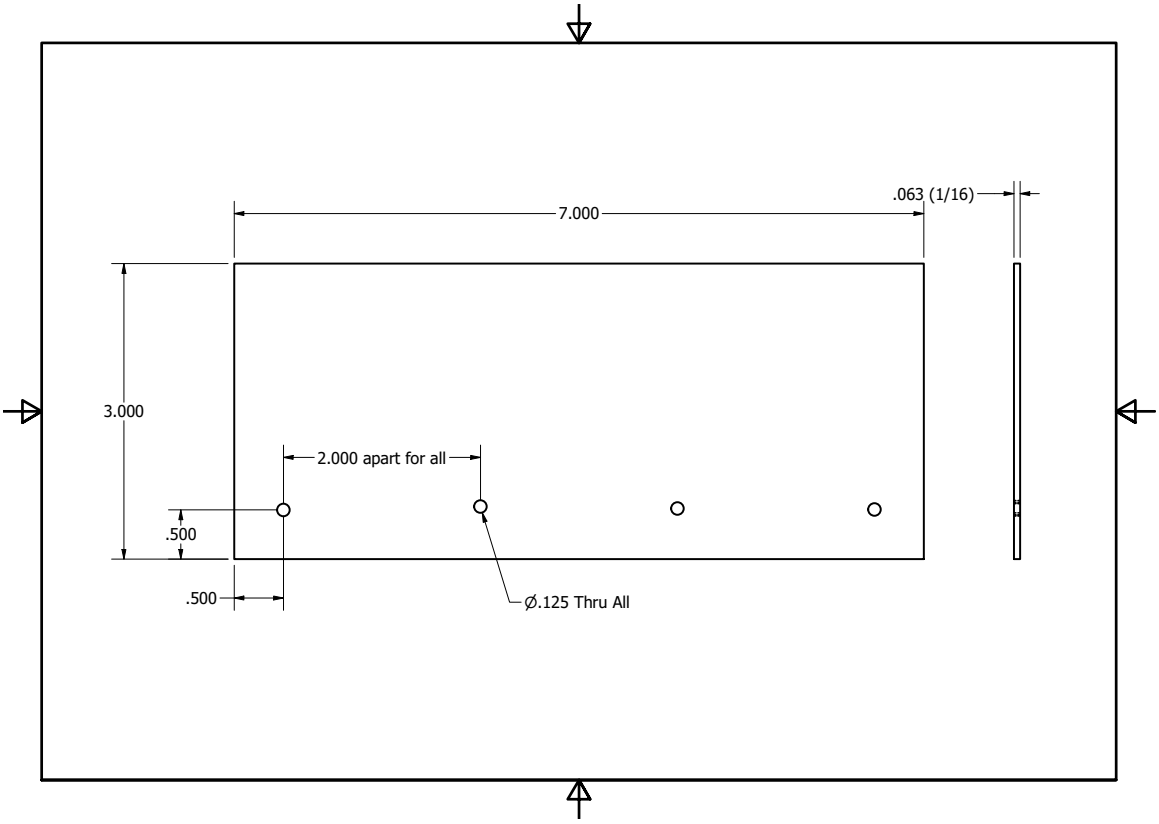

Figure A.10: 4K Bottom Sorb Sinks

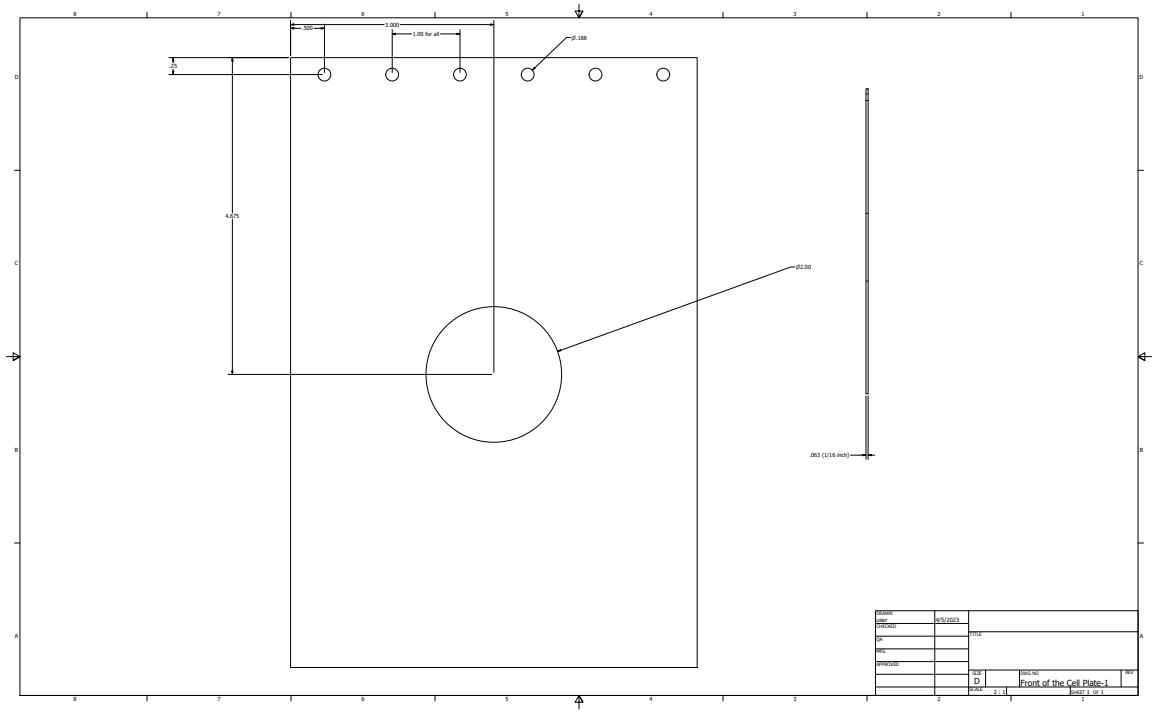

Figure A.11: Front of the Cell Plate

Appendix B

AlCl Molecular Constants

Below table shows the molecular constants for the $A^1\Pi$ state from our work[69] and for the $X^1\Sigma^+$ state from literature.

T_e	ω_e	$\omega_e x_e$	B_e	$\alpha_e \times 10^3$	$D_e \times 10^7$	R_e(Å)	Ref.
$A^1\Pi$							
38253.22(2)	452.54(5)	5.61(3)	0.24535(2)	2.652(7)		2.1220	$Al^{35}Cl$, exp.[69]
38253.718	446.26	5.04	0.243132	3.0341	2.707	2.1326	$Al^{35}Cl$, theo.[69]
38253.22(2)	447.19(5)	5.47(3)	0.23958(2)	2.559(7)		2.1220	$Al^{37}Cl$, exp.[69]
38253.711	440.98	4.92	0.237412	2.928	2.582	2.1325	$Al^{37}Cl$, theo.[69]
38267.55	441.6(2.3)	2.81(37)					[119]
38254.0	449.96	4.37	0.259	0.006		2.06	[130]
38436.3652	453.43	8.4793	0.2435			2.1324	[131] (theory)
38224.44	455.60		0.24078			2.1330	[80] (theory)
38303	471.81	9.61	0.2412			2.145	[81] (theory)
$X^1\Sigma^+$							
0.0	481.77	2.10	0.243930	1.611	2.502	2.1301	[94] ($Al^{35}Cl$)
0.0	476.07	2.05	0.238191	1.555	2.385	2.1301	[94] ($Al^{37}Cl$)

Appendix C

In Front of Cell Absorption Spectroscopy

For a while, we had atomic or molecular beams coming out of the cell with ≈ 400m/s as if they were room temperature beams in stead of cryogenic buffer gas beams. In order to see if it is something wrong with the cell, we did absorption spectroscopy on Yb in cell, through the slit between the first and second stage of the cell and in front of the cell as shown in figC.1 the below figure, with an absorption of 85%, 50% and 5% respectively, which are reasonable values that ruled out the problem that the molecules are somehow lost already in the cell.

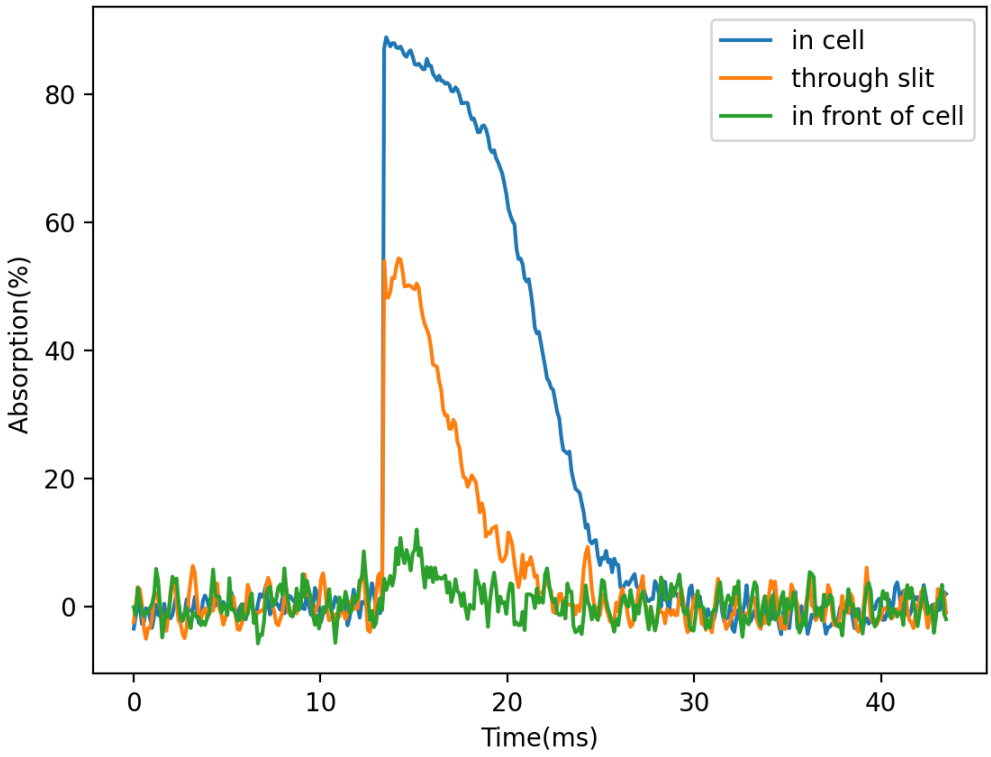

Figure C.1: Absorption spectroscopy time traces for Yb in cell, through the slit between the first and second stage of the cell and in front of cell. The corresponding absorption strengths are reasonable and indicate that the molecules are not lost in the cell.

Appendix D

Proper Procedure to Insert Indium in Between Copper Pieces

We gradually figured that it is important to have the cell pieces as tight as possible to avoid any leakage of the buffer gas, as that can cause insufficient buffer gas cooling. As of now, indium is used to put in between all the copper pieces to make seals. Below is a description of the proper procedure to insert indium in between copper pieces and figD.1 shows an example of attached indium on copper pieces.

Proper procedure: First of all, use 30 thousandths diameter(0.75mm) 99% pure indium wire. First, cut a piece of wire with the shape needed to fill in the interface, considering the amount that will be pressed flat such that it will not come out and block anything. Then use the arbor press in the machine shop, put the wire on top of the copper piece and sandwich them between two flat stainless steel plates(better to use fine grain sand paper to smooth the stainless steel), and press them down. Finally, lift and the

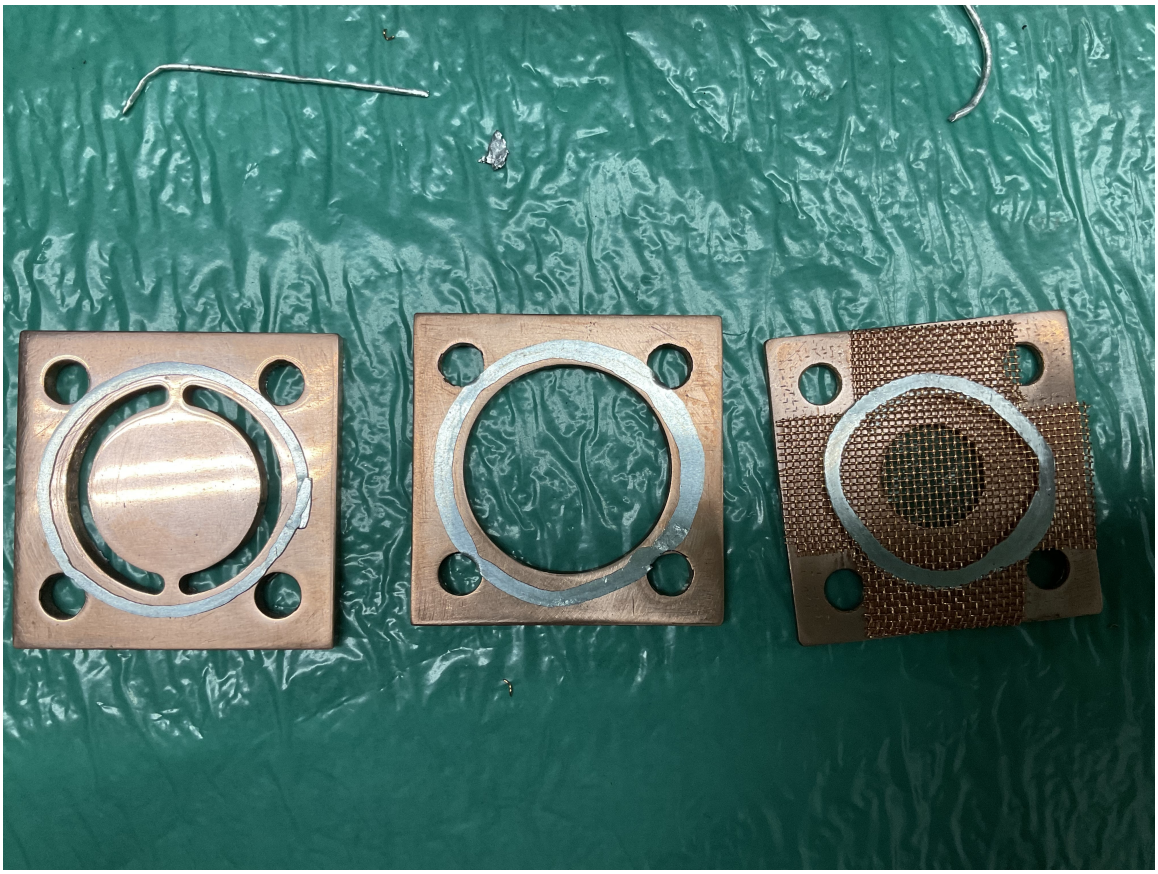

Figure D.1: Example of attached indium layer on copper pieces for the indium seal to prevent leakage of buffer gas from the cell.

indium should be in shape and flat and stick on the copper. If it sticks on the steel, use a sharp blade to carefully get the indium off and put on the copper, cover with the steel and press down with hand till the indium stick to the copper.

Bibliography

[1] T. H. Maiman. Stimulated Optical Radiation in Ruby. *Nature*, 187(4736):493–494, August 1960.

[2] A. L. Schawlow and C. H. Townes. Infrared and Optical Masers. *Physical Review*, 112(6):1940–1949, December 1958.

[3] T.W. Hänsch and A.L. Schawlow. Cooling of gases by laser radiation. *Optics Communications*, 13(1):68–69, January 1975.

[4] Steven Chu, J. E. Bjorkholm, A. Ashkin, and A. Cable. Experimental Observation of Optically Trapped Atoms. *Physical Review Letters*, 57(3):314–317, July 1986.

[5] William D. Phillips and Harold Metcalf. Laser Deceleration of an Atomic Beam. *Physical Review Letters*, 48(9):596–599, March 1982.

[6] Alan L. Migdall, John V. Prodan, William D. Phillips, Thomas H. Bergeman, and Harold J. Metcalf. First Observation of Magnetically Trapped Neutral Atoms. *Physical Review Letters*, 54(24):2596–2599, June 1985.

[7] E. L. Raab, M. Prentiss, Alex Cable, Steven Chu, and D. E. Pritchard. Trapping of Neutral Sodium Atoms with Radiation Pressure. *Physical Review Letters*, 59(23):2631–2634, December 1987.

[8] Malo Cadoret, Estefania De Mirandes, Pierre Cladé, Saïda Guellati-Khélifa, Catherine Schwob, François Nez, Lucile Julien, and François Biraben. Combination of Bloch Oscillations with a Ramsey-Bordé Interferometer: New Determination of the Fine Structure Constant. *Physical Review Letters*, 101(23):230801, December 2008.

[9] E. Peik, B. Lipphardt, H. Schnatz, T. Schneider, Chr. Tamm, and S. G. Karshenboim. Limit on the Present Temporal Variation of the Fine Structure Constant. *Physical Review Letters*, 93(17):170801, October 2004.

[10] M. Fischer, N. Kolachevsky, M. Zimmermann, R. Holzwarth, Th. Udem, T. W. Hänsch, M. Abgrall, J. Grünert, I. Maksimovic, S. Bize, H. Marion, F. Pereira Dos Santos, P. Lemonde, G. Santarelli, P. Laurent, A. Clairon, C. Salomon, M. Haas,

U. D. Jentschura, and C. H. Keitel. New Limits on the Drift of Fundamental Constants from Laboratory Measurements. *Physical Review Letters*, 92(23):230802, June 2004.

[11] Achim Peters, Keng Yeow Chung, and Steven Chu. Measurement of gravitational acceleration by dropping atoms. *Nature*, 400(6747):849–852, August 1999.

[12] M. Amoretti, C. Amsler, G. Bonomi, A. Bouchta, P. Bowe, C. Carraro, C. L. Cesar, M. Charlton, M. J. T. Collier, M. Doser, V. Filippini, K. S. Fine, A. Fontana, M. C. Fujiwara, R. Funakoshi, P. Genova, J. S. Hangst, R. S. Hayano, M. H. Holzscheiter, L. V. Jørgensen, V. Lagomarsino, R. Landua, D. Lindelöf, E. Lodi Rizzini, M. Macrì, N. Madsen, G. Manuzio, M. Marchesotti, P. Montagna, H. Pruys, C. Regenfus, P. Riedler, J. Rochet, A. Rotondi, G. Rouleau, G. Testera, A. Variola, T. L. Watson, and D. P. Van Der Werf. Production and detection of cold antihydrogen atoms. *Nature*, 419(6906):456–459, October 2002.

[13] J. B. Fixler, G. T. Foster, J. M. McGuirk, and M. A. Kasevich. Atom Interferometer Measurement of the Newtonian Constant of Gravity. *Science*, 315(5808):74–77, January 2007.

[14] C. Salomon, J. Dalibard, A. Aspect, H. Metcalf, and C. Cohen-Tannoudji. Channeling atoms in a laser standing wave. *Physical Review Letters*, 59(15):1659–1662, October 1987.

[15] P Verkerk, D. R Meacher, A. B Coates, J.-Y Courtois, S Guibal, B Lounis, C Salomon, and G Grynberg. Designing Optical Lattices: An Investigation with Cesium Atoms. *Europhysics Letters (EPL)*, 26(3):171–176, April 1994.

[16] M. H. Anderson, J. R. Ensher, M. R. Matthews, C. E. Wieman, and E. A. Cornell. Observation of Bose-Einstein Condensation in a Dilute Atomic Vapor. *Science*, 269(5221):198–201, July 1995.

[17] K. B. Davis, M. O. Mewes, M. R. Andrews, N. J. Van Druten, D. S. Durfee, D. M. Kurn, and W. Ketterle. Bose-Einstein Condensation in a Gas of Sodium Atoms. *Physical Review Letters*, 75(22):3969–3973, November 1995.

[18] Daniel Greif, Thomas Uehlinger, Gregor Jotzu, Leticia Tarruell, and Tilman Esslinger. Short-Range Quantum Magnetism of Ultracold Fermions in an Optical Lattice. *Science*, 340(6138):1307–1310, June 2013.

[19] A. D. Ludlow, T. Zelevinsky, G. K. Campbell, S. Blatt, M. M. Boyd, M. H. G. De Miranda, M. J. Martin, J. W. Thomsen, S. M. Foreman, Jun Ye, T. M. Fortier, J. E. Stalnaker, S. A. Diddams, Y. Le Coq, Z. W. Barber, N. Poli, N. D. Lemke, K. M. Beck, and C. W. Oates. Sr Lattice Clock at 1×10^{-16} Fractional Uncertainty by Remote Optical Evaluation with a Ca Clock. *Science*, 319(5871):1805–1808, March 2008.

[20] T. Rosenband, D. B. Hume, P. O. Schmidt, C. W. Chou, A. Brusch, L. Lorini, W. H. Oskay, R. E. Drullinger, T. M. Fortier, J. E. Stalnaker, S. A. Diddams, W. C. Swann, N. R. Newbury, W. M. Itano, D. J. Wineland, and J. C. Bergquist. Frequency Ratio of Al $^+$ and Hg $^+$ Single-Ion Optical Clocks; Metrology at the 17th Decimal Place. *Science*, 319(5871):1808–1812, March 2008.

[21] Tobias Bothwell, Dhruv Kedar, Eric Oelker, John M Robinson, Sarah L Bromley, Weston L Tew, Jun Ye, and Colin J Kennedy. JILA SrI optical lattice clock with uncertainty of \$2.0 \\times 10ˆ{-18}\$. *Metrologia*, 56(6):065004, December 2019.

[22] S.M. Brewer, J.-S. Chen, A.M. Hankin, E.R. Clements, C.W. Chou, D.J. Wineland, D.B. Hume, and D.R. Leibrandt. Al + 27 Quantum-Logic Clock with a Systematic Uncertainty below 10 18. *Physical Review Letters*, 123(3):033201, July 2019.

[23] Stephan Wildermuth, Sebastian Hofferberth, Igor Lesanovsky, Elmar Haller, L. Mauritz Andersson, Sönke Groth, Israel Bar-Joseph, Peter Krüger, and Jörg Schmiedmayer. Microscopic magnetic-field imaging. *Nature*, 435(7041):440–440, May 2005.

[24] M Saffman. Quantum computing with atomic qubits and Rydberg interactions: progress and challenges. *Journal of Physics B: Atomic, Molecular and Optical Physics*, 49(20):202001, October 2016.

[25] Eric R. Hudson, H. J. Lewandowski, Brian C. Sawyer, and Jun Ye. Cold Molecule Spectroscopy for Constraining the Evolution of the Fine Structure Constant. *Physical Review Letters*, 96(14):143004, April 2006.

[26] V. V. Flambaum and M. G. Kozlov. Enhanced Sensitivity to the Time Variation of the Fine-Structure Constant and m p / m e in Diatomic Molecules. *Physical Review Letters*, 99(15):150801, October 2007.

[27] D. DeMille, S. Sainis, J. Sage, T. Bergeman, S. Kotochigova, and E. Tiesinga. Enhanced Sensitivity to Variation of m e / m p in Molecular Spectra. *Physical Review Letters*, 100(4):043202, January 2008.

[28] T. Zelevinsky, S. Kotochigova, and Jun Ye. Precision Test of Mass-Ratio Variations with Lattice-Confined Ultracold Molecules. *Physical Review Letters*, 100(4):043201, January 2008.

[29] Cheng Chin, V V Flambaum, and M G Kozlov. Ultracold molecules: new probes on the variation of fundamental constants. *New Journal of Physics*, 11(5):055048, May 2009.

[30] J. J. Hudson, B. E. Sauer, M. R. Tarbutt, and E. A. Hinds. Measurement of the Electron Electric Dipole Moment Using YbF Molecules. *Physical Review Letters*, 89(2):023003, June 2002.

[31] M. R. Tarbutt, J. J. Hudson, B. E. Sauer, and E. A. Hinds. Prospects for measuring the electric dipole moment of the electron using electrically trapped polar molecules. *Faraday Discussions*, 142:37, 2009.

[32] A C Vutha, W C Campbell, Y V Gurevich, N R Hutzler, M Parsons, D Patterson, E Petrik, B Spaun, J M Doyle, G Gabrielse, and D DeMille. Search for the electric dipole moment of the electron with thorium monoxide. *Journal of Physics B: Atomic, Molecular and Optical Physics*, 43(7):074007, April 2010.

[33] J. J. Hudson, D. M. Kara, I. J. Smallman, B. E. Sauer, M. R. Tarbutt, and E. A. Hinds. Improved measurement of the shape of the electron. *Nature*, 473(7348):493–496, May 2011.

[34] D. DeMille, S. B. Cahn, D. Murphree, D. A. Rahmlow, and M. G. Kozlov. Using Molecules to Measure Nuclear Spin-Dependent Parity Violation. *Physical Review Letters*, 100(2):023003, January 2008.

[35] M G Kozlov and L N Labzowsky. Parity violation effects in diatomics. *Journal of Physics B: Atomic, Molecular and Optical Physics*, 28(10):1933–1961, May 1995.

[36] T. A. Isaev, S. Hoekstra, and R. Berger. Laser-cooled RaF as a promising candidate to measure molecular parity violation. *Physical Review A*, 82(5):052521, November 2010.

[37] N.J. Fitch and M.R. Tarbutt. Laser-cooled molecules. In *Advances In Atomic, Molecular, and Optical Physics*, volume 70, pages 157–262. Elsevier, 2021.

[38] M. A. Baranov, Klaus Osterloh, and M. Lewenstein. Fractional Quantum Hall States in Ultracold Rapidly Rotating Dipolar Fermi Gases. *Physical Review Letters*, 94(7):070404, February 2005.

[39] L. Pollet, J. D. Picon, H. P. Büchler, and M. Troyer. Supersolid Phase with Cold Polar Molecules on a Triangular Lattice. *Physical Review Letters*, 104(12):125302, March 2010.

[40] K. Góral, L. Santos, and M. Lewenstein. Quantum Phases of Dipolar Bosons in Optical Lattices. *Physical Review Letters*, 88(17):170406, April 2002.

[41] Ryan Barnett, Dmitry Petrov, Mikhail Lukin, and Eugene Demler. Quantum Magnetism with Multicomponent Dipolar Molecules in an Optical Lattice. *Physical Review Letters*, 96(19):190401, May 2006.

[42] D. DeMille. Quantum Computation with Trapped Polar Molecules. *Physical Review Letters*, 88(6):067901, January 2002.

[43] S. F. Yelin, K. Kirby, and Robin Côté. Schemes for robust quantum computation with polar molecules. *Physical Review A*, 74(5):050301, November 2006.

[44] R. V. Krems. Cold controlled chemistry. *Physical Chemistry Chemical Physics*, 10(28):4079, 2008.

[45] Matthew T. Hummon, Timur V. Tscherbul, Jacek Kłos, Hsin-I Lu, Edem Tsikata, Wesley C. Campbell, Alexander Dalgarno, and John M. Doyle. Cold N + NH Collisions in a Magnetic Trap. *Physical Review Letters*, 106(5):053201, February 2011.

[46] N. Balakrishnan. Perspective: Ultracold molecules and the dawn of cold controlled chemistry. *The Journal of Chemical Physics*, 145(15):150901, October 2016.

[47] J. F. E. Croft, N. Balakrishnan, and B. K. Kendrick. Long-lived complexes and signatures of chaos in ultracold K 2 +Rb collisions. *Physical Review A*, 96(6):062707, December 2017.

[48] Mikhail Lemeshko, Roman V. Krems, John M. Doyle, and Sabre Kais. Manipulation of molecules with electromagnetic fields. *Molecular Physics*, 111(12-13):1648–1682, July 2013.

[49] A. V. Gorshkov, P. Rabl, G. Pupillo, A. Micheli, P. Zoller, M. D. Lukin, and H. P. Büchler. Suppression of Inelastic Collisions Between Polar Molecules With a Repulsive Shield. *Physical Review Letters*, 101(7):073201, August 2008.

[50] Goulven Quéméner and John L. Bohn. Shielding 2 ultracold dipolar molecular collisions with electric fields. *Physical Review A*, 93(1):012704, January 2016.

[51] Kevin M. Jones, Eite Tiesinga, Paul D. Lett, and Paul S. Julienne. Ultracold photoassociation spectroscopy: Long-range molecules and atomic scattering. *Reviews of Modern Physics*, 78(2):483–535, May 2006.

[52] C Haimberger, J Kleinert, P Zabawa, A Wakim, and N P Bigelow. Formation of ultracold, highly polar X ^{1} $^+$ NaCs molecules. *New Journal of Physics*, 11(5):055042, May 2009.

[53] Andrew J. Kerman, Jeremy M. Sage, Sunil Sainis, Thomas Bergeman, and David DeMille. Production of Ultracold, Polar R b C s * Molecules via Photoassociation. *Physical Review Letters*, 92(3):033004, January 2004.

[54] Alessandro Volpi and John L. Bohn. Magnetic-field effects in ultracold molecular collisions. *Physical Review A*, 65(5):052712, May 2002.

[55] K.-K. Ni, S. Ospelkaus, M. H. G. De Miranda, A. Pe'er, B. Neyenhuis, J. J. Zirbel, S. Kotochigova, P. S. Julienne, D. S. Jin, and J. Ye. A High Phase-Space-Density Gas of Polar Molecules. *Science*, 322(5899):231–235, October 2008.

[56] M. D. Rosa. Laser-cooling molecules: Concept, candidates, and supporting hyperfine-resolved measurements of rotational lines in the A-X(0,0) band of CaH. *The European Physical Journal D*, 31(2):395–402, November 2004.

[57] John M. Brown and Alan Carrington. *Rotational spectroscopy of diatomic molecules*. Cambridge molecular science series. Cambridge University Press, Cambridge ; New York, 2003.

[58] Peter F. Bernath. *Spectra of atoms and molecules*. Oxford University Press, Oxford ; New York, third edition edition, 2016.

[59] Alejandra L Collopy, Matthew T Hummon, Mark Yeo, Bo Yan, and Jun Ye. Prospects for a narrow line MOT in YO. *New Journal of Physics*, 17(5):055008, May 2015.

[60] K.R. Vogel, T.P. Dinneen, A. Gallagher, and J.L. Hall. Narrow-line Doppler cooling of strontium to the recoil limit. *IEEE Transactions on Instrumentation and Measurement*, 48(2):618–621, April 1999.

[61] J. F. Barry, D. J. McCarron, E. B. Norrgard, M. H. Steinecker, and D. DeMille. Magneto-optical trapping of a diatomic molecule. *Nature*, 512(7514):286–289, August 2014.

[62] S. Truppe, H. J. Williams, M. Hambach, L. Caldwell, N. J. Fitch, E. A. Hinds, B. E. Sauer, and M. R. Tarbutt. Molecules cooled below the Doppler limit. *Nature Physics*, 13(12):1173–1176, December 2017.

[63] Loïc Anderegg, Benjamin L. Augenbraun, Eunmi Chae, Boerge Hemmerling, Nicholas R. Hutzler, Aakash Ravi, Alejandra Collopy, Jun Ye, Wolfgang Ketterle, and John M. Doyle. Radio Frequency Magneto-Optical Trapping of CaF with High Density. *Physical Review Letters*, 119(10):103201, September 2017.

[64] Alejandra L. Collopy, Shiqian Ding, Yewei Wu, Ian A. Finneran, Loïc Anderegg, Benjamin L. Augenbraun, John M. Doyle, and Jun Ye. 3D Magneto-Optical Trap of Yttrium Monoxide. *Physical Review Letters*, 121(21):213201, November 2018.

[65] S. Truppe, S. Marx, S. Kray, M. Doppelbauer, S. Hofsäss, H. C. Schewe, N. Walter, J. Pérez-Ríos, B. G. Sartakov, and G. Meijer. Spectroscopic characterization of aluminum monofluoride with relevance to laser cooling and trapping. *Physical Review A*, 100(5):052513, November 2019.

[66] S Hofsäss, M Doppelbauer, S C Wright, S Kray, B G Sartakov, J Pérez-Ríos, G Meijer, and S Truppe. Optical cycling of AlF molecules. *New Journal of Physics*, 23(7):075001, July 2021.

[67] E. B. Norrgard, E. R. Edwards, D. J. McCarron, M. H. Steinecker, D. DeMille, Shah Saad Alam, S. K. Peck, N. S. Wadia, and L. R. Hunter. Hyperfine structure of the B 3 1 state and predictions of optical cycling behavior in the X → B transition of TlF. *Physical Review A*, 95(6):062506, June 2017.

[68] N. B. Clayburn, T. H. Wright, E. B. Norrgard, D. DeMille, and L. R. Hunter. Measurement of the molecular dipole moment and the hyperfine and -doublet splittings of the B 1 3 state of thallium fluoride. *Physical Review A*, 102(5):052802, November 2020.

[69] John R. Daniel, Chen Wang, Kayla Rodriguez, Boerge Hemmerling, Taylor N. Lewis, Christopher Bardeen, Alexander Teplukhin, and Brian K. Kendrick. Spectroscopy on the A 1 ← X + 1 transition of buffer-gas-cooled AlCl. *Physical Review A*, 104(1):012801, July 2021.

[70] Taylor N. Lewis, Chen Wang, John R. Daniel, Madhav Dhital, Christopher J. Bardeen, and Boerge Hemmerling. Optimizing pulsed-laser ablation production of AlCl molecules for laser cooling. *Physical Chemistry Chemical Physics*, 23(39):22785–22793, 2021.

[71] C. J. Foot. *Atomic physics*. Number 7. Atomic, Optical, and laser physics in Oxford master series in physics. Oxford University Press, Oxford ; New York, 2005. OCLC: ocm57478010.

[72] Harold J. Metcalf and Peter Van der Straten. *Laser cooling and trapping*. Graduate texts in contemporary physics. Springer, New York, 1999.

[73] W. Jevons. Spectroscopic investigations in connection with the active modification of nitrogen. III.—Spectra developed by the tetrachlorides of silicon and titanium. *Proceedings of the Royal Society of London. Series A, Containing Papers of a Mathematical and Physical Character*, 89(609):187–193, August 1913.

[74] W. Jevons. On the band-spectra of silicon oxide and chloride, and chlorides of carbon, boron, and aluminium. *Proceedings of the Royal Society of London. Series A, Containing Papers of a Mathematical and Physical Character*, 106(736):174–194, August 1924.

[75] B.N. Bhaduri. Band spectrum of aluminium chloride (AlCl). *Proceedings of the Royal Society of London. Series A, Containing Papers of a Mathematical and Physical Character*, 145(854):321–336, June 1934.

[76] P. C. Mahanti. Das Bandenspektrum des Aluminiumchlorids. *Zeitschrift fr Physik*, 88(7-8):550–558, July 1934.

[77] Ram Samujh Ram, S B Rai, K N Upadhya, and D K Rai. The $A\ ^1$ - $X\ ^1\ ^+$, $a\ ^3$ - $X\ ^1\ ^+$ and $b\ ^3\ ^+$ - $a\ ^3$ Systems of AlCl. *Physica Scripta*, 26(5):383–397, November 1982.

[78] Donald F. Rogowski and Arthur Fontijn. The radiative lifetime of AlCl A 1. *Chemical Physics Letters*, 137(3):219–222, June 1987.

[79] Stephen R. Langhoff, Charles W. Bauschlicher, and Peter R. Taylor. Theoretical studies of AlF, AlCl, and AlBr. *The Journal of Chemical Physics*, 88(9):5715–5725, May 1988.

[80] Mingjie Wan, Di Yuan, Chengguo Jin, Fanhou Wang, Yujie Yang, You Yu, and Juxiang Shao. Laser cooling of the AlCl molecule with a three-electronic-level theoretical model. *The Journal of Chemical Physics*, 145(2):024309, July 2016.

[81] Rong Yang, Bin Tang, and Tao Gao. *Ab initio* study on the electronic states and laser cooling of AlCl and AlBr. *Chinese Physics B*, 25(4):043101, April 2016.

[82] Jinping Zhang, Hui Li, and Yanqin Ma. Rovibrational properties of the A1 – X1+ system of the AlCl radical. *Computational and Theoretical Chemistry*, 1202:113307, August 2021.

[83] Xianquan Yu, Jinchao Mo, Tiangao Lu, Ting You Tan, and Travis L. Nicholson. Magneto-optical trapping of a group-III atom. *Physical Review A*, 105(6):L061101, June 2022.

[84] Kouji Yasuda, Kunio Saegusa, and Toru H. Okabe. New Method for Production of Solar-Grade Silicon by Subhalide Reduction. *MATERIALS TRANSACTIONS*, 50(12):2873–2878, 2009.

[85] Kouji Yasuda, Kunio Saegusa, and Toru H. Okabe. Production of Solar-grade Silicon by Halidothermic Reduction of Silicon Tetrachloride. *Metallurgical and Materials Transactions B*, 42(1):37–49, February 2011.

[86] W. Mcgregor, J. Drakes, K. Beale, and F. Sherrell. The AlCl absorption feature in solid rocket plume radiation. In *27th Thermophysics Conference*, Nashville,TN,U.S.A., July 1992. American Institute of Aeronautics and Astronautics.

[87] Matthias Tacke and Hansgeorg Schnoeckel. Metastable aluminum chloride, AlCl, as a solid and in solution. *Inorganic Chemistry*, 28(14):2895–2896, July 1989.

[88] T. Tsuji. Molecular abundances in stellar atmospheres. II. *Astronomy and Astrophysics, Vol. 23, p. 411 - 431.*

[89] Lucy M. Ziurys. The chemistry in circumstellar envelopes of evolved stars: Following the origin of the elements to the origin of life. *Proceedings of the National Academy of Sciences*, 103(33):12274–12279, August 2006.

[90] M. Agúndez, J. P. Fonfría, J. Cernicharo, C. Kahane, F. Daniel, and M. Guélin. Molecular abundances in the inner layers of IRC +10216. *Astronomy & Astrophysics*, 543:A48, July 2012.

[91] L. Decin, A. M. S. Richards, L. B. F. M. Waters, T. Danilovich, D. Gobrecht, T. Khouri, W. Homan, J. M. Bakker, M. Van De Sande, J. A. Nuth, and E. De Beck. Study of the aluminium content in AGB winds using ALMA: Indications for the presence of gas-phase $(Al_2O_3)_n$ clusters. *Astronomy & Astrophysics*, 608:A55, December 2017.

[92] Martin Asplund, Nicolas Grevesse, A. Jacques Sauval, and Pat Scott. The Chemical Composition of the Sun. *Annual Review of Astronomy and Astrophysics*, 47(1):481–522, September 2009.

[93] J. L. Dunham. The Energy Levels of a Rotating Vibrator. *Physical Review*, 41(6):721–731, September 1932.

[94] H. G. Hedderich, M. Dulick, and P. F. Bernath. High resolution emission spectroscopy of AlCl at 20 . *The Journal of Chemical Physics*, 99(11):8363–8370, December 1993.

[95] J. Hoeft, T. Törring, and E. Tiemann. Hyperfeinstruktur von AlCl und AlBr / Hyperfine Structure of AlCl and AlBr. *Zeitschrift für Naturforschung A*, 28(7):1066–1068, July 1973.

[96] J. C. Shaw. *Prospects for laser cooling and trapping aluminum monochloride.* PhD thesis, University of Connecticut, 2022.

[97] J. R. Daniel, J. C. Shaw, C. Wang, L. R. Liu, B. K. Kendrick, B. Hemmerling, and D. J. McCarron. Hyperfine structure of the $\mathbf{A^{1}}$ state of AlCl and its relevance to laser cooling and trapping. 2023. Publisher: arXiv Version Number: 1.

[98] Norman Ramsey. *Molecular beams*. The International series of monographs on physics. Clarendon Press ; Oxford University Press, Oxford : New York, 1985.

[99] S. A. Rangwala, T. Junglen, T. Rieger, P. W. H. Pinkse, and G. Rempe. Continuous source of translationally cold dipolar molecules. *Physical Review A*, 67(4):043406, April 2003.

[100] D H Levy. Laser Spectroscopy of Cold Gas-Phase Molecules. *Annual Review of Physical Chemistry*, 31(1):197–225, October 1980.

[101] Roman Krems, Bretislav Friedrich, and William C Stwalley, editors. *Cold Molecules: Theory, Experiment, Applications*. CRC Press, 0 edition, June 2009.

[102] Jonathan D. Weinstein, Robert deCarvalho, Thierry Guillet, Bretislav Friedrich, and John M. Doyle. Magnetic trapping of calcium monohydride molecules at millikelvin temperatures. *Nature*, 395(6698):148–150, September 1998.

[103] David Patterson and John M. Doyle. Bright, guided molecular beam with hydrodynamic enhancement. *The Journal of Chemical Physics*, 126(15):154307, April 2007.

[104] David Patterson, Julia Rasmussen, and John M Doyle. Intense atomic and molecular beams via neon buffer-gas cooling. *New Journal of Physics*, 11(5):055018, May 2009.

[105] Jack W. Ekin. *Experimental techniques for low temperature measurements: cryostat design, material properties, and superconductor critical-current testing*. Oxford Univ. Press, Oxford, repr edition, 2014.

[106] Hsin-I Lu, Julia Rasmussen, Matthew J. Wright, Dave Patterson, and John M. Doyle. A cold and slow molecular beam. *Physical Chemistry Chemical Physics*, 13(42):18986, 2011.

[107] John R. Daniel. *Assessment of AlCl as a Candidate for Laser Slowing*. PhD thesis, University of California, Riverside, September 2022.

[108] H.K. Tönshoff, D. Hesse, and J. Mommsen. Micromachining Using Excimer Lasers. *CIRP Annals - Manufacturing Technology*, 42(1):247–251, January 1993.

[109] F. K. Tittel, I. S. Saidi, G. H. Pettit, P. J. Wisoff, and R. Sauerbrey. Excimer Lasers In Medicine. page 219, Los Angeles, CA, United States, June 1989.

[110] J. C. Shaw, S. Hannig, and D. J. McCarron. Stable 2 W continuous-wave 261.5 nm laser for cooling and trapping aluminum monochloride. *Optics Express*, 29(23):37140, November 2021.

[111] T.W. Hansch and B. Couillaud. Laser frequency stabilization by polarization spectroscopy of a reflecting reference cavity. *Optics Communications*, 35(3):441–444, December 1980.

[112] Robert W. Boyd. *Nonlinear optics*. Academic Press is an imprint of Elsevier, San Diego, 4 edition, 2019.

[113] Daniel A. Steck. Rubidium 87 D Line Data," available online at http://steck.us/alkalidata.

[114] V Jacques, B Hingant, A Allafort, M Pigeard, and J F Roch. Nonlinear spectroscopy of rubidium: an undergraduate experiment. *European Journal of Physics*, 30(5):921–934, September 2009.

[115] Annie Hansson and James K.G. Watson. A comment on Hönl-London factors. *Journal of Molecular Spectroscopy*, 233(2):169–173, October 2005.

[116] James K.G. Watson. The isotope dependence of the equilibrium rotational constants in 1 states of diatomic molecules. *Journal of Molecular Spectroscopy*, 45(1):99–113, January 1973.

[117] James K.G. Watson. The isotope dependence of diatomic Dunham coefficients. *Journal of Molecular Spectroscopy*, 80(2):411–421, April 1980.

[118] Devendra Sharma. Two New Band Systems of the AlCl Molecule. *The Astrophysical Journal*, 113:210, January 1951.

[119] E. Mahieu, I. Dubois, and H. Bredohl. The triplet states of AlCl. *Journal of Molecular Spectroscopy*, 138(1):264–271, November 1989.

[120] E. Mahieu, I. Dubois, and H. Bredohl. The triplet states of AlCl. *Journal of Molecular Spectroscopy*, 138(1):264–271, November 1989.

[121] M.D. Saksena, V.S. Dixit, and Mahavir Singh. Rotational Analysis of the 0–0 Band of thea3–X1+Transition of AlCl. *Journal of Molecular Spectroscopy*, 187(1):1–5, January 1998.

[122] David R. Lide. Microwave Spectrum of Perchlorylfluoride. *The Journal of Chemical Physics*, 43(10):3767–3768, November 1965.

[123] Hans-Jörg Himmel. Characterization of Oligomers of AlCl: Al–Cl versus Al–Al Bonding. *European Journal of Inorganic Chemistry*, 2005(10):1886–1894, May 2005.

[124] F. C. Wyse and Walter Gordy. Millimeter Wave Rotational Spectra of AlCl, AlBr, and AlI. *The Journal of Chemical Physics*, 56(5):2130–2136, March 1972.

[125] Peter M. Futerko and Arthur Fontijn. Experimental and transition-state theory studies of the gas-phase reactions of monochloroaluminum with nitrous oxide, carbon dioxide, and sulfur dioxide. *The Journal of Physical Chemistry*, 97(28):7222–7227, July 1993.

[126] David V. Dearden, Russell D. Johnson, and Jeffrey W. Hudgens. Aluminum monochloride excited states observed by resonance-enhanced multiphoton ionization spectroscopy. *The Journal of Chemical Physics*, 99(10):7521–7528, November 1993.

[127] Antoine Aerts and Alex Brown. A revised nuclear quadrupole moment for aluminum: Theoretical nuclear quadrupole coupling constants of aluminum compounds. *The Journal of Chemical Physics*, 150(22):224302, June 2019.

[128] R. E. Alonso, A. Svane, C. O. Rodríguez, and N. E. Christensen. Nuclear quadrupole moment determination of 35 Cl , 79 Br , and 127 I. *Physical Review B*, 69(12):125101, March 2004.

[129] Eunmi Chae. *Laser Slowing of CaF Molecules and Progress towards a Dual-MOT for Li and CaF*. PhD thesis, Harvard University, November 2015.

[130] Peter Linstrom. NIST Chemistry WebBook, NIST Standard Reference Database 69, 1997.

[131] Jian-Gang Xu, Cong-Ying Zhang, and Yun-Guang Zhang. Vibronic spectra of aluminium monochloride relevant to circumstellar molecule*. *Chinese Physics B*, 29(3):033102, March 2020.

[132] J. K. Webb, M. T. Murphy, V. V. Flambaum, V. A. Dzuba, J. D. Barrow, C. W. Churchill, J. X. Prochaska, and A. M. Wolfe. Further Evidence for Cosmological Evolution of the Fine Structure Constant. *Physical Review Letters*, 87(9):091301, August 2001.

[133] Lincoln D Carr, David DeMille, Roman V Krems, and Jun Ye. Cold and ultracold molecules: science, technology and applications. *New Journal of Physics*, 11(5):055049, May 2009.

[134] Loïc Anderegg. *Ultracold molecules in optical arrays: from laser cooling to molecular collisions*. PhD thesis, Harvard University, September 2019.

[135] Nicholas R. Hutzler, Hsin-I Lu, and John M. Doyle. The Buffer Gas Beam: An Intense, Cold, and Slow Source for Atoms and Molecules. *Chemical Reviews*, 112(9):4803–4827, September 2012.